7-2024

A New Diagnostic Method for Distinguishing Binary from Single Supermassive Black Holes Using Broad Emission Lines

Ziming Ji
zj4050@rit.edu

Recommended Citation

Ji, Ziming, "A New Diagnostic Method for Distinguishing Binary from Single Supermassive Black Holes Using Broad Emission Lines" (2024). Thesis. Rochester Institute of Technology. Accessed from

RIT | College of Science
Astrophysical Sciences
and Technology

A New Diagnostic Method for Distinguishing Binary from SingleSupermassive Black Holes Using Broad Emission Lines

By

Ziming Ji

A Thesis Submitted in Partial Fulfillment of the
Requirements for the Degree of Master of Science. in
Astrophysical Sciences & Technology

School of Physics and Astronomy
College of Science
Rochester Institute of Technology
Rochester, NY

July 2024

Approved by:____
Andrew Robinson, Ph.D Date
Director, Astrophysical Sciences and Technology

RIT | College of Science
Astrophysical Sciences
and Technology

CERTIFICATE OF APPROVAL

MASTER DEGREE Thesis

The Master's. Degree Thesis of Ziming Ji has been examined and approved by the thesis committee as satisfactory for the dissertation requirement for the Master of Science degree in Astrophysical Sciences and Technology.

Dr. Andrew Robinson, Thesis Advisor

Dr. Manuela Campanelli, Committee Member

Dr. Michael Richmond, Committee Member

Date ______________________________

A New Diagnostic Method for Distinguishing Binary from Single Supermassive Black Holes Using Broad Emission Lines

---

M.S. *Master of Science*

in Astrophysical Sciences and Technology

Ziming Ji

School of Physics and Astronomy

Rochester Institute of Technology

Rochester, New York

July 2024

ASTROPHYSICAL SCIENCES AND TECHNOLOGY
COLLEGE OF SCIENCE
ROCHESTER INSTITUTE OF TECHNOLOGY
ROCHESTER, NEW YORK

CERTIFICATE OF APPROVAL

M.S. DEGREE THESIS

The M.S. Degree Thesis of *Ziming Ji* has been examined and approved by the thesis committee as satisfactory for the thesis requirement for the M.S. degree in Astrophysical Sciences and Technology.

Dr. Andrew Robinson, Thesis Advisor

Dr. Manuela Campanelli, Committee Member

Dr. Michael Richmond, Committee Member

Date

A New Diagnostic Method for Distinguishing Supermassive Binary Black Holes from Single Supermassive Black Holes Using Broad Emission Lines

By

Ziming Ji

A thesis submitted in partial fulfillment of the
requirements for the degree of M.S. in Astrophysical
Sciences and Technology, in the College of Science,
Rochester Institute of Technology.

July, 2024

Approved by

Dr. Andrew Robinson | Date
Director, Astrophysical Sciences and Technology

Abstract

During cosmic timescales, supermassive binary black holes (SMBBHs) form by galaxy mergers, where each galaxy hosts a supermassive black hole (SMBH) at its center. By studying SMBBHs, we can gain insights into galaxy evolution and black hole growth. However, the typical separation between black holes in SMBBHs is usually below 1 pc, making them difficult to resolve using direct imaging or photometry. To be able to distinguish binary black holes (BBHs) from typical AGN powered by single black holes (SBHs), we conducted this research project to develop a new diagnostic method to identify a unique feature of SMBBHs, which can be used to distinguish AGN powered by BBHs from those powered by SBHs.

The basic idea of this method is that BBHs have different configurations compared with those of SBHs, such as the circumbinary disk enveloping the whole binary system, the minidisks around each black hole, and the streams between the circumbinary disk and minidisks. It is these different configurations of accretion disks of black holes that lead to the difference in the spectral energy distributions (SEDs), which in turn will differently photoionize the broad line region (BLR) and produce different strengths of broad emission lines. Thus, it is these differences in strengths of broad emission lines that we expect to see between two different configurations of black holes, either binary or single black holes. By identifying these differences in line strengths, we can distinguish between binary and single black holes.

In order to achieve this goal of distinguishing BBHs from SBHs, we organized our project in the steps below: (1) obtained BBH SEDs from Gutiérrez et al., 2022, (2) generated SBH SEDs using XSPEC modeling code OPTXAGNF, (3) produced single-cloud models, which represent the BLR, input BBH and SBH SEDs into the models, and simulated the single0cloud response with a photoionization code Cloudy, (4) built cloud-ensemble models, which represent a more realistic BLR, input BBH and SBH SEDs into the models, and simulated the emission-line response within those clouds using a broad emission line mapping code BELMAC.

In step (3), we have explored the differences in line ratios between BBH and SBH for a representative single-cloud photoionization model. The emission lines we used here are: Si IV λ1400Å, C III] λ1909Å, C IV λ1549Å, Mg II λ2798Å, and Lyα λ1216Å. It turned

out that differences do exist, but they are too small to be identified in observational data. Furthermore, we have investigated the line equivalent widths predicted by SBH and BBH models respectively. By doing so, we found some apparent differences between BBHs and SBHs in some specific emission lines: Lyα, CIV, and Hα. However, these differences vanish at the highest mass of black holes ($10^9 M_\odot$).

In step (4), we continued the investigation of the equivalent width between SBH and BBH BLR cloud-ensemble models and found that some emission lines show the difference between BBHs and SBHs, such as CIV in the case of BH mass $10^7 M_\odot$, $U \propto r^{-2}$, and $\log n/1\ \mathrm{cm}^{-3} = 10.5, 11.0$. For the highest mass in the case of $U \propto r^{-2}$, the results are similar to the one in single-cloud models: no difference is shown between BBHs and SBHs across all emission lines. Most importantly, in this step, we found that for CIV λ1549 Å in the case of a black hole mass of $10^7 M_\odot$, $s = -2$, and $\log n/1\ \mathrm{cm}^{-3} = 10.5$, only the SBH EW falls inside the range of the observed range in SDSS DR7 Quasar Catalog while the BBH EW falls outside the range and becomes an outlier. This is what we want to find to distinguish BBHs from SBHs in the observational data.

Contents

List of Figures

List of Tables

Chapter 1

Introduction

1.1 Overview

Supermassive binary black holes (SMBBHs) form through galaxy mergers, wherein two black holes, situated at the center of each merging galaxy (Denuk Richstone et al., 1998; Kormendy et al., 2013), gradually approach each other, ultimately becoming gravitationally bound. In order for the binary to become gravitationally bound, the separation between two black holes is typically at $1-10$ pc (A. De Rosa et al., 2019), which is unresolvable for current telescopes and makes it difficult to distinguish between active galactic nuclei (AGN) powered by SMBBHS and those powered by single supermassive black holes (SMBHs). While it is challenging to distinguish AGNs powered by SMBBHs from those powered by single SMBHs, SMBBHs can provide crucial information about the evolution of galaxies and SMBHs. Therefore, in this research, we aim to develop a diagnostic strategy using broad emission lines to distinguish between AGNs powered by different configurations of black holes, either binary or single black holes. This chapter will provide an introduction to the study by first discussing the background of AGNs and the dynamical evolution of SMBBHs, followed by distinctive electromagnetic signatures of SMBBHs, and eventually the overall thesis structure.

1.2 AGN

Since the first spectroscopic detection of an active galaxy, NGC 1068 by Fath (1909), the general class known as active galactic nuclei (AGN) has been studied in many aspects. An AGN represents a compact region situated at the core of a galaxy, emitting a substantial amount of energy across the entire electromagnetic spectrum. This emission can exceed that of the rest of the galaxy by factors of 100 or more, indicating that stars alone cannot account for its source. The prevailing hypothesis suggests that this significant energy may arise from gas accreting onto an accretion disk surrounding a black hole. In terms of electromagnetic spectra, AGNs are characterized by (a) strong X-ray emission, (b) relatively strong radio emission, (c) non-stellar emission spanning the ultraviolet to infrared wavelengths, and (d) broad emission lines observable across ultraviolet, optical, and infrared wavelengths.

The unified AGN model, shown in Figure 1.1, elucidates the internal structure of these systems, which typically consist of a central black hole encircled by an accretion disk. the photoionized gas clouds in or around the disk constitute the broad-line region (BLR) that produces strong, broad emission lines. Extending outward from the BLR is the dusty torus, delineated by the dust-sublimation radius, R_d, the closest distance to the central source where dust can persist. The expression of dust-sublimation radius assessed by Nenkova et al. (2008) is:

$$R_d \backsimeq 0.4 \left(\frac{L}{10^{45} \mathrm{erg/s}} \right)^{1/2} \left(\frac{1500\ \mathrm{K}}{T_{sub}} \right)^{2.6} \ \mathrm{pc}, \tag{1.2.1}$$

where L is the luminosity of the central source and T_{sub} is the sublimation temperature for dust. Surrounding these structures is the narrow-line region (NLR), spanning up to hundreds of parsecs, where narrow forbidden and permitted lines originate. Moreover, radio jets are occasionally observed spanning various scales and aligned with the system's axis. At the heart of the unified AGN model lies the dusty torus surrounding the central source and the BLR. Depending on the torus's inclination angle, emissions from the BLR and central source may be obscured or unobstructed. When the torus obscures these inner structures, a

Seyfert 2 spectrum is observed in the nucleus of the host galaxy; conversely, when they remain unobscured, a Seyfert 1 spectrum is observed.

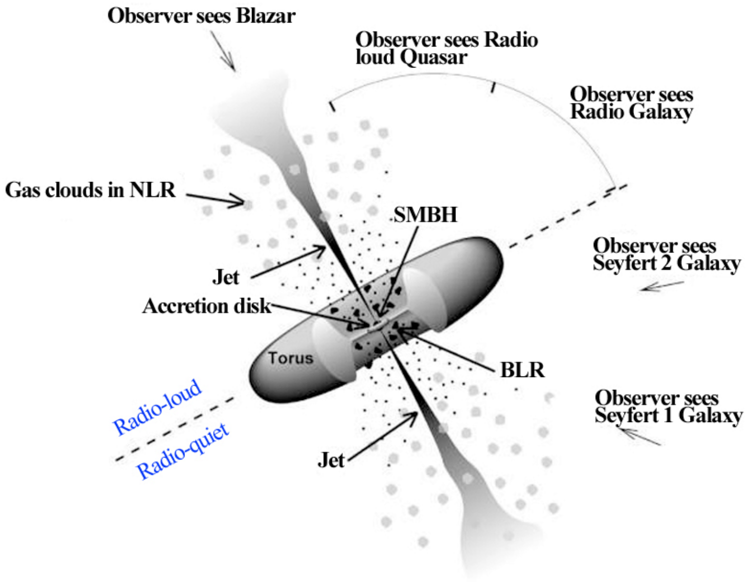

Figure 1.1: The unified AGN model. This figure describes the components of an AGN: an SMBH at the center, an accretion disk around the central SMBH, a dusty torus obscuring part of the BLR, and an NLR. The other labels indicate various categories of AGN that are observed based on the direction of the observer. Figure taken from Urry et al. (1995).

1.2.1 Accretion and SEDs of SMBHs

As depicted in Figure 1.1, the standard AGN model posits an SMBH encircled by an accretion disk. The strong gravitational pull of the black hole draws in the matter, yet owing to the matter's angular momentum, the majority of infalling matter initially forms an accretion disk. Within this disk, matter progressively moves inward due to viscous torques, wherein the material's gravitational potential energy transforms into kinetic energy and is radiated away as heat. This thermal energy heats the disk, causing it to emit thermal photons. Under the assumption that the disk is optically thick, it radiates locally like a blackbody, generating the big blue bump shown in Figure 1.2.

Apart from the thermal emission, non-thermal emission also contributes to the SED, which is produced by the inverse Compton scattering and synchrotron radiation. Firstly, the inverse

Compton scattering occurs when relativistic electrons collide with the photons and increase the photon energy. Secondly, synchrotron radiation occurs when a collection of electrons spirals around magnetic field lines at relativistic speeds. Moreover, there is an infrared bump in Figure 1.2, which is due to emission from warm ($T \leq 2000$ K) dust grains.

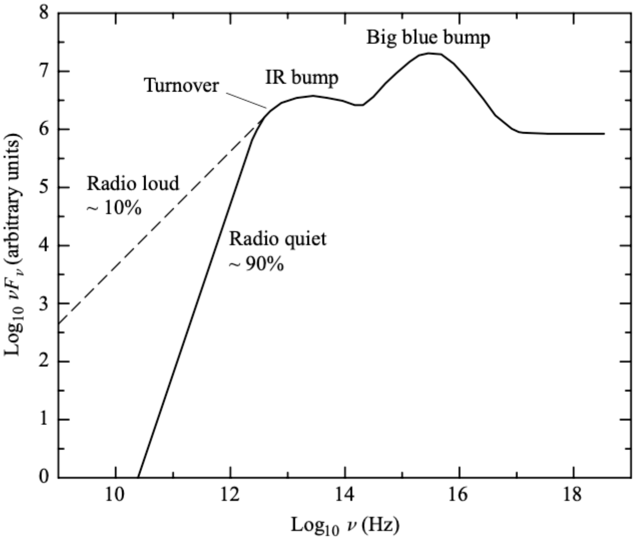

Figure 1.2: A sketch of typical AGN SEDs. Adapted from Carroll et al. (2017).

Under the assumption that the disk surfaces radiate as a blackbody, the thermal structure of an accretion disk can be calculated using the equation 1.2.2:

$$T \approx 2.1 \times 10^5 \left(\frac{M}{10^7 M_\odot}\right)^{-1/4} \eta^{-1/4} \left(\frac{\dot{M}}{\dot{M}_{\mathrm{Edd}}}\right)^{1/4} \left(\frac{r}{r_0}\right)^{-3/4} \ \mathrm{K}, \tag{1.2.2}$$

where M is the black hole mass, η is the efficiency, r_0 is the inner radius of the disk, and $\dot{M}$ is the accretion rate.

Based on the blackbody assumption, the radiation intensity of a single blackbody of temperature $T(r)$ is described by the Planck function:

$$B_\nu = \frac{2h\nu^3}{c^2} \frac{1}{\exp(h\nu/kT(r)) - 1}, \tag{1.2.3}$$

which in turn describes the flux from each concentric ring of the disk as observed from a distance D:

$$F_\nu = \frac{4\pi h \cos i \nu^3}{c^2 D^2} \int_{r_0}^{r_{\rm out}} \frac{r dr}{\exp(h\nu/kT(r)) - 1} \tag{1.2.4}$$

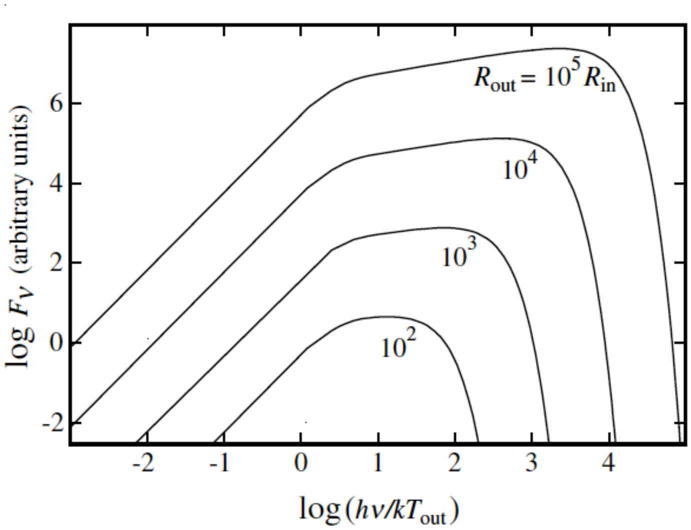

Figure 1.3: A continuum spectrum F_ν of an optically thick disk radiating like a blackbody. Adapted from Frank et al. (2002).

Equation 1.2.4 has three regimes, as shown in Figure 1.3:

- Low-frequency regime $h\nu \ll kT(r_{\rm out})$: the Planck function B_ν takes the Rayleigh-Jeans limit, $F_\nu \propto \nu^2$.
- Intermediate-frequency regime $kT(r_{\rm out}) < h\nu < kT(r_0)$: the spectrum is nearly flat, $F_\nu \propto \nu^{1/3}$.

- High-frequency regime $h\nu \gg kT(r_0)$: the Planck function $B_n u$ takes the Wien form, $F_\nu \propto \nu^3 e^{-h\nu/kT}$.

Moreover, the temperature relates to the wavelength by Wien's law (Equation 1.2.5) and wavelength is further related to the energy by Equation 1.2.6.

$$\lambda_{\text{peak}} = \frac{2.821 \times 10^{-3}\ \text{m} \cdot \text{K}}{T_{\text{peak}}[\text{K}]} \tag{1.2.5}$$

$$E = h\nu = \frac{hc}{\lambda} \tag{1.2.6}$$

1.3 Dynamical Evolution of SMBBHs

In the context of the hierarchical evolution of galaxies, where small galaxies form first and then merge to form larger ones (White et al., 1978; White et al., 1991), and with the assumption that each massive galaxy contains an SMBH at its center (Denuk Richstone et al., 1998; Kormendy et al., 2013), SMBBHs will form through these galactic mergers (Haehnelt et al., 2002).

Correlations between the mass of a central SMBH and its host galaxy have been established by many studies (Kormendy et al., 1995; Magorrian et al., 1998; Tremaine et al., 2002; McConnell et al., 2013). Among these correlations, the tightest one is between the black hole mass, M_{BH}, and the stellar velocity dispersion of the bulge, σ:

$$\log\left(\frac{M}{M_\odot}\right) = \alpha + \beta \log\left(\frac{\sigma}{200\ \text{km s}^{-1}}\right), \tag{1.3.7}$$

where $\alpha = 8.32 \pm 0.05$ and $\beta = 5.64 \pm 0.32$ (Bogdanovi et al., 2022; McConnell et al., 2013).

This correlation suggests that massive galaxies harbor black holes with masses $M_{\text{BH}} \sim 10^6 - 10^8 M_\odot$, corresponding to the mass range of SMBHs.

For these SMBHs to merge, there are several important phases from galactic merger to black hole merger (Begelman et al., 1980):

- Phase I: Dynamical Friction Phase, where two black holes are dragged by the dynamical friction in the stellar bulge of the post-merger galaxy, ends with the formation of a close Keplerian binary.
- Phase II: Binary Hardening Phase, where the binary orbit decays due to energy loss due to stellar encounters, and
- Phase III: GW Dominated Phase, where the binary orbit decays due to GW emissions, ends with the coalescence of the two black holes.

1.3.1 Phase I: Dynamical Friction

When a massive object, such as an SMBH with a mass M_{BH}, traverses through the stellar background, the gravitational pull is exerted on this massive object by the stellar background. This gravitational pull acting as a brake is named "dynamical friction".

In this phase, as described in Bogdanovi et al. (2022), dynamical friction serves as a crucial pathway for the formation of gravitationally bound black hole binaries. Initially, during the merger of two galaxies, their SMBHs remain closely attached to their stellar bulges. As the parent bulges gradually converge, approaching a distance ~ 1 kpc, they eventually merge, leading to a gradual dissipation until the SMBHs become detached. Provided that the mass of the stars and gas in the background significantly exceeds the total mass of the two black holes, both SMBHs experience a pull toward each other induced by dynamical friction exerted by the stellar and gaseous background within the post-merger galaxy.

Under the influence of dynamical friction, the separation between two black holes shrinks with a timescale described by Colpi (2014):

$$\tau_{df} \approx \frac{2 \times 10^8}{\ln N} \left(\frac{10^6 M_{\odot}}{M_{\mathrm{BH}}} \right) \left(\frac{r}{100\ \mathrm{pc}} \right)^2 \left(\frac{\sigma_*}{100\ \mathrm{km/s}} \right) \tag{1.3.8}$$

This equation describes the timescale for phase I with several parameters: a stellar background of N stars in a singular isothermal sphere, a one-dimensional velocity dispersion σ_* that describes a stellar density $\rho_* = \sigma_*^2/(2\pi G r^2)$, a black hole mass $M_{\rm BH}$, and a sinking-start distance r.

As depicted by this equation, for a given black hole mass and specific velocity dispersion, the smaller r is, the shorter the timescale, indicating that dynamical friction increases with orbital decay. Ultimately, the black holes form a gravitationally bound system, marking the start of Phase II, the binary hardening phase.

1.3.2 Phase II: Binary Hardening

As dynamical friction gradually draws two black holes together, a binary system forms when the total mass of stars enclosed within the binary orbit is less than twice the mass of the binary system. A typical separation for the formation of the binary system is $a \approx 10$ pc (Mayer et al., 2007; Dotti et al., 2007; Khan et al., 2012).

Throughout this process, the dynamical friction weakens as the black holes gain higher velocities during inspiral. Once the separation between to black holes drops below $a_{\rm hard}$, phase I concludes, yielding the stage to phase II, the binary hardening phase.

$$a_{\rm hard} = \frac{G\mu}{3\sigma_*^2} = 0.1\frac{q}{(q+1)^2}\left(\frac{M_{\rm tot}}{10^6 M_\odot}\right)\left(\frac{\sigma_*}{100\ {\rm km/s}}\right)^{-2}\ {\rm pc}, \qquad (1.3.9)$$

where $M_{\rm tot}$ is the mass of the binary system, q is the mass ratio between two black holes, and $\mu = M_{\rm tot} q/(q+1)^2$ is the reduced mass of the binary (Quinlan, 1996; Yu, 2003; Merritt et al., 2004b; Colpi, 2014).

During this hardening phase, dynamical friction ceases to effectively draw two black holes together. In order to continue orbital decay, the binary system needs to interact with individual stars to lose orbital energy and angular momentum. This interaction is known as "stellar scattering". Under the influence of stellar scattering, the hardening timescale to coalescence is

$$\tau_{\mathrm{hard}} = \frac{\sigma_*}{\pi G \rho_* a} = 70 \left(\frac{\sigma_*}{100\ \mathrm{km/s}}\right) \left(\frac{10^4 M_\odot\ \mathrm{pc}^{-3}}{\rho_*}\right) \left(\frac{10^{-3}\ \mathrm{pc}}{a}\right), \tag{1.3.10}$$

where σ_* is the velocity dispersion of stars, ρ_* is the density of the stellar background, and a is the semi-major axis of the binary system (Colpi, 2014). In contrast to the timescale driven by dynamical friction, the hardening time increases when two black holes become closer to each other, indicating that it is more difficult to harden the binary as two black holes approach the merger.

However, a significant challenge arises with stellar scattering. As the binary system interacts with individual stars and approaches merger, these stars are expelled from the galactic center, leading to a decrease in the number of stars available to interact with the binary system. Consequently, there may eventually not be a sufficient number of stars for stellar scattering, potentially causing the binary to stall at a certain separation, typically around 1 pc. This challenge is commonly referred to as the "final parsec problem".

To address this challenge, several solutions have been proposed: in galaxies with a non-spherical potential, the stellar reservoir can be replenished (Yu et al., 2005); a third SMBH can enter the binary system, reigniting the merger process (Hoffman et al., 2007; Bonetti et al., 2018; Ryu et al., 2018); or gas can facilitate binary orbital decay by dissipating the binary angular momentum through radiation (Bogdanovi et al., 2022).

While a binary system may stall at parsec scales, accumulating evidence suggests that this scenario is only likely in perfectly spherical, idealized galaxies (Amaro-Seoane et al., 2023), where stars are bound to conserve angular momentum. In reality, stellar bulges are often triaxial, allowing stellar orbits to be torqued by the asymmetric mass distribution, and their angular momentum does not necessarily remain conserved over time (Yu, 2002; Merritt et al., 2004a; Merritt et al., 2010). This indicates that the loss cone can be refilled within a Hubble time.

1.3.3 Phase III: GW Dominated

As two black holes come close enough, gravitational waves (GWs) start to drive the merger. During this GW-dominated phase, the timescale driven by GWs is

$$\tau_{\rm gw} = \frac{5.4 \times 10^8}{f(e)} \frac{(q+1)^2}{q} \frac{a^4}{M_{\rm tot}^3} \left(\frac{1}{0.001 \text{ pc}}\right)^4 \left(\frac{10^6 M_\odot}{M_{\rm tot}}\right)^3 \text{ yr} \tag{1.3.11}$$

, where $f(e) = \left[1 + \frac{73}{24}e^2 + \frac{37}{96}e^4\right](1-e^2)^{-7/2}$ and e is the eccentricity of the orbit (Colpi, 2014). The dependence of the GW-driven timescale on the eccentricity of the orbit stems from the fact that GW emission is highly dependent upon the orbital frequency, thus closely linked to the orbital speed.

This phase is divided into three sub-phases: (1) inspiral, during which the orbital velocity of two black holes still exceeds their radial velocity towards each other, (2) merger, marking the fusion of the two black holes into a single one with different mass and spin, and (3) ringdown, when the newly formed black hole stabilizes and emits GWs like a bell.

In a binary with each black hole mass m_1 and m_2, a total mass of $M = m_1 + m_2$, and a reduced mass ratio $\mu = m_1 m_2/M$, the inspiral phase involves the binary orbiting from infinity to the innermost stable circular orbit (ISCO). In geometrized units ($G = c = 1$), the released energy for the inspiral phase is approximately μ times the specific binding energy at the ISCO, yielding $E_{\rm inspiral} \sim \mu$. In contrast, the total energy released during the merger and ringdown phases is estimated as $E_{\rm merger} \sim \mu^2/M$, or equivalently $E_{\rm merger} \sim (\mu/M)E_{\rm inspiral}$ (Bogdanovi et al., 2022).

Therefore, if the black hole mass ratio is $0.1 < q < 1$, the energy emitted during the merger and ringdown could constitute a few percent of the rest mass energy of the binary, comparable to the energy emitted during the inspiral. Conversely, for systems with extreme mass ratios, the GW in the inspiral sub-phase is the most likely to be detected.

In summary, these three processes have timescales listed below:

- Galaxies merge in a few Gyr.

- Two SMBHs become gravitationally bound in $\sim 10^{7-9}$ yr due to dynamical friction.
- SMBBH hardens in $\sim 10^{6-9}$ yr.
- SMBBH coalesces in $\sim 10^{6}$ yr due to the emission of GWs.

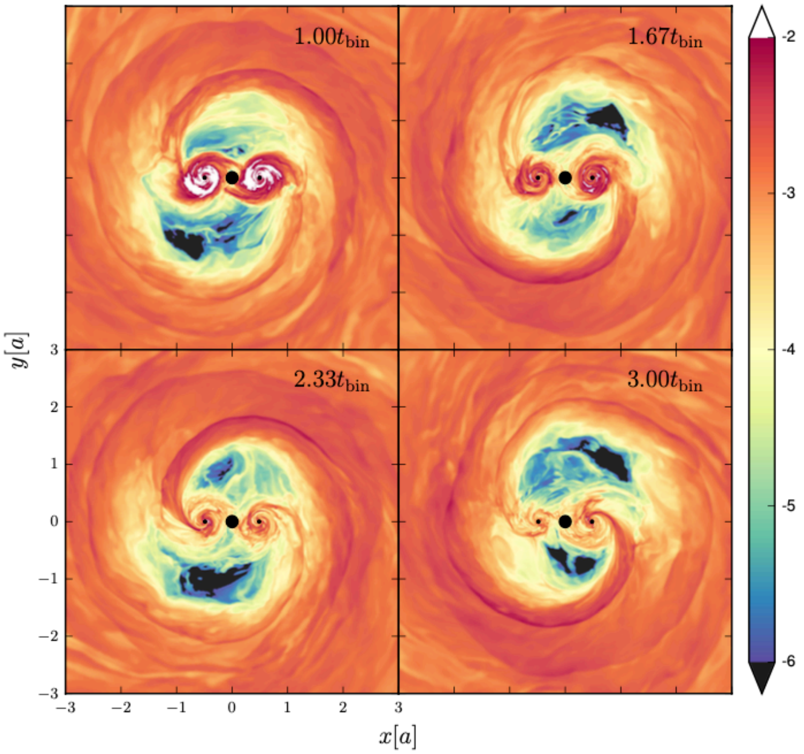

Figure 1.4: Density distribution on a logarithmic scale for a binary black hole system at four distinct time points. Each black hole is depicted by a black circle, with the larger black circle at the coordinate origin denoting the central cutout of the simulation. From one to the next snapshot, the black hole receiving the most material changes. It is BH2 (on the left) in the first frame, BH1 (on the right) in the next, back to BH2 in the third, and BH1 in the fourth. $t_{\rm bin} = 2\pi/\Omega_{\rm bin}$, where $\Omega_{\rm bin}$ is the binary orbital frequency. Adapted from Bowen et al. (2018) with permission from the authors.

1.4 Electromagnetic Signatures of SMBBHs

The galactic environments where SMBBHs form will contain sufficient amounts of gas for them to become electromagnetically bright (Cuadra et al., 2009; Chapon et al., 2013; Colpi, 2014).

Thus, SMBBHs are excellent targets for multimessenger astrophysics following the launch of LISA (J. Baker et al., 2019; Kara et al., 2019). Compared to standard AGNs powered by single black holes, different electromagnetic signatures will be emitted by SMBBHs due to their distinctive features, as shown in Figure 1.4, such as (a) a circumbinary disk surrounding the two black holes, (b) minidisks formed around each black hole, and (c) streams of gas accreted onto the minidisks from the inner edge of the circumbinary disk (Noble et al., 2012; Zilhão et al., 2015; Armengol et al., 2021; S. C. Noble et al., 2021; S. C. Noble et al., 2021; Bowen et al., 2018; Bowen et al., 2019; Gutiérrez et al., 2022).

1.4.1 Circumbinary Disks

Early concerns arose regarding the low inflow rate of material toward merging black holes via a circumbinary disk. These concerns stemmed from two main arguments. Firstly, even when gravitational radiation losses are insufficient to drive orbital evolution, the binary's strong torques on nearby gas can result in the clearance of a substantial cavity within approximately $2a$ of the binary, particularly when the binary mass ratio is close to unity (Artymowicz et al., 1994; Artymowicz et al., 1996; D'Orazio et al., 2016; Bowen et al., 2017; Tang et al., 2018). Therefore, these torques were thought to be able to prevent any mass accretion inside the binary (Pringle, 1991). Secondly, as previously stated, the circumbinary disk may decouple from binary black holes when the GW merger timescale becomes shorter than the accretion timescale of the disk.

Both arguments have been addressed by numerical simulations of SMBBHs. The first argument was resolved by two sets of simulations focused on circumbinary disks. One set, incorporating internal stresses within the disk, demonstrated that gas streams readily detach from the disk's inner edges (MacFadyen et al., 2008; Noble et al., 2012; Shi et al., 2012; D'Orazio et al., 2013). The other set, accounting for defined accretion rates, indicated that all mass traversing through the circumbinary disk is effectively delivered to the binary (Farris et al., 2014; Shi et al., 2015). Moreover, Shi et al. (2015) revealed that binary torques acting on streams within the gap can redirect gas back to the circumbinary disk, where a portion of the stream mass undergoes sufficient angular momentum loss via shock deflection to subsequently accrete onto the binary. This redirection of gas creates an overdensity at the inner edge of the circumbinary disk, which is often referred to as a "lump", which does not appear in disks around a single SMBH.

The second argument was addressed by Noble et al. (2012) and Farris et al. (2015), who demonstrated that as the binary black hole system undergoes orbital decay, the rate of accretion can remain stable. This is attributed to the availability of gas close to the black holes, resulting in a shorter timescale for accretion compared to what was previously estimated based on material from distant regions of the disk (Bowen et al., 2017). This remains true even in the case of spinning black holes (Armengol et al., 2021). Additionally, Noble et al. (2012) showed that the circumbinary disk can remain bound to the binary system up to a separation of $a \sim 10M$. Consequently, at this separation, the efficiency of energy released amounts to 5% of the rest mass energy, resulting in a luminous circumbinary disk:

$$\eta = \frac{M}{r_{\mathrm{in}}} = \frac{M}{2a} \sim 5\% \tag{1.4.12}$$

where r_{in} is the size of the inner edge of the circumbinary disk.

1.4.2 Minidisks and Streams

As mentioned in the previous subsection, contrary to earlier assumptions that gas cannot accrete within the circumbinary disk, it is indeed capable of inward movement, forming minidisks around each member of the binary. These minidisks constitute significant deviations from the structure of a typical AGN disk. Consequently, numerous studies have endeavored to elucidate their configuration and the processes governing their ability to generate distinctive electromagnetic signatures (Ju et al., 2016; Ryan et al., 2017; D'Orazio et al., 2015; Bowen et al., 2017; Bowen et al., 2018; Bowen et al., 2019; dAscoli et al., 2018; Tang et al., 2018).

Bowen et al. (2018) found, as depicted in Figure 1.4, that the minidisks, besides having approximately four times the mean surface density of the circumbinary disk, also exhibit an intriguing feature: an accretion switch. The accretion of streams alternates between black holes across four snapshots at a time interval of $(2/3)t_{\rm bin}$, where $t_{\rm bin} = 2\pi/\Omega_{\rm bin}$ with $\Omega_{\rm bin}$ the binary orbital frequency. This alternation is due to the stationarity of the $m = 2$ accretion stream pattern in the corotating frame. Relative to this stationary pattern, the lump moves backward, so that it switches the accretion feeding between two black holes in the binary system (Bowen et al., 2018). Furthermore, the mass difference between two minidisks increases over time.

Bowen et al. (2019) further found that the masses of minidisks have a modulation frequency of $\Omega_{\rm beat}$. At frequencies ranging from $0.2\Omega_{\rm bin}$ to $0.4\Omega_{\rm bin}$ and $2\Omega_{\rm beat}$, the total minidisk mass and the lump angular velocity $\Omega_{\rm lump}$ undergo modulations. As a result, they concluded that the internal time-varying structure of the central cavity, streams, lump, and minidisks are interconnected, producing significant quasi-periodic signatures in the electromagnetic emission of SMBBHs.

1.4.3 BLR

With these distinctive electromagnetic signatures associated with SMBBHs, we expect that the surrounding gas clouds within the BLR will be photoionized differently and produce different strengths of broad emission lines from those photoionized by the AGN powered by single SMBHs. Specifically, the BLR gas clouds are photoionized by the accretion-disk continuum emitted by either binary or single black holes at the center of AGN.

Typically, clouds within the BLR exhibit a high gas density ($n_{\rm gas} \sim 10^{11}$ cm^{-3}) and a high column density ($N_{\rm col} \sim 10^{23}$ cm^{-3}), situated at a distance of approximately $r \sim 1$ pc from the central continuum source (Netzer, 2008). Due to the high gas density, certain forbidden lines may be suppressed. Generally, emission lines require the spontaneous decay of excited atoms from higher to lower energy levels. However, within high-density clouds, much of the level decay arises from collisional de-excitation by electrons, which does not result in photon emission. Consequently, part of the forbidden lines are suppressed in high-density clouds.

Generally, a cloud that is photoionized by a central luminous source will have an illuminated side and a non-illuminated side, which corresponds to the ionized and neutral/partially ionized zones. If the cloud is optically thin, then most of the cloud will be ionized. If the cloud is optically thick, then the illuminated side of the cloud will mostly be ionized while the non-illuminated side will be neutral or partially ionized.

Each cloud in the BLR will be highly ionized in the illuminated side, and if it has a sufficiently high column density, it will be mostly neutral in the non-illuminated side. The illuminated side emits high-ionization lines such as He II, He I, O VI, N V, and C IV, whereas the non-illuminated side emits low-ionization lines such as Mg II, Ca II, O I, and Fe II (Gaskell, 2009).

To determine the ionization level of a cloud within the BLR, the ionization parameter is defined as

$$U = \frac{Q}{4\pi r^2 c n_{\mathrm{gas}}}, \tag{1.4.13}$$

where the ionizing photon emission rate $Q = \displaystyle\int_{\nu_0}^{\infty} \frac{L_\nu}{h\nu} d\nu$ is integrated frequency from the hydrogen ionization frequency ($\nu_0 = 3.29 \times 10^{15}$ Hz). Since Q depends on the continuum shape, changes in the continuum shape will induce variations in Q, causing variations in the ionization parameter.

1.4.4 Research Objective and Significance

Given their dual emission of GWs and electromagnetic signals, SMBBHs represent exceptional targets for multimessenger observations. By combining GW and electromagnetic data, we can refine our understanding of the dynamical interactions between SMBBHs and their environments, elucidate the mechanisms of accretion in their vicinity, and investigate the co-evolution of SMBBHs and their host galaxies (Kelley et al., 2019; Charisi et al., 2022). Moreover, electromagnetic observations can constrain binary parameters, such as the chirp mass and period. For instance, Arzoumanian et al. (2020) utilized electromagnetic data to estimate the upper chirp mass limit of an SMBBH candidate in the center of the galaxy 3C 66B to be $(1.65 \pm 0.02) \times 10^9 M_\odot$ and claimed that this upper limit is improved by a factor of 1.6 over previous limits. Additionally, the identification of binary candidates in electromagnetic data can significantly improve the ability of Pulsar Timing Arrays (PTAs) to detect these binary systems (Liu et al., 2021).

With the capability of detecting nanohertz GWs, PTAs can detect SMBBHs with a mass range $10^8 - 10^{10} M_\odot$ (Kelley et al., 2019), whereas the future Laser Interferometer Space Antenna (LISA) will detect SMBBHs with a mass range $10^5 - 10^7 M_\odot$ (Amaro-Seoane et al., 2017), which emit millihertz GWs.

As previously mentioned, SMBBHs exhibit different characteristics from standard AGNs, such as the circumbinary disk and minidisks. These unique characteristics will yield differences in electromagnetic signatures, particularly their SEDs. These distinct SEDs influence the photoionization of the surrounding gas, resulting in the emission of different strengths of emission lines within the BLR. Detecting differences in the strengths of these emission lines may signify the presence of binary black holes (BBHs) or single black holes (SBHs).

Therefore, the objective of my research project is to develop a diagnostic approach to distinguish BBHs and SBHs using BLR emission lines. If this approach proves feasible, it could enable us to identify the electromagnetic counterparts of future targets of LISA and PTAs.

1.5 Thesis Structure

The structure of this thesis is as follows: we begin chapter 2 by discussing the comparison between the light-crossing time over the BLR and the merger time of BBHs. Next, we introduce the models used to simulate the SEDs of binary and single black holes and outline both the single-cloud (Cloudy) and cloud-ensemble (BELMAC) models. In Chapter 3, we discuss in detail the BBH and SBH SEDs obtained either from General Relativistic Magnetohydrodynamic (GRMHD) simulations or OPTXAGNF modeling, where we used the code OPTXAGNF to model the SBH SEDs. Additionally, we include a more realistic continuum that combines accretion-disk SEDs and galaxy SEDs. In Chapter 4, we present our most important results on the behaviors of broad emission lines within two types of BLR models: single-cloud models and cloud-ensemble models. Finally, in Chapter 5, we present the conclusions and provide an outline for our future work.

In this thesis, we plotted the SEDs using different conventions, such as the wavelengths (Å) and frequency (Hz), to match the conventions of different communities in astronomy. In GRMHD simulations, the convention is to plot the SED with the frequency (Hz). We followed the same conventions in our simulations of single black holes. On the other hand, when calculating the equivalent widths, we follow the observational convention that SEDs are plotted against the wavelength (Å). Note here, the conversion between wavelength (λ) and frequency (ν), $\lambda = \frac{c}{\nu}$. Therefore, an increase in wavelengths indicates a decrease in frequency or energy.

Chapter 2

Description of Models

2.1 Overview

In this chapter, we present the models used in our project. This project is conducted based on the idea that BBH SEDs differ from those of SBHs, which should affect the strengths of broad emission lines in the BLR. Therefore, based on this idea, we aim to determine whether broad emission lines can be used to distinguish BBHs from SBHs. In order to achieve this goal, we took several steps.

Firstly, we obtained BBH SEDs from GRMHD simulations for four BH masses: 10^6, 10^7, 10^8, $10^9 M_\odot$.

Secondly, to compare BBH SEDs with SBH SEDs, we computed the corresponding set of SBH SEDs, which share the same parameters with BBHs (e.g. BH mass, spin, and luminosity).

Thirdly, to simulate the emission-line response from the BLR, we computed photoionization models of a single cloud using a photoionization code called Cloudy (Chatzikos et al., 2023).

Lastly, to generate more realistic line responses, we computed cloud-ensemble models using BELMAC, which is a broad emission line mapping code (Rosborough et al., 2024).

In section 2.2, we present the calculations of timescales for BBHs to assess their detectability and the effect of temporal SED variations on the BLR response. In section 2.3, we delve into the discussion of the models employed in simulating SEDs, including both BBHs and

SBHs. In section 2.4, we introduce the BLR photoionization models utilized in this project, including single-cloud models and cloud-ensemble models.

2.2 Timescales

Model	t_{gw} (days)	R_{BLR} (light days)	t_{orb} (days)
M6	0.73	0.727	0.032
M7	7.3	3.836	0.320
M8	73	27.40	3.202
M9	730	166.13	32.015

Table 2.1: A comparison of key timescales. The "Model" column lists the total black hole mass utilized in the model, where the number denotes the $10^n M_\odot$ of the black hole. t_{gw} represents the merger timescale initiated from a separation $a = 20M$, with M representing the black hole mass. R_{BLR} denotes the radius of the BLR, computed using the luminosity-radius relationship outlined in Bentz et al. (2013). t_{orb} indicates the orbital period, computed using Kepler's Third Law.

Since our project focuses on the emission lines in the BLR, we first calculated the BLR radius (R_{BLR}) using the luminosity-radius relationship in Bentz et al. (2013):

$$\log_{10}\left(\frac{R_{\mathrm{BLR}}}{1 \text{ lt-day}}\right) = 1.527 + 0.533 \log_{10}\left(\frac{\lambda L_\lambda}{10^{44} \text{ erg/s}}\right), \tag{2.2.1}$$

where λL_λ denotes the optical luminosity at wavelength 5100Å. This optical luminosity was obtained by interpolating the SED data for each model (νL_ν vs. λ). This relationship can be approximated as $R_{\mathrm{BLR}} \propto L^{1/2}$.

Secondly, by calculating the merger timescale (t_{gw}) using Equation 2.2.2 in Loeb (2007), we aim to determine whether the merger of black holes can be detected or not.

$$t_{\mathrm{gw}} = 2 \times 10^6 \left(\frac{M}{4\mu}\right)\left(\frac{a}{1000 r_g}\right)^4 \left(\frac{M}{10^7 M_\odot}\right) \text{ yr}, \tag{2.2.2}$$

where M is the binary mass, $\mu = (m_1 m_2)/M$ the reduced mass ratio, $r_g = 2GM/c^2$ the gravitational radius, and a the separation between two black holes. Here, we chose the separation $a = 20M$, since in the GRMHD simulation, the merger starts at this separation.

Additionally, $m_1 = m_2 = M/2$, where m_1 and m_2 represent masses of the two black holes, respectively. Since the separation is fixed, the merger timescale solely depends on M ($t_{\rm gw} \propto M$), as shown in Table 2.1.

Finally, as provided by Gutiérrez et al., 2022, the shapes and specific luminosity of BBH SEDs vary throughout the simulation. Therefore, to assess the significance of temporal SED variations, we approximated the SED variation time to the orbital period of the two black holes. If the SED variation time significantly exceeds the light-crossing time of the BLR, we can detect fluctuations in the SED, which might result in time-dependent variations in the strengths of broad emission lines. Otherwise, these temporal SED variations would be averaged out, appearing as a time-averaged SED. In this case, there will be no significant temporal variations in broad emission lines.

In calculating the orbital period, we applied Kepler's Third Law:

$$T^2 = \frac{4\pi^2}{GM} a^3 \tag{2.2.3}$$

, where $a = 20M$ as well.

When the merger timescale is compared with the light-crossing time, if the merger timescale is significantly shorter than the light-crossing time of the BLR, the BBHs will exist for a relatively brief period compared to the post-merger SBHs. In this case, the strengths of broad emission lines in the BLR will be mainly affected by the post-merger SBHs instead of BBHs.

After calculating of merger and orbital timescales and comparing them to the light-crossing time of the BLR, we found that

- None of the models exhibit merger times significantly smaller than the light-crossing time of the BLR, indicating that in all models the BBHs exist long enough for the BLR to emit broad emission lines that are mainly photoionized by the configuration of BBHs, such as the circumbinary disk, minidisks, and streams, instead of the post-merger SBHs.
- None of the models have orbital times significantly greater than the light-crossing time of the BLR, implying that only time-averaged SEDs can be detected. Consequently, the

strengths of broad emission lines will remain fixed through BH evolution.

2.3 Spectral Energy Distributions

In this section, we describe the SED simulations used in our study. We simulated the SEDs of SBHs to compare with those of BBHs provided by Gutiérrez et al. (2022). Further details regarding the simulations will be provided below.

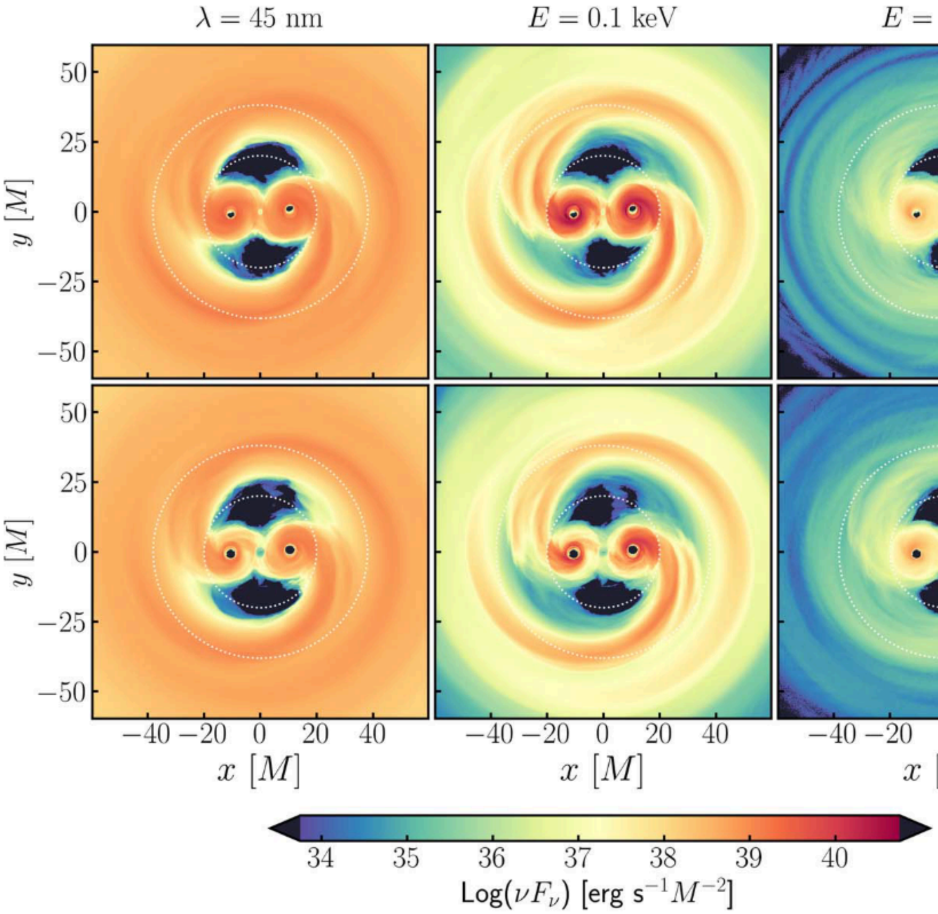

Figure 2.1: Surface brightness map of BBHs in GRMHD simulations, which are averaged in the fifth orbit of the simulation. The inner white circle represents the outer boundary of the minidisks, while the outer one is the inner boundary of the circumbinary disk. The upper panel is from the simulation for spin 0.6 black holes, whereas the lower panel is for spin 0 black holes. Reproduced from Gutiérrez et al. (2022) with permission from the authors.

2.3.1 BBH SEDs

As mentioned above, the BBH SEDs were provided by Gutiérrez et al. (2022). The data of these SEDs was generated in two steps: (1) accretion-disk simulations and (2) electromagnetic emission simulations.

Firstly, the accretion-disk simulations were performed by Combi et al. (2022) using a General Relativistic Magnetohydrodynamic (GRMHD) code HARM3D developed by S. C. Noble et al. (2009). Subsequently, the data from accretion-disk simulations was post-processed by Gutiérrez et al. (2022) using a ray-tracing code BOTHROS, developed by S. C. Noble et al. (2007), to calculate the electromagnetic emissions from these disks.

GRMHD Simulations

In GRMHD simulations, the basic setup is: two black holes with equal mass are placed on a time-dependent spacetime. These black holes are initially placed at a separation $a = 20M$, where units are geometric units ($G = c = 1$). Surrounding this binary system is a circumbinary disk with its inner edge located at a distance $2a$, whose initial properties are obtained from the quasi-steady state snapshot at $t = 50,000M$ from the RunSS simulation described in Noble et al. (2012). Additionally, there are two minidisks encircling each member of the binary system, each minidisk interwoven with a weak poloidal magnetic field (dAscoli et al., 2018).

Specifically, in this GRMHD simulation the evolution of BBHs is based on several constraints: (1) the conservation of baryon number density, (2) conservation of stress-energy, and (3) the Maxwell induction equation (more detailed descriptions in S. C. Noble et al., 2009).

In HARM3D, all dissipated energy is recorded as heat, of which the loss is accounted by a "loss term" $\nabla_\mu T^{\mu\nu} = \mathcal{L}_c u^\nu$, where $T^{\mu\nu}$ is the energy-momentum tensor, and $\mathcal{L}_c$ is the cooling function (Gutiérrez et al., 2022). This cooling function is designed to cool the gas toward the initial entropy ($S_0 = 0.01$) at a rate per unit volume:

$$\mathcal{L}_c = \frac{\rho\epsilon}{t_{\text{cool}}} \left(\frac{\Delta S}{S_0} + \left| \frac{\Delta S}{S_0} \right| \right)^{1/2} \tag{2.3.4}$$

, where ρ is the rest-mass density, ϵ is the specific internal energy, $\Delta S \equiv S - S_0$ with S the specific entropy, and the cooling timescale t_{cool} is defined as:

$$t_{\text{cool}}(r) = \begin{cases} 2\pi(r+M)^{3/2}/\sqrt{M} & \text{if } r \geq 1.5a \\ 2\pi r_{\text{BL,i}}^{3/2}/\sqrt{m_i} & \text{if } r_i \leq 0.45a \\ 2\pi(1.5a+M)^{3/2}/\sqrt{M} & \text{otherwise} \end{cases} \tag{2.3.5}$$

In the equation above, $r_{\text{BL,i}}$ is the Boyer-Lindquist radial coordinate in the co-moving frame of the i-th black hole, and m_i is the i-th black hole mass.

Radiative Transfer Simulations

Once the accretion-disk data is generated, it is post-processed by BOTHROS, a general relativistic ray-tracing code developed by S. C. Noble et al. (2007). BOTHROS adopts an observer-to-source method, wherein a distant simulated camera emits photons toward the source along geodesic paths. Each launched ray contributes a spectrum, I_ν, to individual pixels within the simulated camera. Additionally, Gutiérrez et al. (2022) employed the fast-light approximation, assuming that the simulation data remains constant over the duration of the photon travel time.

2.3.2 SBH SEDs

To compare with BBH SEDs, we simulated the SBH SEDs using the accretion-disk modeling code OPTXAGNF developed by Done et al. (2012). OPTXAGNF assumes a standard blackbody disk model for a mass accretion rate $\dot{M}$ onto a black hole of mass M and spin a^*. It utilizes the effective temperature as a function of radius derived from the Novikov-Thorne relativistic disk emissivity. The fluxes from each annulus in the disk are integrated over all radii from the edge of the disk r_{out} to the innermost stable circular orbit (ISCO) radius with isotropic emission assumed (Done et al., 2012).

OPTXAGNF models three components in a typical AGN SED: (1) thermal emission of the accretion disk, where the photon energy typically peaks in the UV band, (2) a non-thermal power-law component ($E > 2$ keV), produced by the Compton upscattering of seed photons by the electrons surrounding the disk, and (3) a soft X-ray excess ($E < 1$ keV) with an unknown origin. In AGN the X-ray emission is attributed to Compton upscattering of the UV photons emitted by the disk. Therefore, the "corona radius" (r_{cor}) is used to define the boundary of a region where Compton upscattering predominantly occurs (Jin et al., 2012).

The parameters we used to generate SBH SEDS are listed in Table 2.2. For the SBH models the mass, spin, and luminosity were chosen to match those of the corresponding BBH model: using the total BBH mass, the spin of the individual black hole and the time-averaged SED luminosity.

Model	$\log(L/L_{\mathrm{Edd}})$	a^*	r_{cor} (r_g)	$\log(r_{\mathrm{out}}/r_g)$	kT_e (keV)	τ	Γ	f_{pl}	z
M6	-0.8834	0.6	10	5	0.2	10	1.55	0.56	0
M7	-1.0634	0.6	10	5	0.2	10	1.55	0.56	0
M8	-1.0634	0.6	10	5	0.2	10	1.55	0.56	0
M9	-1.0634	0.6	10	5	0.2	10	1.55	0.56	0

Table 2.2: SBH parameter table for OPTXAGNF. L/L_{Edd} is the Eddington ratio for time-averaged luminosity. a^* is the spin parameter. r_{cor} is the coronal radius (outer boundary where inverse Compton scattering occurs), in units of the gravitational radius r_g. r_{out} is the outer radius of the disk, in units of r_g. kT_e is the energy of the Compton optically thick material that produces the soft X-ray excess. τ is the optical thickness of the Compton optically thick material. f_{pl} is the proportion of the corona power emitted in the hard power-law component. Γ is the negative photon power-law index of the hard X-ray tail component.

These emission processes, such as blackbody radiation and inverse Compton scattering, are also included in the GRMHD simulations. As mentioned above, the codes we used are different for binary and single black holes. Specifically, BBH simulations consider the relativistic effect of curved spacetime and calculate the emissions along geodesics while OPTXAGNF does not. But they both were built upon the same theories of radiative processes, such as the thermal blackbody radiation and inverse Compton scattering. Therefore, the differences in the SED shape they show are what we would expect to see in real binary and single black holes.

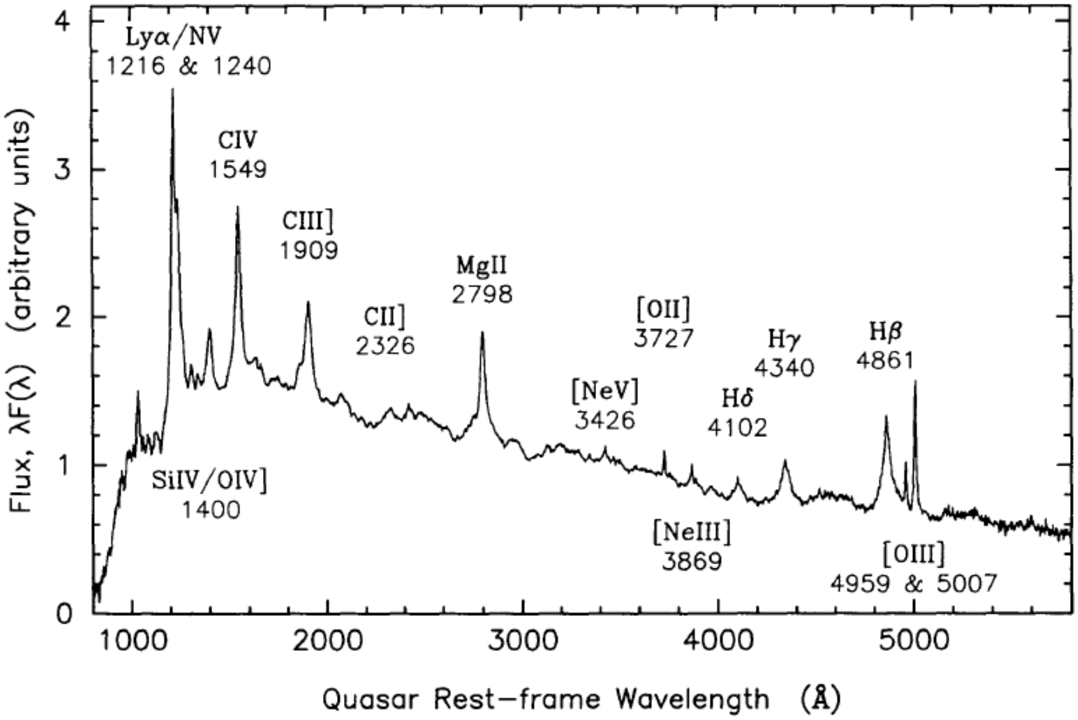

Figure 2.2: A typical quasar spectrum. Adapted from Francis et al. (1991).

2.4 Photoionization Models

Once we acquired the SEDs of both SBHs and BBHs, we proceeded to construct photoionization models to simulate the BLR response in terms of its emission lines. These models calculate the ionization and thermal structures within individual clouds, allowing us to compute theoretical line emissions. We employed two types of photoionization models: (1) single-cloud models, which compute line emission of a single cloud, and (2) cloud-ensemble models, where the line emission is aggregated over multiple clouds. The latter models offer a more realistic representation of the BLR.

Since in this project we only considered the BLR, the emission lines used to probe the difference in SEDs are strong broad emission lines, as shown in Figure 2.2: Si IV λ1400Å, C III] λ1909Å, C IV λ1549Å, Mg II λ2798Å, and Lyα λ1216Å.

2.4.1 Single-Cloud Models

As a preliminary step, we approximated the BLR as a single cloud, as assumed by the photoionization code Cloudy. Developed by Ferland et al. (1998), Cloudy calculates the ionization distribution, level populations of excited states, and electron temperature within a cloud that is illuminated by the radiation field of a source of continuum radiation. Based on these conditions, it generates a theoretical spectrum containing emission and absorption lines. To simulate the line emissions within a cloud, we first defined a grid of parameters that characterize the cloud: (1) gas density (purely hydrogen) $n_H = 10^{11}$ cm^{-3}, which is typical in a BLR, (2) the cloud overall column density $\log N_{\rm col} = 22, 23, 24, 25$ cm^{-2} for which the cloud ranging from being optically thin to optically thick, and (3) the cloud composition with the default solar composition in Cloudy.

It is also necessary to specify the incident spectrum. Based on the timescale calculations in section 2.2, only time-averaged SEDs matter to the strengths of broad emission lines. Therefore, we computed the time-averaged SEDs, from the data provided by Gutiérrez et al. (2022), by averaging each luminosity at each corresponding frequency over the evolution time in the GRMHD simulation.

Additionally, a mode needs to be specified in Cloudy, whether it is a luminosity case, where the line strengths are calculated in terms of the luminosity of a surrounding sphere, or an intensity case, where the line strengths are calculated in terms of flux. We tried both cases and chose to use the intensity case because we only need the line flux in a single cloud, not the total line luminosity of the sphere. In order to use the intensity case, we need to specify an ionization parameter, which characterizes the ionization level within a cloud. This parameter is described by the equation:

$$U = \frac{Q}{4\pi r^2 c n_{\rm H}} \tag{2.4.6}$$

, where $Q = \displaystyle\int_{\nu_{\rm min}}^{\nu_{\rm max}} \frac{L_\nu}{h\nu}$ is the ionization photon luminosity with a specific luminosity L_ν and

h is the Planck constant, r is the distance between the central luminous source and the cloud, and n_{H} is the hydrogen density within a cloud.

We computed the BLR radius based on the equation 2.2.1. Subsequently, we positioned this single cloud at three different locations: 1R, 2R, and 4R, which is equivalent to varying the ionization parameter with respect to the BLR radius based on the equation 2.4.6. Additionally, as shown in the list of cloud parameters, we varied the column density to assess its impact on the ionization structure within the cloud.

2.4.2 Cloud-Ensemble Models

While Cloudy offers preliminary insights into BLR emission lines, as mentioned earlier, its assumption of a single cloud for the BLR is unrealistic. To address the complexity of millions of clouds in the BLR, we turned to BELMAC, a broad emission line mapping code developed by Rosborough et al. (2024), which models a 3D ensemble of gas clouds for the BLR.

As outlined in Rosborough et al. (2024), BELMAC characterizes the BLR as a collection of clouds, where the outer boundary of the BLR is determined by the dust sublimation radius R_d (Equation 1.2.1) and the inner boundary of the BLR, R_{in}, is determined by the scaling parameter $Y_{\mathrm{BLR}} = R_d/R_{\mathrm{in}}$.

Additionally, for each cloud in the cloud ensemble, BELMAC follows the assumptions of photoionization models made by Netzer (2008) and defines a power-law index s for gas density $n_{\mathrm{gas}}(r) \propto r^s$. From mass conservation, $R_{\mathrm{cl}}^3(r) n_{\mathrm{gas}}(r) = \mathrm{Const}$, the size of a spherical cloud can be derived as $R_{\mathrm{cl}}(r) \propto r^{-s/3}$. Consequently, based on the cloud's size, the overall column density of a cloud is given by $N_{\mathrm{col}}(r) = n_{\mathrm{gas}}(r) R_{\mathrm{cl}}(r) \propto r^{2s/3}$. Furthermore, the number of clouds within an element of the radius is described by a power-law index p, where $N_{\mathrm{tot}}(r) \propto r^p$.

Although BELMAC incorporates the reverberation mapping effect, we omit its consideration in this study because $t_{\mathrm{orb}} \ll t_{\mathrm{lc}}$ as discussed in section 2.2. Therefore, we only used part of the functionality of BELMAC to generate the total line luminosity without the reverberation mapping effect.

While BELMAC requires the specification of numerous parameters, we focus solely on defining the input SED and the power-law density of the gas, denoted by $s = 0$ or $s = -2$. The SEDs employed are the BBH and SBH SEDs mentioned earlier, and the selection of the s is made to ensure that the ionization parameter U is proportional to r^{-2} or remains constant. All the parameters we used in this project are listed in Table 4.2.

Chapter 3

Spectral Energy Distributions for Binary and Single Black Holes

3.1 Overview

As previously discussed in Chapter 2, we have obtained two types of SEDs: BBH SEDs from GRMHD simulations and SBH SEDs from OPTXAGNF simulations. As shown by the timescale calculations discussed in section 2.2, only time-averaged SEDs matter at the BLR because the variations in the SEDs are smoothed out over the light travel times. Therefore, we averaged the BBH SEDs over time and simulated SBH SEDs using the time-averaged luminosity of BBHs to compare with the binary SEDs.

3.2 GRMHD BBH SEDs

To start with, we are provided with BBH SEDs by Gutiérrez et al. (2022). They provided us with BBH SEDs for four total masses of the binary system: 10^6, 10^7, 10^8, $10^9 M_\odot$.

As discussed in Gutiérrez et al. (2022), there are three main emission contributors to the BBH SEDs: (a) the circumbinary disk, (b) the streams, and (c) the minidisks around each member of the binary. Despite the cavity contributing negligible emission, it is still included in the total emission. These components' spatial distributions, as depicted in Figure 2.1, are

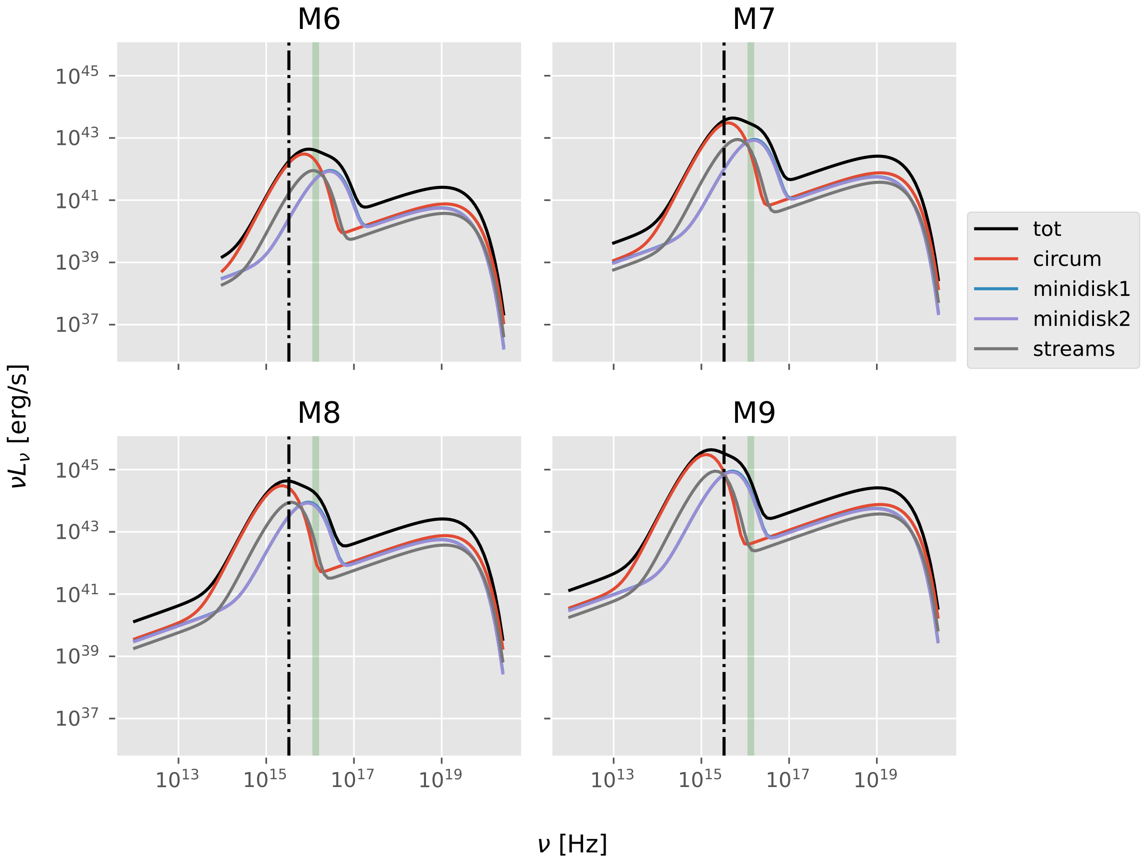

Figure 3.1: Time averaged SEDs for BBHs ranging from M6 ($10^6 M_\odot$) to M9 ($10^9 M_\odot$), featuring total emission (black), circumbinary-disk emission (red), emission from minidisk1 (blue) and minidisk2 (violet), along with stream emission (gray). The shaded green area represents the CIV ionization range: $44.89 - 64.49$ eV. The dot-dashed line represents the hydrogen ionization frequency, which is about 3.29×10^{15} Hz. Plot reproduced with the data provided by Gutiérrez et al. (2022).

defined as (a) $r > r_{12}$ for the circumbinary disk, (b) $r_{12} < r < 2r_{12}$ for the streams, and (c) $r_i < 0.45r_{12}$ for each minidisk, where r_{12} is the separation between two black holes in the binary system, and r_i is the distance from each black hole. In each case, the emission is computed under the assumption that the thermal component arises from a multi-temperature blackbody, whereas the non-thermal component originates from Compton upscattering.

For the case of M6 ($M_{\rm BH} = 10^6 M_\odot$), the thermal peak of the circumbinary disk occurs in the extreme UV band, with an effective temperature of $T_{\rm eff} \sim 9 \times 10^4$ K, dominating the bolometric luminosity. Conversely, the minidisks positioned closer to the black hole exhibit higher temperatures, approximately $T_{\mathrm{eff}} \sim 3.2 \times 10^5$ K, peaking in the far-UV band. The dominance of emission from the circumbinary disk over the minidisks can be attributed to two factors. Firstly, the accretion rate of the minidisks is lower compared to that of the circumbinary disk. Secondly, the reduced angular momentum of gas within the minidisks results in a smaller loss of angular momentum, leading to lower energy dissipation compared to the circumbinary disk (Gutiérrez et al., 2022).

As shown in Figure 3.1, a notable trend emerges among these BBH SEDs: as the black hole mass increases, the SEDs shift towards the lower-frequency range. This phenomenon is attributed to the more massive black holes having a larger ISCO radius, resulting in accretion disks positioned farther away with lower temperatures compared to those of lighter black holes. The ISCO radius, as given by Reynolds (2021), is related to the spin parameter a of a black hole according to the equations:

$$R_{\mathrm{ISCO}} = \left(3 + Z_2 \mp [(3 - Z_1)(3 + Z_1 + 2Z_2)]^{1/2}\right) R_g \tag{3.2.1}$$

, where the ∓ sign indicates prograde/retrograde spinning directions for black holes, and

$$Z_1 = 1 + (1 - a^2)^{1/3} \left[(1 + a)^{1/3} + (1 - a)^{1/3}\right] \tag{3.2.2}$$

$$Z_2 = (3a^2 + Z_1^2)^{1/2} \tag{3.2.3}$$

$$R_g = \frac{GM}{c^2} \tag{3.2.4}$$

For instance, in our project, the black holes have the spin parameter $a = 0.6$; thus, the corresponding ISCO radius is $R_{\mathrm{isco}} = 3.8 R_g$. More massive black holes have a larger ISCO radius, which is also the inner radius of an accretion disk.

Under the assumption that the disk radiates as a black body and is optically thick and geometrically thin, the temperature across the disk follows

$$T_{\text{eff}}(R) \propto R^{-3/4} \tag{3.2.5}$$

, where R represents the distance from the center. Consequently, the disk is cooler at larger radii if it is in a steady state. This behavior explains why, as shown in Figure 3.1, more massive black holes display thermal bumps at lower frequencies, related to the temperature with $h\nu = kT$. These thermal bumps follow a relationship with the black hole mass (Gutiérrez et al., 2022):

$$\nu_{\text{peak}} \propto M^{-0.25} \tag{3.2.6}$$

Moreover, the luminosity scales with the black hole mass as $L \propto M$, indicating that with more mass, the black hole is more luminous at a given Eddington ratio. Interestingly, both streams and minidisks exhibit peaks at nearly the same luminosities, consistent with the brightness map where streams and minidisks are represented in similar colors, as in Figure 2.1. For the non-thermal emissions, the minidisks exhibit stronger emissions than those of the circumbinary disk because the Compton up-scattering is much more important in the inner regions of BBHs.

3.3 OPTXAGNF SBH SEDs

To compare BBHs with SBHs, we used OPTXAGNF to simulate SBH SEDs with the same parameters (e.g. mass, spin, time-averaged luminosity, and accretion rate) as those of BBHs, ensuring that only SED shapes are changing, as shown in Figure 3.2.

They exhibit a similar trend to BBHs: as the black hole mass increases, the thermal bumps appear at lower frequencies, attributed to the lower temperatures associated with the increasing mass of black holes.

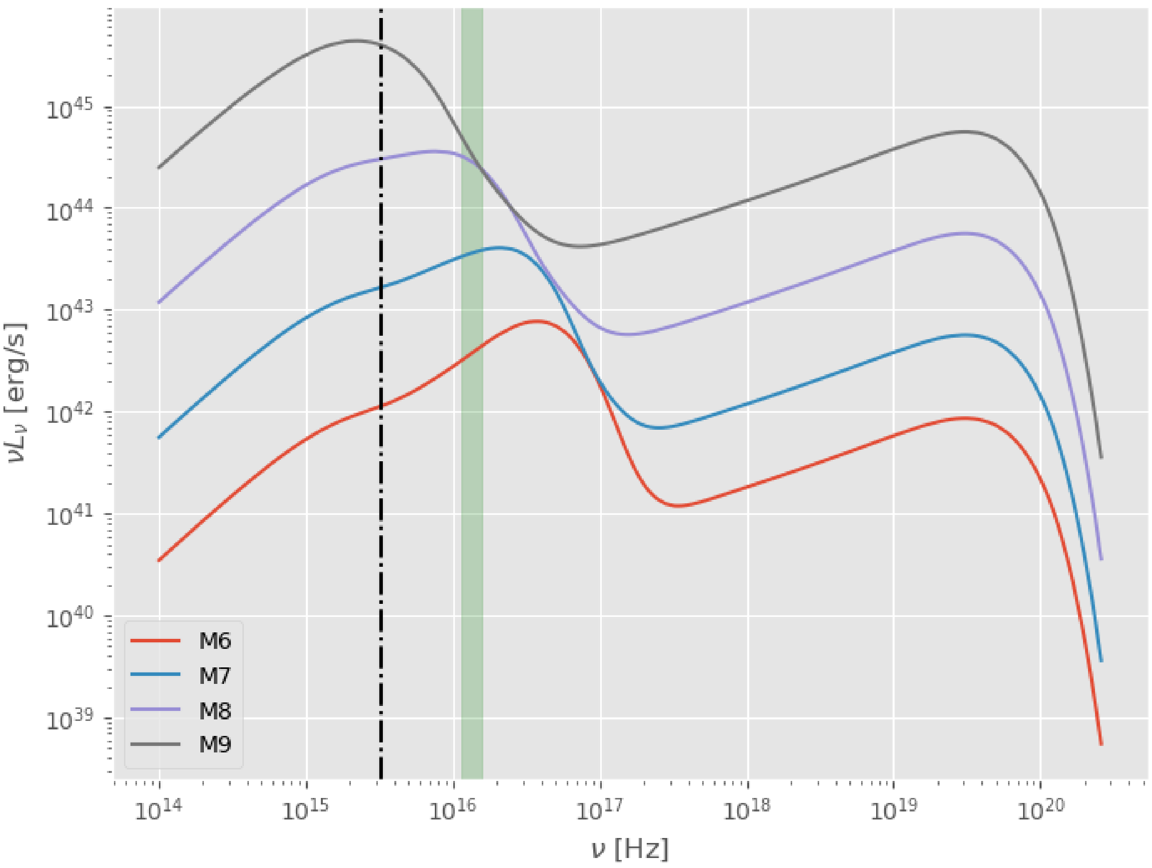

Figure 3.2: Time averaged SBH SEDs simulated by OPTXAGNF, illustrated as four models in different colors: M6 (red), M7 (blue), M8 (violet), and M9 (gray). The black dashed line denotes the ionization frequency for hydrogen. The green shaded area highlights the CIV ionization range, spanning from 44.89 to 64.49 eV.

3.3.1 Effects of $f_{\rm pl}$ on SBH SEDs

To investigate whether the parameter $f_{\rm pl}$, which is the fraction of the corona power emitted in the hard power-law component, will affect the continuum level in the ultraviolet/optical range, we tried several values for this parameter.

Although different values of $f_{\rm pl}$ affect the magnitude of L_λ in the X-ray range, they do not alter the slope or magnitude at the optical or ultraviolet range at all. Therefore, the continuum level involved in the EW calculations will stay the same, no matter the choice of $f_{\rm pl}$.

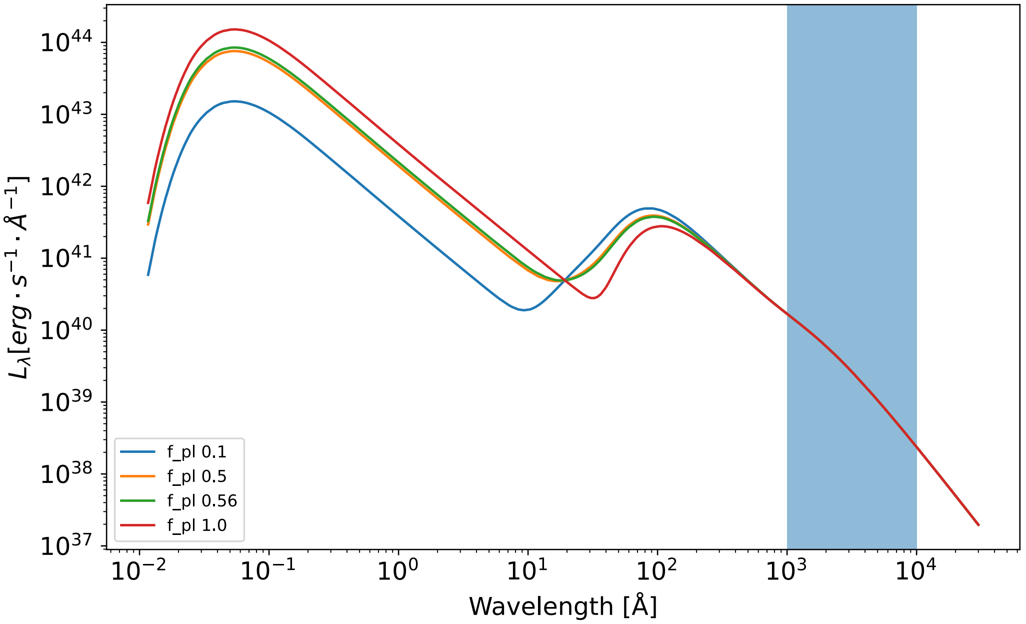

Figure 3.3: Different values for $f_{\rm pl}$ in OPTXAGNF. Four lines in different colors represent different values of $f_{\rm pl}$: $f_{\rm pl} = 1.0$ (red), $f_{\rm pl} = 0.56$ (green), which is what we used to run the BELMAC simulation and calculate the equivalent width, $f_{\rm pl} = 0.5$ (orange), and $f_{\rm pl} = 0.1$ (blue). The shaded blue area indicates the spectral region containing the optical and ultraviolet emission lines we are interested in.

3.4 SED Comparison

The shapes of the SEDs for BBHs and SBHs, illustrated in Figure 3.1 and Figure 3.2, respectively, exhibit stark differences. Notably, the low-frequency slope of the BBH SEDs is steeper than that of the SBH SEDs, which is expected to yield differences in the equivalent widths of broad emission lines, as will be discussed in Chapter 5.

The critical spectral range for photoionization lies within the domain where $h\nu \geq 13.6$ eV. This domain encompasses photons capable of ionizing hydrogen atoms, which are the most abundant in gas clouds, along with other atoms possessing higher ionization potentials.

To identify the disparities in the photoionization domain between BBH and SBH SEDs, we plotted SEDs of both binary and single black holes on top of each other, as shown in Figure 3.4. In Figure 3.4, the biggest difference lies in the $10^6 M_\odot$ case, where the thermal

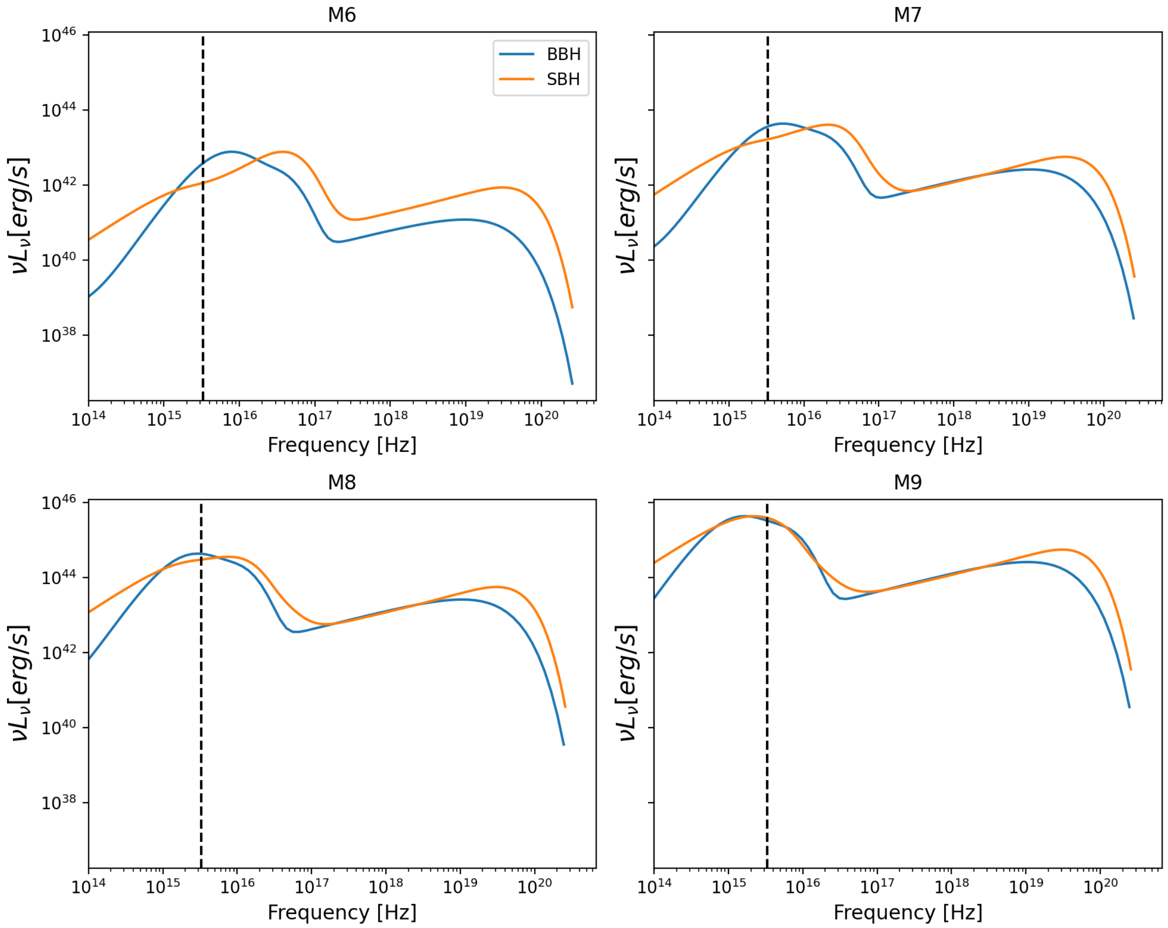

Figure 3.4: Comparison between binary and single black holes' SEDs. The title for each subplot indicates the total mass of black holes. Colors indicate the configuration of black holes: BBH (blue) and SBH (orange).

peak between BBH and SBH SEDs is separated at the farthest frequency range. As the total mass of black holes increases, both thermal peaks in binary and single black holes' SEDs shift to lower frequencies. However, the thermal peak in the SBH SEDs shifts farther than that of BBH SEDs. The main reason for this is that the binary system contains the cavity between the circumbinary disk and minidisks while the SBH does not. With an increased total mass, the ISCO radius of the black hole increases. However, for the BBH, an increased ISCO radius mostly affects the minidisks instead of the circumbinary disk. It is the circumbinary disk that dominates the thermal emission. Therefore, the circumbinary disk's temperature in the high-mass binary system remains similar to that of the low-mass binary system. Conversely, the accretion disk in the SBH is continuously distributed around the black hole, with no cavity at all, making the effect of an increased ISCO radius transmitted through the entire disk and lowering the temperature to a greater extent than that of BBHs.

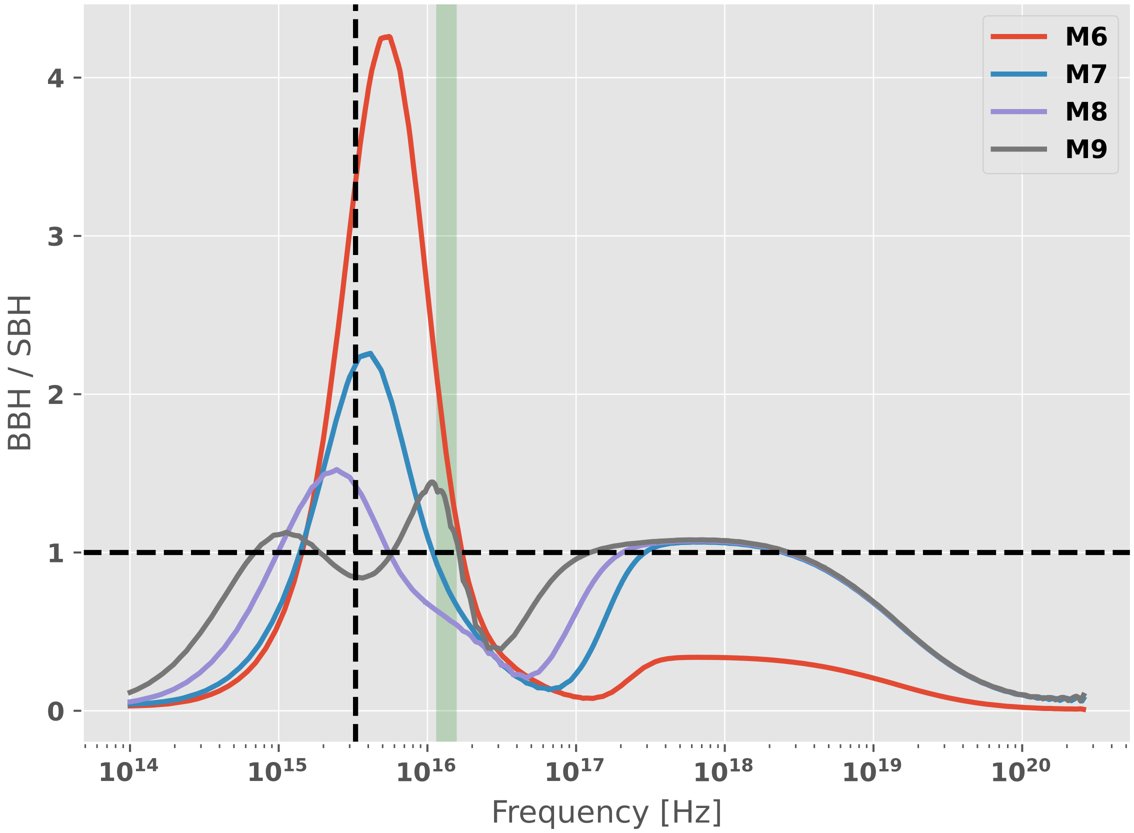

Figure 3.5: A SED ratio plot, BBH/SBH. Four models in different colors: M6 (red), M7 (blue), M8 (violet), and M9 (gray). The black dashed line denotes the ionization frequency for hydrogen. The green shaded area highlights the CIV ionization range, spanning from 44.89 to 64.49 eV.

It is because the two thermal peaks, both of binary and single black holes, separate at the greatest frequency range in the case of $10^6 M_\odot$ of the total black holes' mass that Figure 3.5 shows the biggest difference in this case. Also, with the total mass of black holes increasing, both thermal peaks approach each other and finally overlap in the case of $10^9 M_\odot$ of the total mass of black holes, corresponding to the diminishing thermal peak ratio in Figure 3.5.

3.5 Accretion-Disk SEDs + Galaxy SEDs

SEDs observed by telescopes usually include not only an accretion-disk continuum but also an often significant contribution from the host galaxy. To simulate these observed SEDs accurately, we combined galaxy SEDs with the accretion-disk SEDs of SBHs and BBHs. The reason why it is important to account for the galaxy's contribution to the SEDs is that it will affect the continuum level, which in turn will alter the equivalent widths of the emission lines. Therefore, with galaxy SEDs included, we can predict more realistic line equivalent widths.

We obtained a set of galaxy SEDs from Brown et al. (2014) and chose the SED of an elliptical galaxy, NGC4125. This choice is justified by the fact that it typically takes about 10^8 years for a BBH system to evolve from the gravitationally bound stage to the gravitational-wave dominated stage (Bogdanovi et al., 2022), a period during which some star-forming activities cease. Moreover, after a major merger, the remnant galaxy will eventually become an elliptical galaxy in which the gas is consumed and dispersed and the activities of star formation are ceased (Hopkins et al., 2008). Therefore, by incorporating the NGC4125 SED into the accretion-disk SEDs, we produced SEDs that more closely resemble those observed by telescopes, including both the accretion-disk continuum and host-galaxy continuum.

To produce Figure 3.6, Figure **??**, Figure **??**, and Figure 3.7, we combined galaxy SEDs with the accretion-disk SEDs based on the Equation 3.5.7:

$$\text{Combined Continuum} = \text{galaxy continuum} + \text{ Accretion-Disk continuum} \tag{3.5.7}$$

, where I used the actual luminosity of the NGC4125 galaxy, which is calculated by using $L = 4\pi r^2 \cdot$ flux.

As shown in Figure 3.6, the accretion-disk continuum differs between the BBH and SBH for a BH mass of $10^6 M_\odot$, particularly in the slope at the high-energy range. This difference is primarily due to the bump in the circumbinary disk, which is caused by an overdensity at its inner edge, resulting in a higher temperature compared to the rest of the disk. The two

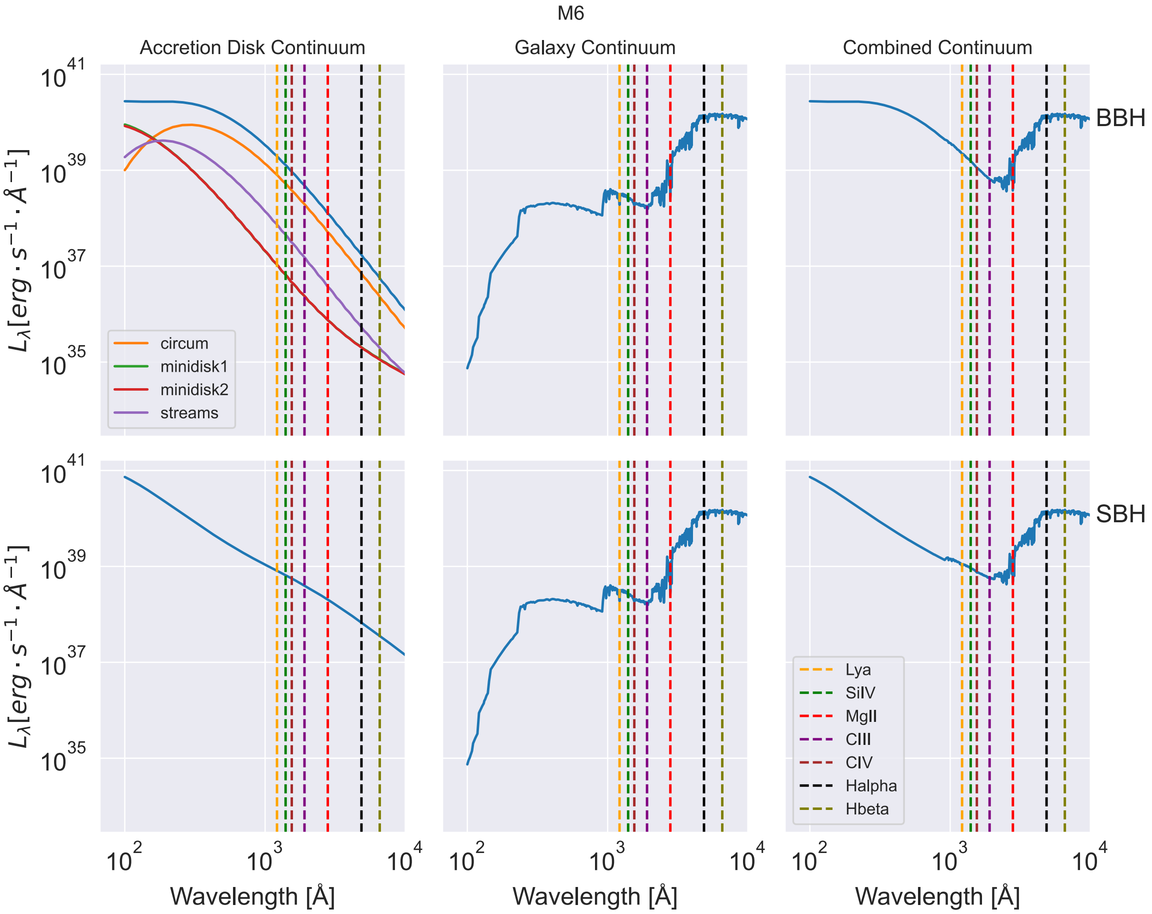

Figure 3.6: An UV-NIR SED for three continua for a BH mass of $10^6 M_\odot$: (1) Accretion-Disk Continuum, (2) Galaxy Continuum, and (3) Combined Continuum with the previous two continua being added together. The top panel shows the BBH SEDs, whereas the bottom one shows the SBH SEDs. For the BBH SED, the various components are: a circumbinary disk (orange), two minidisks (green + red), and streams (purple). The total emission with these components combined are denoted in blue. The galaxy continuum we chose is that of NGC4125, which is an elliptical galaxy. The dashed lines here denote all the emission lines we used: Lyα (orange), SiIV (green), MgII (red), CIII] (purple), CIV (brown), Hα (black), and Hβ (olive).

minidisks exhibit a similar slope to the single disk of the SBH.

Additionally, the galaxy continuum has a comparable specific luminosity (L_λ) to that of the accretion-disk continuum, leading to an upturn in the combined continuum at wavelengths > 3000 Å.

When the BH mass increases to $10^9 M_\odot$, the differences between the accretion-disk continua

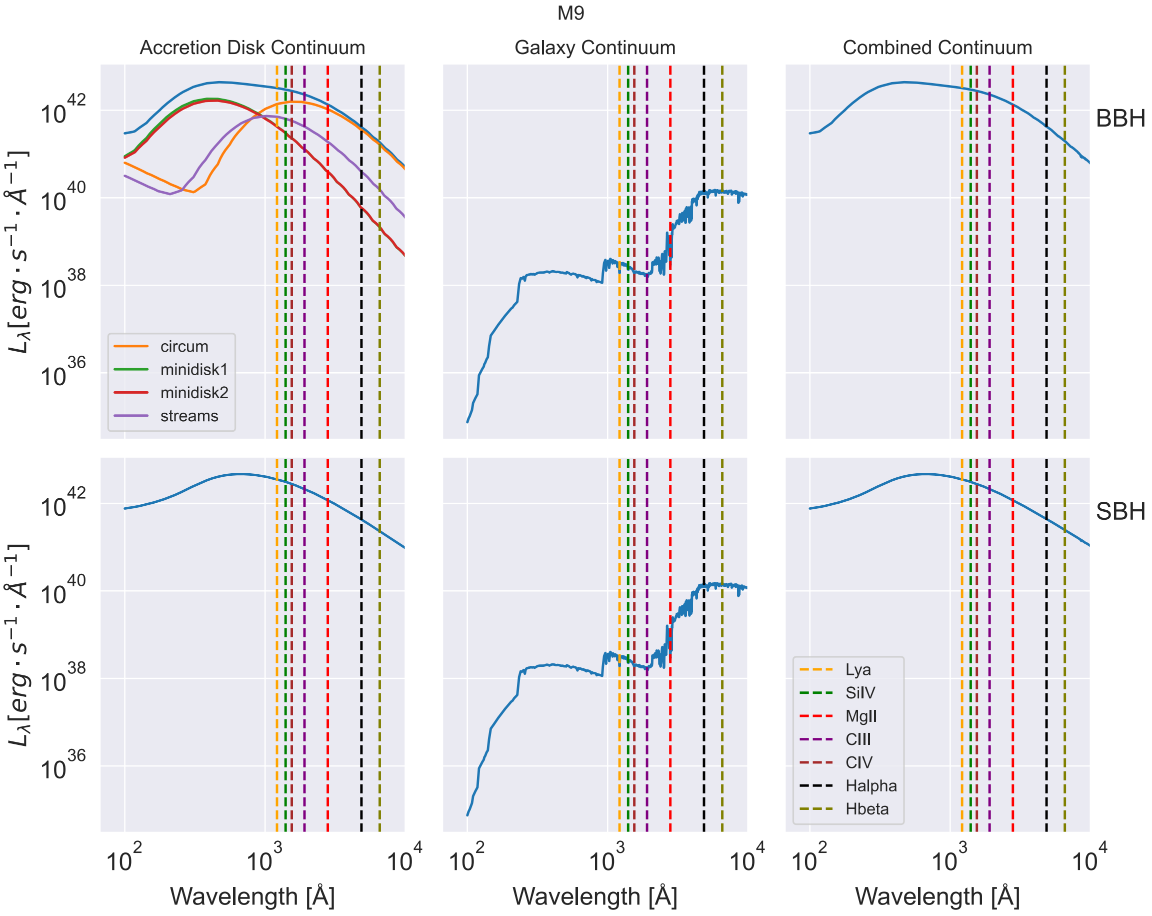

Figure 3.7: An UV-NIR SED for three continua for a BH mass of $10^9 M_\odot$: (1) Accretion-Disk Continuum, (2) Galaxy Continuum, and (3) Combined Continuum with the previous two continua being added together. The top panel shows the BBH SEDs, whereas the bottom one shows the SBH SEDs. For the BBH SED, the various components are: a circumbinary disk (orange), two minidisks (green + red), and streams (purple). The total emission with these components combined are denoted in blue. The galaxy continuum we chose is that of NGC4125, which is an elliptical galaxy. The dashed lines here denote all the emission lines we used: Lyα (orange), SiIV (green), MgII (red), CIII] (purple), CIV (brown), Hα (black), and Hβ (olive).

of BBHs and SBHs diminish. As shown in Figure 3.7, while the two minidisks have a different slope in their SED compared to the single disk of an SBH, emission from the circumbinary disk compensates for this difference. The overdensity in the circumbinary disk now appears in the low-energy range.

For the combined continuum, there is a minimal contribution from galaxy contamination because the specific luminosity of the host galaxy is negligible compared to the accretion-disk continuum.

In this project, as an example, we only selected one specific galaxy with a certain luminosity. As the equivalent width depends on the continuum flux density at the line wavelength, it will change if the continuum flux density changes. Here we combined a galaxy continuum with the accretion-disk continuum, causing the equivalent width to decrease. Generally, the brightness of the galaxy continuum scales with the stellar mass of the galaxy. Therefore, with a greater number of stars, the galaxy continuum will be higher, which will result in a decrease in the equivalent width of emission lines. Conversely, with a smaller number of stars, the galaxy continuum will be lower, causing an increase in the equivalent width of emission lines, which is what we have done in this project.

Chapter 4

Results of Broad Line Region Models

4.1 Overview

In this chapter, we present the results we obtained by using the single-cloud models and cloud-ensemble models described in Chapter 2. To distinguish BBHs from SBHs, we compare the predicted emission-line ratios and EWs between the two cases. Firstly, the single-cloud models were investigated because it is the simplest case and while it is not a realistic representation of the BLR, it provides insights into how the different SEDs affect the photoionization models. Additionally, as we mentioned in Section 2.4.1, we placed this single cloud at three different locations: 1R, 2R, and 4R, where R is the BLR radius calculated by the radius-luminosity relationship (Eq. 2.2.1).

In the single-cloud cases, we tried to investigate the emission-line ratios first because there is already a diagnostic method called Baldwin-Phillips-Terlevich (BPT) diagrams (Baldwin et al., 1981), which can separate the star-forming regions and AGNs by plotting certain emission-line ratios. As shown in Figure 4.1, Kewley et al. (2006) used optical emission lines, such as [OIII], [NII], [SII], and [OI], to distinguish between the HII regions associated with star formation and AGNs, based on the idea that the two regions have different line ratios.

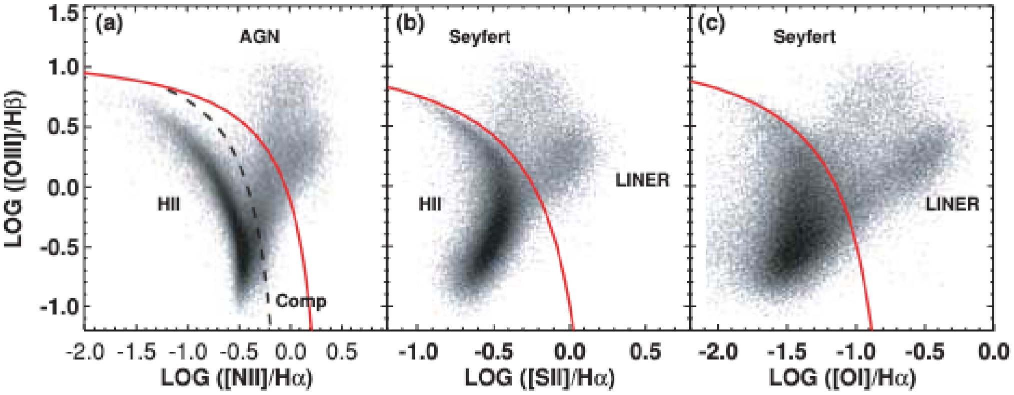

Figure 4.1: BPT diagrams. The red solid line represents the maximum starburst line, indicating the upper limit of the theoretical pure star-forming regions. Galaxies that are above this line are possible to be dominated by an AGN, whereas the region below is dominated by star formation. The black dashed line here is an empirical line dividing pure star-forming galaxies from galaxies that have both star-formation and AGN activities. Therefore, the 'Comp' in (a) means that the region is a composite object that has both star formation and AGN activities. Adapted from Kewley et al. (2006).

Similarly, we expected that for binary and single black holes, the emission-line ratios would also be different, and therefore we constructed BLR line-ratio diagrams using the ultraviolet emission lines Si IV λ1400Å, C III] λ1909Å, C IV λ1549Å, Mg II λ2798Å, and Lyα λ1216Å. While there are some differences in emission-line ratios between BBHs and SBHs, they are not big enough for the two black hole cases to occupy two different zones. Therefore, we switched to the equivalent widths, which can probe the difference in SED shapes between binary and single black holes.

The equivalent width is a ratio between the flux of an emission line and the underlying continuum flux density at that line wavelength. Therefore, if the line flux is similar in binary and single black holes, the equivalent widths will still be different because the SED shapes differ. Happily, the EWs of certain emission lines, such as Lyα, CIV, and Hα, do show a big difference between BBHs and SBHs for the mass range from 10^6 to $10^8 M_\odot$. The difference becomes insignificant at the black hole mass of $10^9 M_\odot$.

After we found differences in the line EWs between BBHs and SBHs for photoionization models of a single cloud, we continued our investigation for a more realistic representation of the BLR, which is a cloud ensemble. By using BELMAC with multiple combinations of input parameters, such as the gas density and its power-law distribution parameter, and excluding the effect of reverberation mapping, we generated a group of line luminosities of those selected emission lines and calculated their EWs by dividing the line luminosity with the continuum luminosity under each line.

To find out which combination of parameters matches the observed results, we obtained the observed EWs from the SDSS DR7 Quasar Catalog, which contains 105,783 objects from SDSS DR7 (Shen et al., 2010). Shen et al. (2010) only includes EWs for MgII, CIV, Hα, and Hβ. From this dataset, we calculated mean EWs and their standard deviations to compare them with the predicted values of our EWs between BBHs and SBHs. As our models utilize four different masses, we classified the observed EWs into four different black hole masses as well. However, there are no objects in this catalog whose black hole mass falls into the $10^6 M_\odot$ band, so we were unable to compute mean EWs for comparison with the $10^6 M_\odot$ cases.

4.2 Single Cloud Models

4.2.1 BLR BPT Diagrams

As discussed in Section 2.4.1, we have chosen different combinations of parameters, such as the distance between the cloud and the central luminous source and the column density, to investigate whether there will be any difference in line ratios between BBHs and SBHs.

Due to the novelty of this method, we don't know which combination of lines can distinguish between BBHs and SBHs. Consequently, we tried all the combinations of lines to accomplish that goal.

The BLR BPT diagrams are separated into four different black hole masses: $10^6 M_\odot$, $10^7 M_\odot$, $10^8 M_\odot$, and $10^9 M_\odot$. However, after examining all the combinations of line ratios, we found that only a couple of line combinations for a black hole mass of $10^8 M_\odot$ marginally satisfy the goal of distinguishing BBHs from SBHs: SiIV λ1400 Å vs. CIII] λ1909 Å and SiIV λ1400 Å vs. MgII λ2798 Å, where all lines are in relative strengths with respect to Ly

α λ1216 Å as shown in Figure 4.2 and Figure 4.3. For the sake of completeness, we present the rest of the BLR BPT diagrams in Appendix A.

For most of the data points in both figures, the SBH data exhibits a higher SiIV/Lyα ratio than that of BBH because the ionization structures of the clouds differ. However, the difference in those line ratios is only about 0.08%. Usually, in observational datasets, the data comes along with statistical and systematic uncertainties. When comparing the observational data with the simulated data, these uncertainties will likely obscure the 0.08% difference, making it difficult to distinguish between binary and single black holes. Therefore, this method fails to distinguish between BBHs and SBHs. We need to try another method.

Although this method fails, there are still some interesting trends in the data that follow our expectations.

First, as shown in Figure 4.3, BBHs and SBHs share the same trend: the value of SiIV/Lyα decreases while the value of MgII/Lyα increases as the distance between the central luminous source and the single cloud increases. This is because the ionization parameter follows $U \propto Qr^{-2}$ with a given gas density. Therefore, with a given Q, the ionization parameter will decrease as the radius increases. The variation of the ionization parameter will affect the line ratios based on the line properties whether the line is low-ionization or high-ionization. To determine whether a line is low-ionization or high-ionization, we need to know its ionization potential energy. For example, the line SiIV has an ionization potential of 33.49 eV, whereas the line MgII has an ionization potential of 7.65 eV. Therefore, SiIV is a high-ionization line while MgII is a low-ionization line.

Due to the disparity of the ionization properties of both lines, the trends differ: SiIV/Lyα decreases while MgII/Lyα increases. On one hand, SiIV is a high-ionization line; therefore, when the ionization parameter decreases, the ionization flux that can ionize the SiIV becomes smaller, causing the line ratio smaller as the radius increases. On the other hand, MgII is a low-ionization line. The increase in this line ratio is because as the ionization parameter decreases, fewer MgII ions are photoionized to MgIII.

It is intriguing to see the different behaviors of lines in Figure 4.2 because in contrast to

MgII λ2798 Å, CIII] λ1909 Å is an intermediate-ionization line. As indicated by the semi-square bracket, it is a semi-forbidden line that occurs in the BLR and its presence implies an upper limit for the gas density within the BLR. Although the behaviors are opposite between SiIV λ1400 Å and CIII]λ1909 Å, the change in the value of CIII]/Lyα is relatively small. Therefore, we may conclude that the value of SiIV/Lyα generally decreases while the value of CIII]/Lyα either increases (for the BBH case), or decreases (for the SBH case) by a smaller amount.

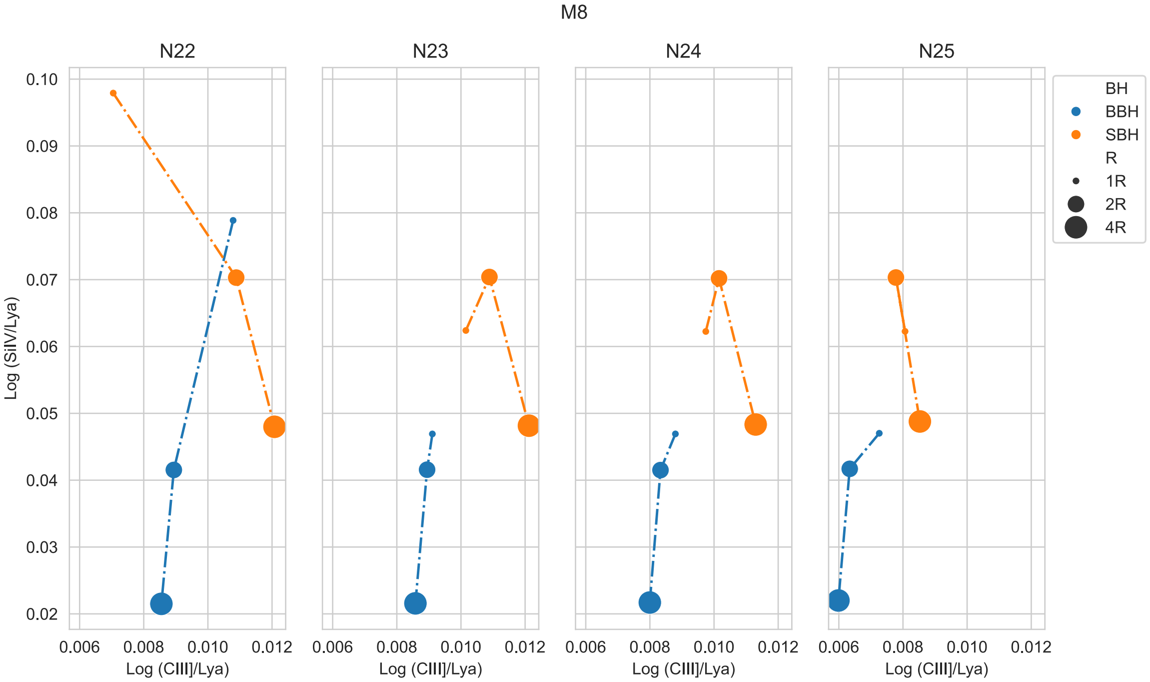

Figure 4.2: A BLR BPT diagram for a black hole mass of $10^8 M_\odot$. The x-axis represents the line ratio between SiIV λ1400 Å and Lyα λ1216 Å. the y-axis represents the line ratio between CIII] λ1909 Å and Lyα λ1216 Å. The configurations of BHs are represented in two colors: SBH (orange) and BBH (blue). From left to right, the column density increases by a factor of 10, from 10^{22} cm^{-3} to 10^{25} cm^{-3}.

4.2.2 EW Diagrams

Next, we tried equivalent width (EW) to probe the shape difference in SEDs between binary and single black holes. EW measures the ratio between total line flux and the underlying continuum flux at the line wavelength:

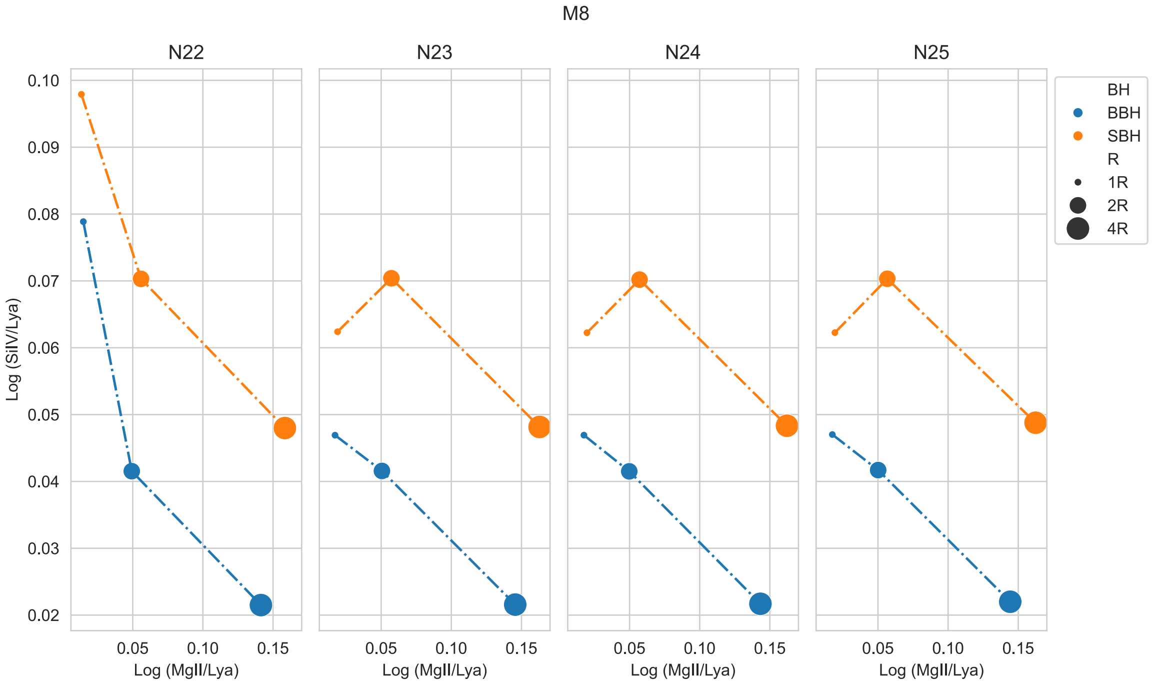

Figure 4.3: A BLR BPT diagram for a black hole mass of $10^8 M_{\odot}$. The x-axis represents the line ratio between SiIV λ1400 Å and Lyα λ1216 Å. the y-axis represents the line ratio between MgII λ2798 Å and Lyα λ1216 Å. The configurations of BHs are represented in two colors: SBH (orange) and BBH (blue). From left to right, the column density increases by a factor of 10, from 10^{22} cm^{-3} to 10^{25} cm^{-3}.

Element	U_{ion} level 1 (eV)	U_{ion} level 2 (eV)	U_{ion} level 3 (eV)
Hydrogen (H)	13.6	—	—
Carbon (C)	11.26	24.38	47.89
Magnesium (Mg)	7.65	15.04	80.14
Silicon (Si)	8.15	16.35	33.49

Table 4.1: Ionization energy for three ionization states of 4 selected elements, where U_{ion} denotes the ionization energy.

$$EW = \frac{F}{F_{c,\lambda}} \tag{4.2.1}$$

, where F is the total line flux and $F_{c,\lambda}$ is the underlying continuum flux density at the line wavelength, which is determined from the corresponding SED, either of binary or single black holes. Here, we also computed the line flux at three different BLR radii. As the BLR radius increases, the ionization parameter decreases, resulting in a change in the line flux. For a given SED, the continuum remains constant. Therefore, the line EWs will vary as the radius increases.

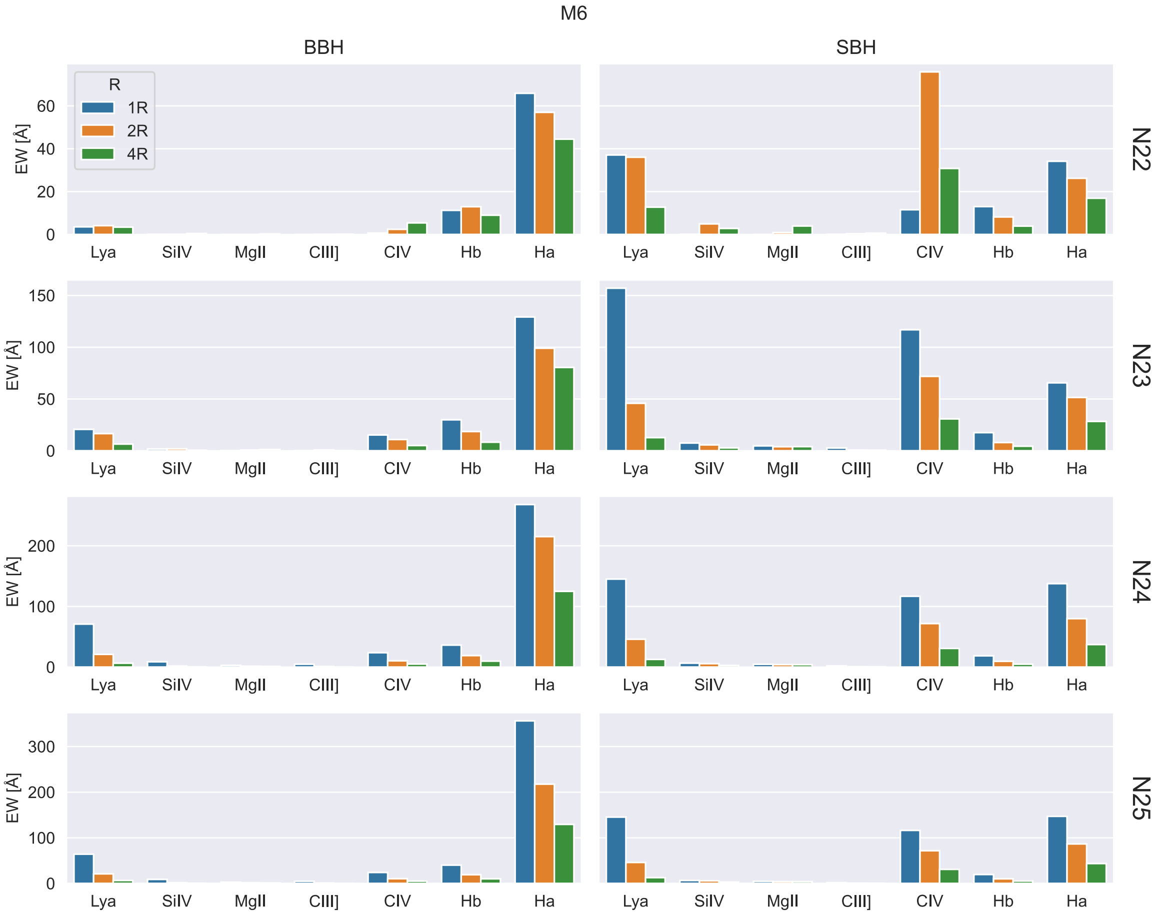

Figure 4.4: Equivalent width for M6 predicted by single-cloud photoionization models. The left panel is BBH and the right one is SBH. For each line, there are three radii for EWs: 1R (blue), 2R (orange), and 4R (green). From the top panel to the bottom, the column density increases by a factor of 10 in the range from 10^{22} cm^{-2} to 10^{25} cm^{-2}.

Again, we have four different BH masses here: $10^6 M_\odot$, $10^7 M_\odot$, $10^8 M_\odot$, $10^9 M_\odot$. We include two EW plots predicted by single-cloud photoionization models for two total black hole masses: $10^6 M_\odot$ and $10^9 M_\odot$, as shown in Figure 4.4 and Figure 4.5. There are two reasons for this. First, only the case of black hole mass of $10^6 M_\odot$ exhibits the peculiar rise in CIV at the column density of 10^{22} cm^{-2}. Second, only the case of black hole mass of $10^9 M_\odot$ shows no substantial differences in line EWs between BBHs and SBHs. By comparing the line EWs between BBHs and SBHs across all black hole masses and column densities, we found that the Hα EWs of BBHs are much higher than those of SBHs, whereas the EWs of Lyα and CIV of SBHs are much higher than those of BBHs, as shown in Figure 4.4. These results hold when the black hole mass increases from $10^6 M_\odot$ to $10^8 M_\odot$. Therefore, we may be able to use these three lines Lyα, CIV, and Hα to distinguish between BBHs and SBHs. Although Hβ also shows slightly different EWs between BBHs and SBHs, this difference is small enough that it may be obscured by the noise and uncertainty in observational data.

In Figure 4.4, for the $10^6 M_\odot$ case, at the lowest column density 10^{22} cm^{-2}, there is a clear distinction between BBHs and SBHs in EWs of Lyα, CIV, and Hα. As the column density increases, Hα EW increases because the cloud is becoming more optically thick and captures more ionizing photons, resulting in more HI atoms being ionized. Interestingly, there is an inverse relationship between EW and radius for CIV of the SBH models at column density of 10^{22} cm^{-2}. At 1R, the ionization parameter is so high that most CIV ions are ionized to higher states, such as CV. When the radius increases to 2R, the CIV flux increases as the ionization parameter decreases to a level where CIV dominates the cloud. Apart from this apparent behavior, SIV shows similar behavior but its EW is much smaller. MgII and CIII] should increase as R increases, but they are also relatively weak so it's hard to see any trend in Figure 4.4. The strengths of the Hydrogen lines decrease as R increases because the ionization parameter scales with R, where $U \propto r^{-2}$.

Some lines, such as SiIV, MgII, and CIII], do not show any EW in Figure 4.4. This does not indicate that their fluxes are zero; instead, their fluxes are much smaller than the underlying continuum level. Therefore, at the scale of the plot, the EWs are negligibly small when the line fluxes are divided by the underlying continuum flux at the line wavelength.

4.3 Cloud Ensemble Models – EW Diagrams

Since only the EW succeeded in distinguishing BBHs from SBHs in single-cloud models, we continued to use it to probe the differences between binary and single black holes.

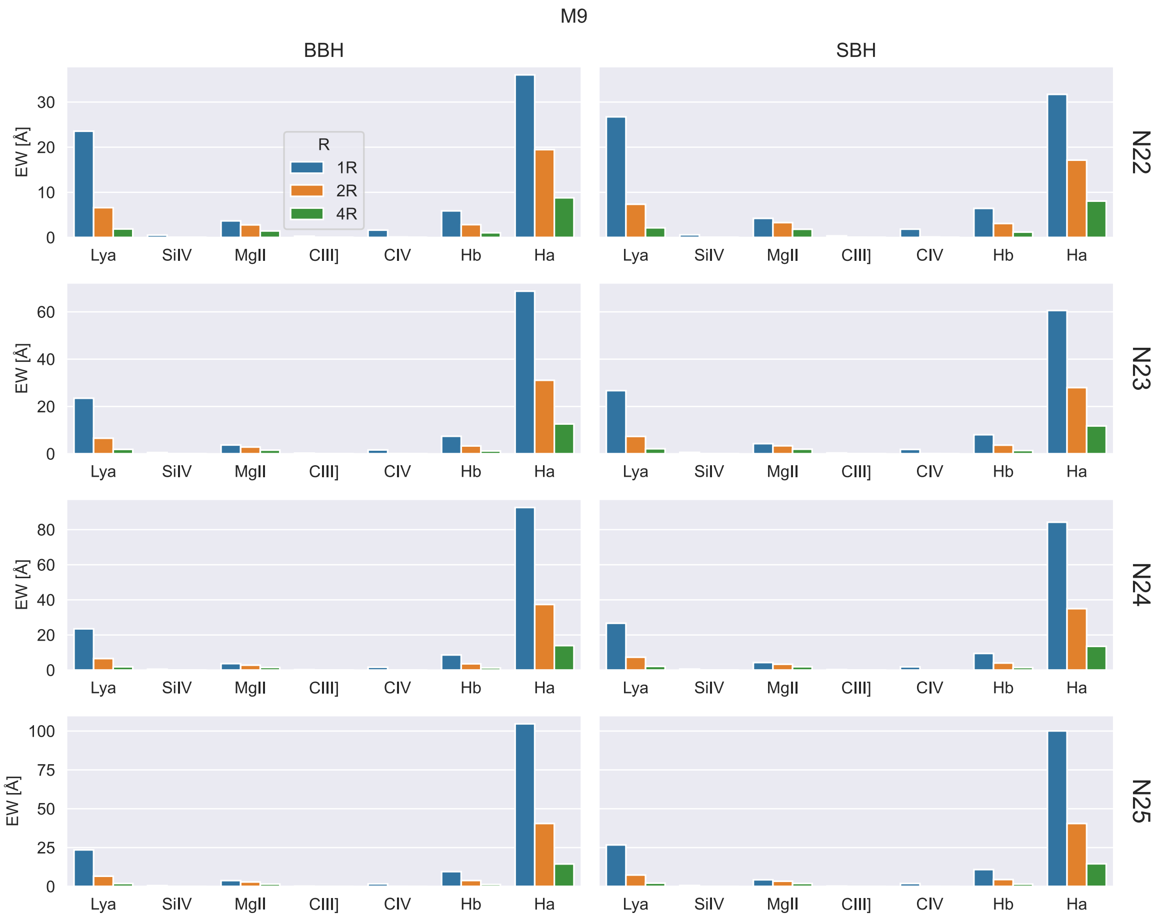

Figure 4.5: Equivalent width for M9 predicted by single-cloud photoionization models. The top panel is BBH EW and the bottom one is SBH EW. For each line, there are three radii for EWs: 1R (blue), 2R (orange), and 4R (green). From the left panel to the right, the column density increases by a factor of 10 in the range from 10^{22} cm^{-2} to 10^{25} cm^{-2}.

To be able to calculate the EWs, we need the line luminosity and continuum specific luminosities at the wavelengths of the selected lines. For the continuum specific luminosities, we derived them from the SEDs we have. For the line luminosity of a cloud ensemble, we used BELMAC, which takes in an AGN SED and outputs the line luminosity of the selected lines, excluding the effect of reverberation mapping. To run BELMAC, a Cloudy photoionization grid was computed for each SED with each total black hole mass. In total, 8 grids were computed. Each grid has 3 dimensions: $-5 \leq \log_{10} U \leq 1.5$, $7.5 \leq \log_{10}(n/1 \text{ cm}^{-3}) \leq 15$, and $19 \leq \log_{10}(N_{\text{col}}/1 \text{ cm}^{-2}) \leq 25$, with an increment of 0.25, 0.5, and 1, respectively. The grid also assumes solar abundance. BELMAC also requires the AGN bolometric luminosity (L_{bol}) and ionizing photon luminosity (Q), which are calculated from the corresponding SED, either of binary or single black holes. The specific values for AGN bolometric luminosity (L_{bol}) and ionizing photon luminosity (Q) are listed in Table 4.3. Moreover, the gas density (n) and its distribution were also specified, with the power-law index, s, controlling the distribution of the gas density, which in turn controls the ionization parameter as $U \propto r^{-s-2}$. Additionally, in our cloud-ensemble models, we assume the BLR is in a disk-like shape around the central luminous source, which is either a binary or single black hole. All the parameters we used in BELMAC are listed in Table 4.2.

As the gas density and its distribution within the BLR are not well known, we did a parameter exploration on both parameters to determine what combination of the two parameters generates the data that agrees with the observational data. As a first step, we tried two values of s: $s = 0$ and $s = -2$, where $U \propto r^{-2}$ and $U \propto$ constant, correspondingly. Next, for the gas density n, we selected four values: $\log_{10}(n/1\ \text{cm}^{-3}) = 9.5, 10.0, 10.5, 11.0$.

Parameter Description	Symbol	Values
Size scaled to R_d	Y	20
Angular width	σ	20°
Total number of clouds	N_{tot}	500,000
Inclination to observer	i	60°
Covering Fraction	C_f	0.3
Gas Density in a cloud at R_d	$\log n(R_d)$	9.5, 10.0, 10.5, 11.0 cm^{-3}
Power-law index for gas density	s	0, -2
Power-law index for cloud distribution	p	0

Table 4.2: Parameters that are used by BELMAC to set up cloud-ensemble models of the BLR.

By comparing the simulated EWs with the observed EWs in the SDSS DR7 Quasar Catalog, under the assumption that most quasars are powered by SBHs, we expect to see SBH EWs fall into the range of the observed EWs while the BBH EWs fall outside the range. The range of the observed EWs is calculated in three steps: first, we categorized the black hole mass into four different bins: (1) $5.5 \leq \log_{10} M_{\text{BH}}/1M_\odot \leq 6.5$, (2) $6.5 \leq \log_{10} M_{\text{BH}}/1M_\odot \leq 7.5$, (3) $7.5 \leq \log_{10} M_{\text{BH}}/1M_\odot \leq 8.5$, and (4) $8.5 \leq \log_{10} M_{\text{BH}}/1M_\odot \leq 9.5$; second, we calculated

Model	BH	$L_{\rm bol}$ (erg/s)	Q (photons/s)
M6	BBH	1.644×10^{43}	2.364×10^{53}
	SBH	1.807×10^{43}	1.111×10^{53}
M7	BBH	1.086×10^{44}	1.453×10^{54}
	SBH	1.191×10^{44}	1.020×10^{54}
M8	BBH	1.086×10^{45}	1.178×10^{55}
	SBH	1.187×10^{45}	1.167×10^{55}
M9	BBH	1.085×10^{46}	7.540×10^{55}
	SBH	1.177×10^{46}	7.357×10^{55}

Table 4.3: A table of AGN bolometric luminosity ($L_{\rm bol}$) and ionizing photon luminosity (Q) for 4 different total masses of binary and single black holes.

the mean observed EWs; and third, we computed the standard deviations.

Lastly, to explore the effect of the galaxy continuum on the line EWs, we added the observed SED of NGC4125 to the accretion-disk continuum.

Note that we only included the black hole mass of 10^7 and $10^9 M_\odot$ here because no quasar in SDSS DR7 Quasar Catalog has a black hole mass ranging from $10^{5.5}$ to $10^{6.5} M_\odot$. Results for a black hole mass of $10^8 M_\odot$ are included in Appendix B because they show similar results and do not have any unexpected peculiar behavior.

4.3.1 Constant Ionization Parameter: s = -2

In this section, we present results for cloud-ensemble models, in which $s = -2$, $n \propto r^{-2}$, and the ionization parameter is constant, for total black hole masses 10^7 and $10^9 M_\odot$.

For $s = -2$ and a black hole mass of $10^7 M_\odot$, as shown in Figure 4.6, the differences in line EWs between models of binary and single black holes are most apparent in the following cases: (1) Lyα, CIV, and Hα when the gas density $\log_{10}(n/1\ \mathrm{cm}^{-3}) = 9.5$, (2) Ly$\alpha$, CIV, H$\beta$ and Hα when the gas density $\log_{10}(n/1\ \mathrm{cm}^{-3}) = 10.0$, (3) Ly$\alpha$, MgII, and CIV when the gas density $\log_{10}(n/1\ \mathrm{cm}^{-3}) = 10.5$, and (4) CIV and H$\alpha$ when the gas density $\log_{10}(n/1\ \mathrm{cm}^{-3}) = 11.0$. Although these results succeeded in distinguishing BBHs from SBHs, there are some peculiar behaviors, such as the extremely high EWs in the case of the gas density of $\log_{10}(n/1\ \mathrm{cm}^{-3}) = 10.0, 11.0$. These high EWs are caused by the high line luminosities generated by BELMAC. Moreover, in the case of the gas density $\log_{10}(n/1\ \mathrm{cm}^{-3}) = 10.0$, the SBH line luminosity is

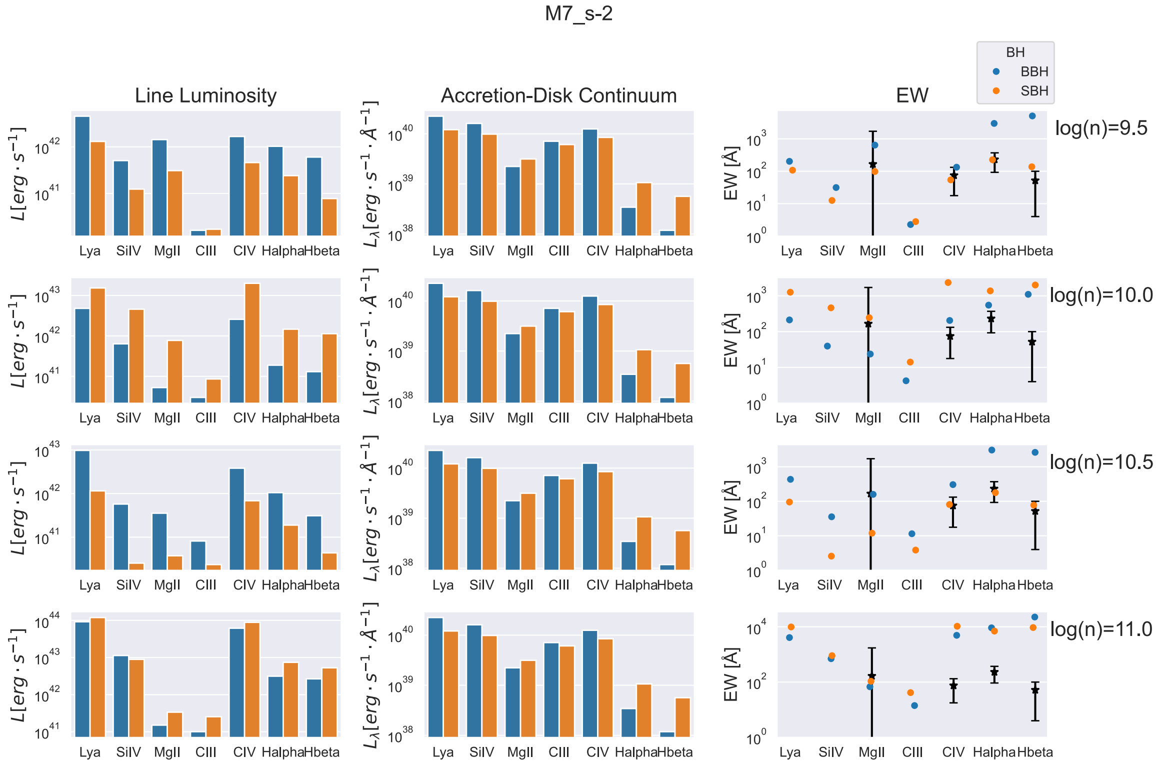

Figure 4.6: Cloud ensemble models for the BLR computed with BELMAC. Line luminosity, accretion-disk luminosity, and equivalent widths for a BH mass $10^7 M_\odot$ and $s = -2$. The color scheme here is: BBH denoted in blue and SBH denoted in orange. We have chosen seven emission lines, Si IV λ1400Å, C III] λ1909Å, C IV λ1549Å, Mg II λ2798Å, Lyα λ1216Å, Hα λ6562.80Å, and Hβ λ4861.32Å. There are three columns in the figure: from left to right, the first column shows the line luminosity, the second column shows the specific luminosity of the continuum of the accretion disk, and the third column shows the equivalent width, calculated by dividing the line luminosity by the continuum shown in the previous two columns. The black points with error bars show the mean and standard deviations of the observed EWs of MgII, CIV, Hβ, and Hα calculated using data from the SDSS DR7 Quasar catalog, for black hole masses in the range of $6.5 \leq \log_{10} M_{\mathrm{BH}} \leq 7.5$.

much higher than that of BBHs. The reasons for this high luminosity need to be investigated further in the future.

By comparing these predicted EWs of binary and single black holes with the observed EWs in the SDSS DR7 Quasar Catalog, we found that for some combinations of parameters, the predicted EWs agree with the range of the observed EWs: (1) MgII, CIV, and Hα in the case of $\log_{10}(n/1\ \mathrm{cm}^{-3}) = 9.5$, (2) MgII in the case of $\log_{10}(n/1\ \mathrm{cm}^{-3}) = 10.0$, (3) MgII, H$\alpha$, and H$\beta$ in the case of $\log_{10}(n/1\ \mathrm{cm}^{-3}) = 10.5$, and (4) MgII in the case of $\log_{10}(n/1\ \mathrm{cm}^{-3}) = 11.0$.

Interestingly, for CIV in case (3), the BBH EW falls outside the range of the observed EWs while that of SBH falls within, indicating that BBHs will differ in EWs from SBHs and become an outlier for the observed EWs. Therefore, we may be able to identify BBHs among SBHs by using this outlier behavior in the observational data.

When the black hole mass is $10^9 M_\odot$, as shown in Figure 4.7, the line luminosity for the gas density in the range of $10^{9.5}$ to $10^{10.5}$ cm^{-3} becomes much higher than the underlying continuum at the selected line wavelengths, resulting in extremely high line EWs. Generally, the results differ from those we obtained from single-cloud models because, unlike those models, which show little difference in EW between the BBH and SBH cases for a black hole mass of $10^9 M_\odot$, there are large differences in EW for gas densities $\log_{10}(n/1\ \mathrm{cm}^{-3}) = 9.5, 10.0, 10.5$ for lines: the Lyα, CIV, Hα, and Hβ ($\log_{10}(n/1\ \mathrm{cm}^{-3}) = 9.5$).

Intriguingly, there is an aberrant behavior shown in Figure 4.6 and Figure 4.7. In general, the EWs of the BBH models exceed those of the SBH models. However, when the gas density is 10^{10} cm^{-3}, the opposite is the case for all lines. This occurs because, as also shown in both figures, the line luminosity produced by BELMAC is higher in the case of single black holes. However, the reason for the higher line luminosity in the SBH case remains uncertain. It may suggest that this gas density is inappropriate for the simulation. We will investigate the code further to understand the calculations of line luminosity in the future.

4.3.2 Constant Gas Density: s = 0

In this section, we present results for cloud-ensemble models, in which $s = 0$, $n \propto$ Constant, and $U \propto r^{-2}$, for total black hole masses 10^7 and $10^9 M_\odot$.

For $s = 0$ and a black hole mass of $10^7 M_\odot$, as shown in Figure 4.8, the line EWs that differ between BBHs and SBHs are (1) MgII when the gas density $\log_{10}(n/1\ \mathrm{cm}^{-3}) = 9.5$ and (2) Lyα and CIV when the gas density $\log_{10}(n/1\ \mathrm{cm}^{-3}) = 10.5, 11.0$. Additionally, the line EWs that fall in the range of the observed EWs are (1) MgII when $\log_{10}(n/1\ \mathrm{cm}^{-3}) = 9.5, 10.0$ and (2) MgII and Hβ when $\log_{10}(n/1\ \mathrm{cm}^{-3}) = 10.5, 11.0$. By comparing the observed EWs with the simulated EWs, we can exclude some choices of parameters, such as CIV in the gas

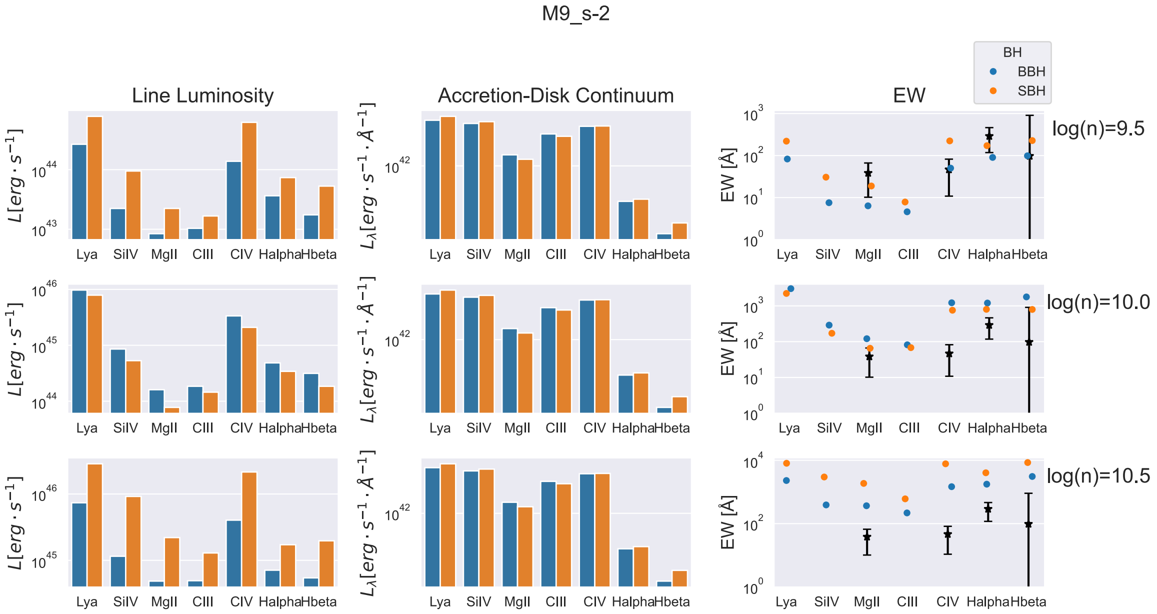

Figure 4.7: Cloud ensemble models for the BLR computed with BELMAC. Line luminosity, accretion-disk luminosity, and equivalent widths for a BH mass $10^9 M_\odot$ and $s = -2$. The color scheme here is: BBH denoted in blue and SBH denoted in orange. We have chosen seven emission lines, Si IV λ1400Å, C III] λ1909Å, C IV λ1549Å, Mg II λ2798Å, Lyα λ1216Å, Hα λ6562.80Å, and Hβ λ4861.32Å. There are three columns in the figure: from left to right, the first column shows the line luminosity, the second column shows the specific luminosity of the continuum of the accretion disk, and the third column shows the equivalent width, calculated by dividing the line luminosity by the continuum shown in the previous two columns. The black points with error bars show the mean and standard deviations of the observed EWs of MgII, CIV, Hβ, and Hα calculated using data from the SDSS DR7 Quasar catalog, for black hole masses in the range of $8.5 \leq \log_{10} M_{\rm BH} \leq 9.5$.

density of $\log_{10}(n/1\ {\rm cm}^{-3}) = 10.0, 11.0$ because its SBH EW falls outside the range of the observed EWs. Although there are differences between BBHs and SBHs in MgII at the gas density $\log_{10}(n/1\ {\rm cm}^{-3}) = 9.5$, their EWs both fall inside the range of the observed EWs, which makes it hard to distinguish between BBHs and SBHs in the observational dataset.

When the black hole mass is $10^9 M_\odot$, as shown in Figure 4.9, there is no difference in any line EW between BBHs and SBHs, which is consistent with the results we obtained in the single-cloud models.

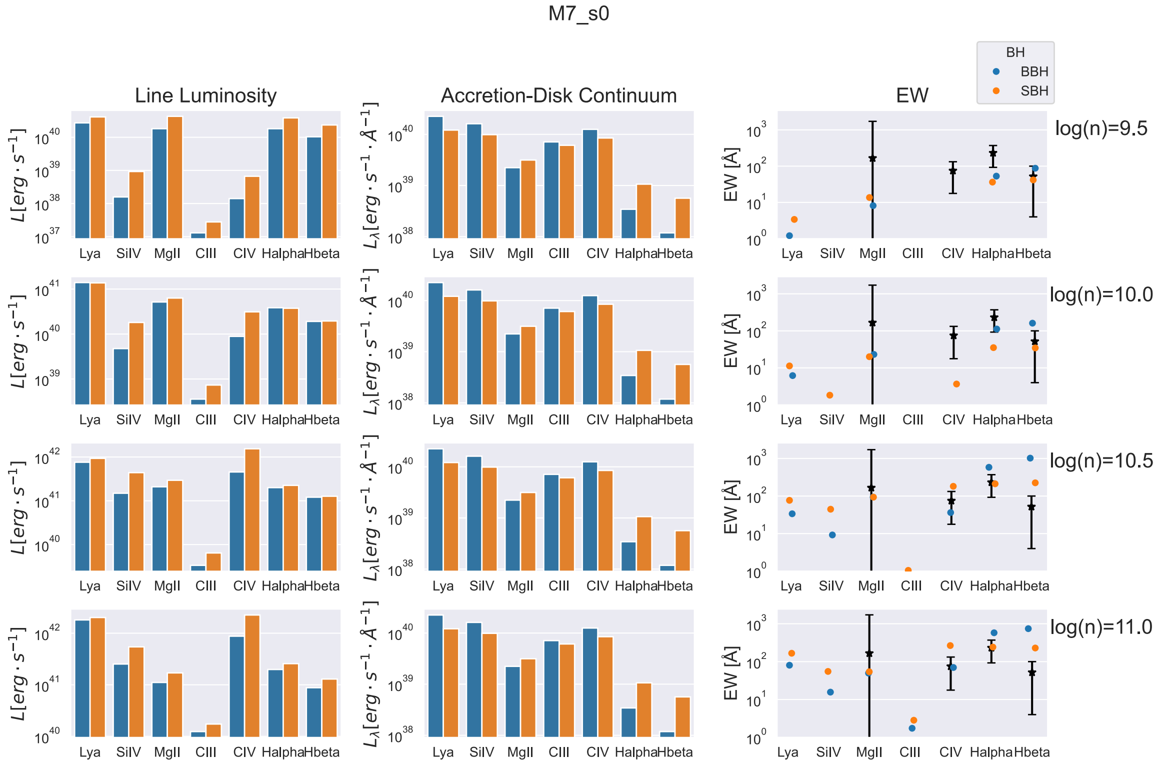

Figure 4.8: Cloud ensemble models for the BLR computed with BELMAC. Line luminosity, accretion-disk luminosity, and equivalent widths for a BH mass $10^7 M_\odot$ and $s = 0$. The color scheme here is: BBH denoted in blue and SBH denoted in orange. We have chosen seven emission lines, Si IV λ1400Å, C III] λ1909Å, C IV λ1549Å, Mg II λ2798Å, Lyα λ1216Å, Hα λ6562.80Å, and Hβ λ4861.32Å. There are three columns in the figure: from left to right, the first column shows the line luminosity, the second column shows the specific luminosity of the continuum of the accretion disk, and the third column shows the equivalent width, calculated by dividing the line luminosity by the continuum shown in the previous two columns. The black points with error bars show the mean and standard deviations of the observed EWs of MgII, CIV, Hβ, and Hα calculated using data from the SDSS DR7 Quasar catalog, for black hole masses in the range of $6.5 \leq \log_{10} M_{\rm BH} \leq 7.5$.

4.3.3 Effect of Galaxy SED onto the line EWs

In real life, a spectrum does not only show the continuum of the accretion disk but also shows that of the host galaxy. Therefore, in this section, we consider the effect of the galaxy SEDs on the line EWs. As shown in 4.10, the continuum flux density of the optical lines (Hβ and Hα) increases by an order of magnitude while that of UV lines is almost unaffected. The reason for this is that the galaxy continuum is higher in the optical range ($3,000 - 10,000$ Å)

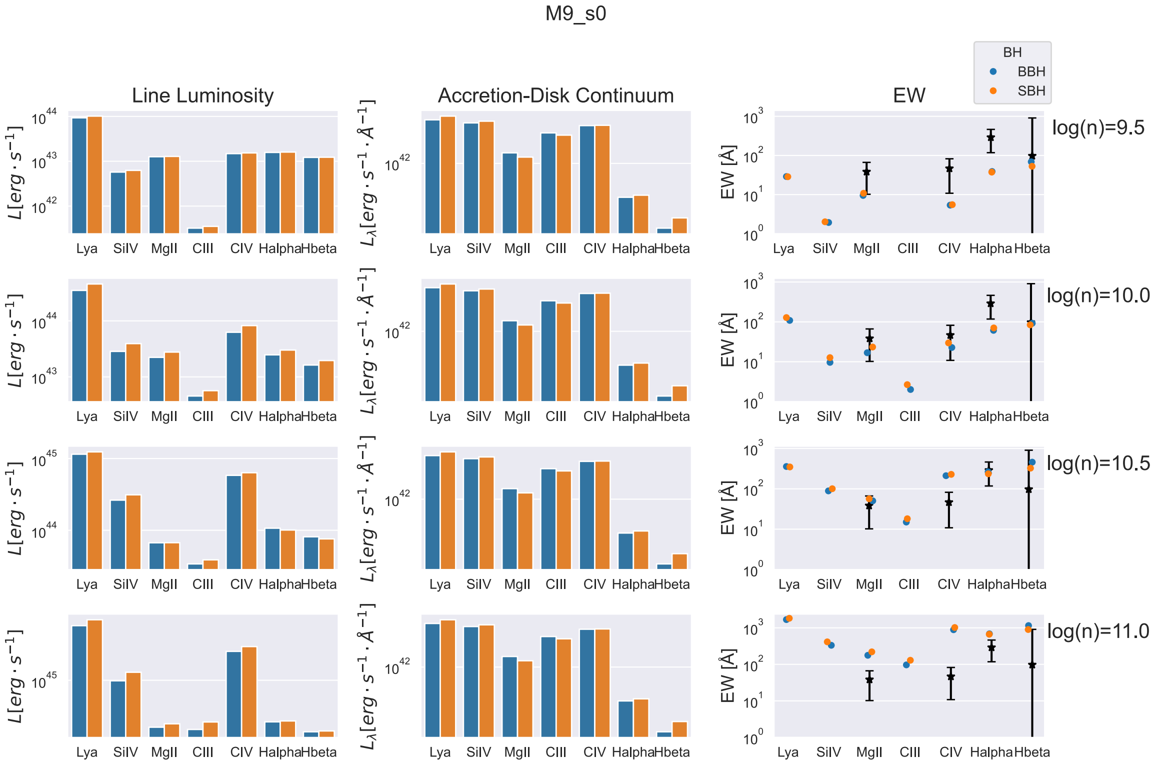

Figure 4.9: Cloud ensemble models for the BLR computed with BELMAC. Line luminosity, accretion-disk luminosity, and equivalent widths for a BH mass $10^9 M_\odot$ and $s = 0$. The color scheme here is: BBH denoted in blue and SBH denoted in orange. We have chosen seven emission lines, Si IV λ1400Å, C III] λ1909Å, C IV λ1549Å, Mg II λ2798Å, Lyα λ1216Å, Hα λ6562.80Å, and Hβ λ4861.32Å. There are three columns in the figure: from left to right, the first column shows the line luminosity, the second column shows the specific luminosity of the continuum of the accretion disk, and the third column shows the equivalent width, calculated by dividing the line luminosity by the continuum shown in the previous two columns. The black points with error bars show the mean and standard deviations of the observed EWs of MgII, CIV, Hβ, and Hα calculated using data from the SDSS DR7 Quasar catalog, for black hole masses in the range of $8.5 \leq \log_{10} M_{\rm BH} \leq 9.5$.

while in the UV range $(1,000 - 3,000$ Å), the galaxy continuum is much lower than the one of the accretion disk, making the optical lines mostly affected by the galaxy continuum while the UV lines are almost unaffected.

As brighter AGNs tend to live in brighter host galaxies, we scaled the galaxy contribution with a scaling factor, simply by multiplying a factor with the galaxy continuum of NGC4125.

As shown in Figure 4.11, the optical line EWs vary significantly with the scaling factor due to the higher luminosity of the galaxy continuum in the optical wavelengths (Figure 3.6). This

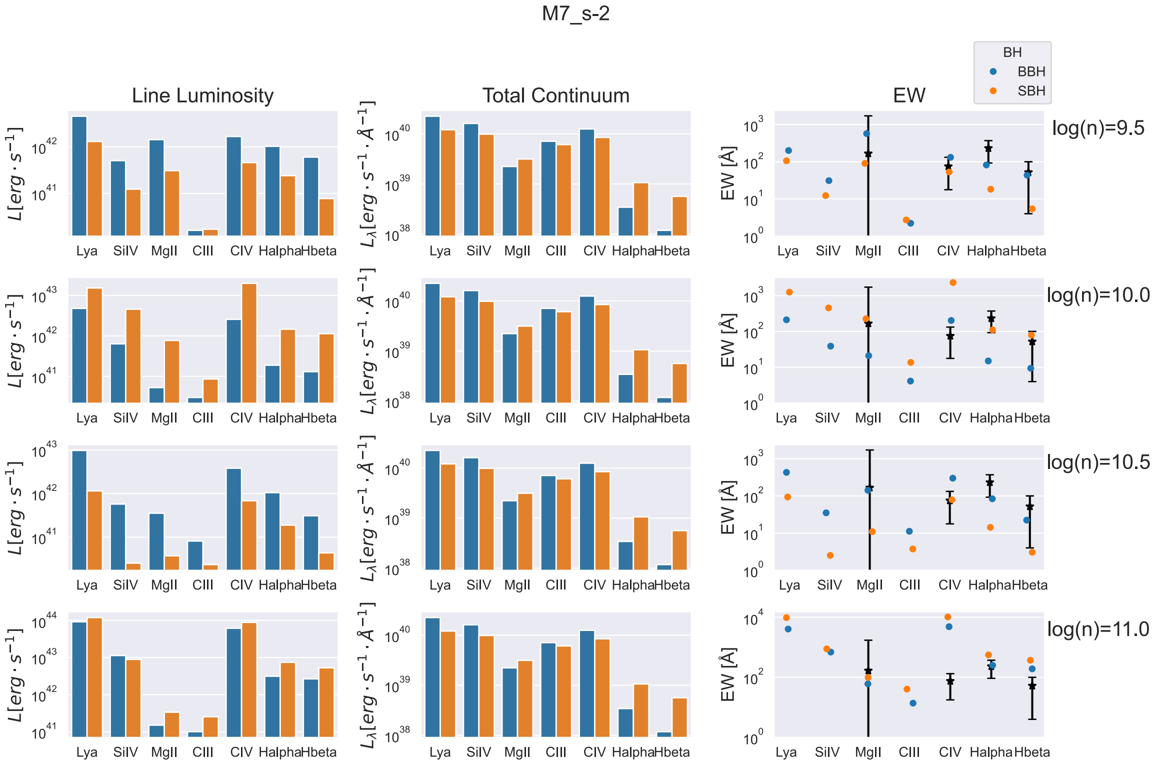

Figure 4.10: Line luminosity, total continuum including the galaxy continuum, and equivalent width for a BH mass $10^7 M_\odot$ and $s = -2$. The color scheme here is: BBH denoted in blue and SBH denoted in orange. We have chosen seven emission lines, Si IV λ1400Å, C III] λ1909Å, C IV λ1549Å, Mg II λ2798Å, Lyα λ1216Å, Hα λ6562.80Å, and Hβ λ4861.32Å. There are three columns in the figure: from left to right, the first column shows the line luminosity of all emission lines generated by BELMAC, the second column shows the specific luminosity of the continuum obtained by adding the accretion-disk continuum and galaxy continuum together, and the third column shows the equivalent width, calculated by dividing the line luminosity by the continuum shown in the previous two columns. The error bars in the third column are obtained by calculating the distribution of observed EWs in the SDSS DR7 Quasar Catalog. Moreover, the black points in the third column denote the mean observed EWs in the catalog.

galaxy exhibits higher optical luminosity than ultraviolet luminosity because it is an elliptical galaxy, characterized by a low star formation rate and a lack of young stars emitting ultraviolet light. Consequently, the galaxy continuum affects optical lines more than ultraviolet lines. This implies that if the spectrum is not corrected for the host galaxy continuum, for a brighter galaxy, it will be challenging to distinguish BBHs from SBHs using optical lines, as a portion of the optical-line emissions originates from the galaxy rather than the central BH. Therefore, careful modeling and removal of the host galaxy continuum is required.

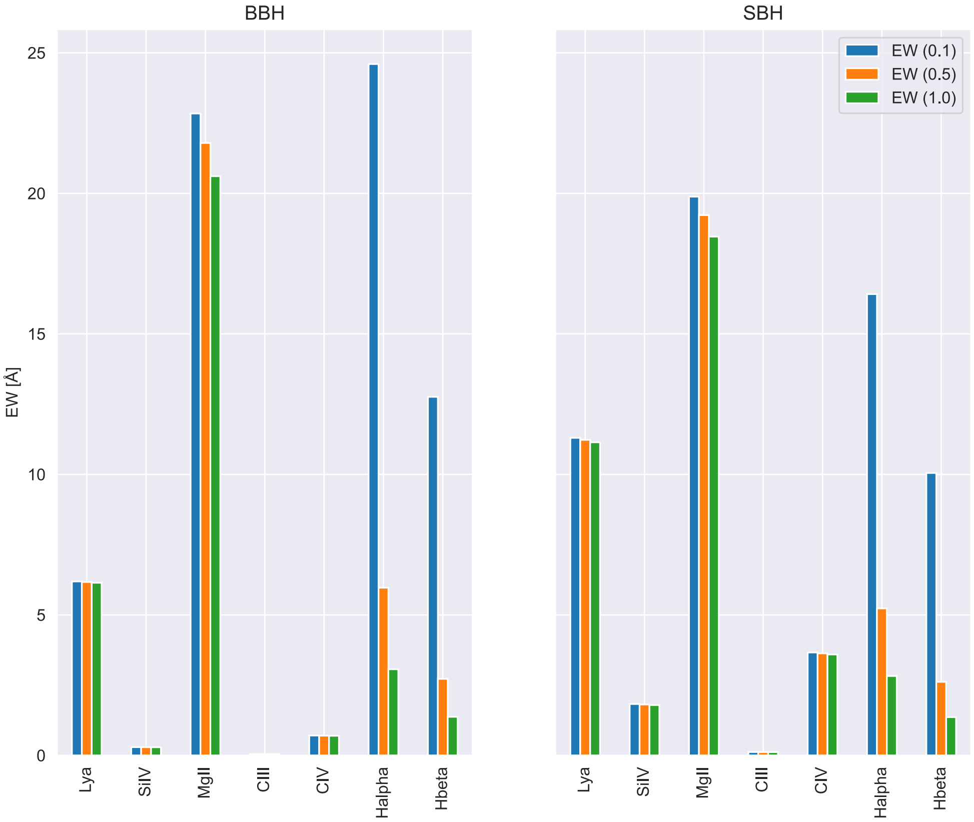

Figure 4.11: EWs between different scaling factors of the galaxy continuum of NGC4125 in the case of a $10^7 M_\odot$ black hole mass. The blue denotes the equivalent width with a scaling factor of 0.1, the orange represents the equivalent width with a factor of 0.5, and the green represents the equivalent width with a factor of 1.0. The lines we used here are: Si IV λ1400Å, C III] λ1909Å, C IV λ1549Å, Mg II λ2798Å, Lyα λ1216Å, Hα λ6562.80Å, and Hβ λ4861.32Å.

Chapter 5

Conclusion and Future Work

5.1 Conclusion

In this project, we aim to distinguish BBHs from SBHs by analyzing the differences in broad emission lines resulting from the different shapes of their accretion-disk SEDs. We obtained BBH SEDs from GRMHD simulations and SBH SEDs from OPTXAGNF modeling. To simulate the BLR response, we computed single-cloud photoionization models using Cloudy and cloud-ensemble photoionization models using BELPro. We then used emission-line ratios and equivalent widths to probe the differences between BBHs and SBHs. It turns out that emission-line ratios cannot clearly show the difference between both types of BHs while equivalent widths can in some circumstances.

- Firstly, for the single-cloud models, three broad emission lines can be used to distinguish between BBHs and SBHs: Lyα (higher EWs in BBHs), CIV (higher EWs in SBHs), and Hα (higher EWs in BBHs). But at the highest mass of BHs, $10^9 M_\odot$, the difference vanishes.
- Secondly, for the cloud-ensemble models, we separated the distribution of gas density into two cases: (1) $s = 0$ and (2) $s = -2$, where the ionization parameter $U \propto r^{-2}$ and $U \propto$ constant, correspondingly.
- In the case of $s = -2$, several lines can be used to probe the difference between BBHs and

SBHs across different gas densities. For example, when the black hole mass is $10^7 M_\odot$, the lines that can be used are: (1) Lyα and CIV ($\log n = 9.5$), (2) Lyα λ1216 Å, CIV λ1549 Å ($\log n = 10.0$), and (3) CIV λ1549 Å, Hα λ6562 Å, and Hβ λ4861 Å. Additionally, the simulated EWs become too high when the black hole mass increases to $10^9 M_\odot$, indicating that we may need to exclude these parameter choices at a higher mass of black holes.

- In the case of $s = 0$, the lines that satisfy our goal in the case of a black hole mass of $10^7 M_\odot$ are SiIV λ1400 Å and CIV λ1549 Å ($\log n = 10.5, 11.0$). However, when the black hole mass increases to $10^9 M_\odot$, these lines show no difference in EWs between BBHs and SBHs.
- Moreover, by comparing these simulated EWs with the observed EWs in the SDSS DR7 Quasar Catalog, we found that some simulated EWs fall within the range of the observed EWs. Most interestingly, for CIV in the case of a black hole mass of $10^7 M_\odot$, $s = -2$, and $\log n = 10.5$, only the SBH EW falls inside the range of the observed range while the BBH EW falls outside and becomes an outlier. It is this outlier behavior of BBHs that we can use to probe the difference between BBHs and SBHs in the observational dataset.

The results produced in our project suggest that line ratio diagnostic diagrams may not help distinguish between BBHs and SBHs, but this needs to be investigated further with cloud-ensemble models and comparison with observed values. Using EWs appears to be more promising, but it depends on the models. Therefore, stronger constraints on SBH models are needed.

5.2 Future Work

Based on the work completed in this project, we plan to extend our research with several goals: (1) varying the element abundance in clouds to explore its effect on emission-line strengths within the BLR, (2) incorporating temporal effects into BELMAC, and (3) applying our current results to available observational datasets, such as the SDSS Quasar Catalog and future LSST AGN spectra, to identify SMBBH candidates.

Firstly, for comprehensiveness, we will vary the cloud's element abundance to explore its impact on line strengths.

Secondly, as a mapping code for broad emission lines, BELMAC currently takes a single AGN SED and produces responses for broad emission lines, particularly line luminosity. The code cannot currently process a group of SEDs spanning different periods of SMBBHs. Therefore, we aim to extend BELMAC's capabilities to simulate responses of broad emission lines with time-dependent SEDs.

Thirdly, we will use PYQSOFIT, a fitting code for quasar spectra, to extract spectral information from the observational datasets mentioned above. Although the fitting process sounds straightforward, the SDSS DR16 Quasar Catalog includes about one million quasars, making manual fitting impractical. Thus, we need to develop an algorithm to automatically extract the necessary spectral information, such as line flux and equivalent width, from these spectra.

After extracting the required spectral information, we will compare this observational data with our project's results to test and refine our BBH identification method.

Once BELMAC's extension is complete, we will simulate the responses of broad emission lines using time-dependent BH SEDs. Additionally, we will obtain more BBH SEDs from our CCRG GRMHD group, which evolved these SEDs based on a grid of parameters: mass ratio, spin parameter, and initial separations. By inputting these SEDs into BELMAC, we aim to simulate more line responses that can differentiate BBHs from SBHs and can be used in observational datasets.

Lastly, with both simulation and observational data in hand, we will compare them to refine our diagnostic methods for distinguishing BBHs from SBHs.

All in all, the goal is still to distinguish between the binary and single supermassive black holes using the broad emission lines. Therefore, we will keep searching for the outlier behaviors in these broad emission lines lying in the equivalent width of the binary black holes. After the binary candidates have been identified with this outlier behavior, it is possible to further investigate these objects with other methods: (1) direct imaging with Very Long Baseline Interferometry (VLBI), (2) PTAs and LISA to detect the gravitational waves emitted from these objects, and (3) periodicities and gravitational self-lensing of light curves of these objects.

-

Appendices

- -

Appendix A

Additional BPT Diagrams

We included additional BPT diagrams in this section.

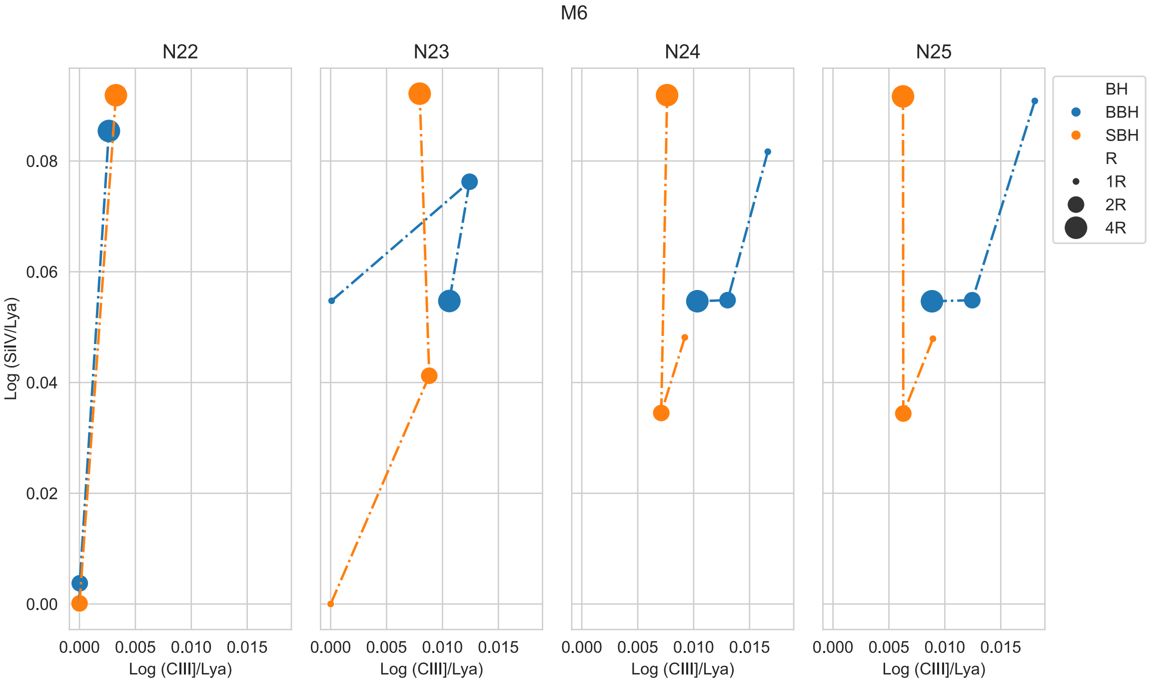

Figure A.1: A BLR BPT diagram for a black hole mass of $10^6 M_\odot$. The x-axis represents the line ratio between SiIV $\lambda1400$ Å and Lyα $\lambda1216$ Å. the y-axis represents the line ratio between CIII] $\lambda1909$ Å and Lyα $\lambda1216$ Å. The BH types are represented in two colors: SBH (orange) and BBH (blue). From left to right, the column density increases by a factor of 10, from 10^{22} cm^{-3} to 10^{25} cm^{-3}.

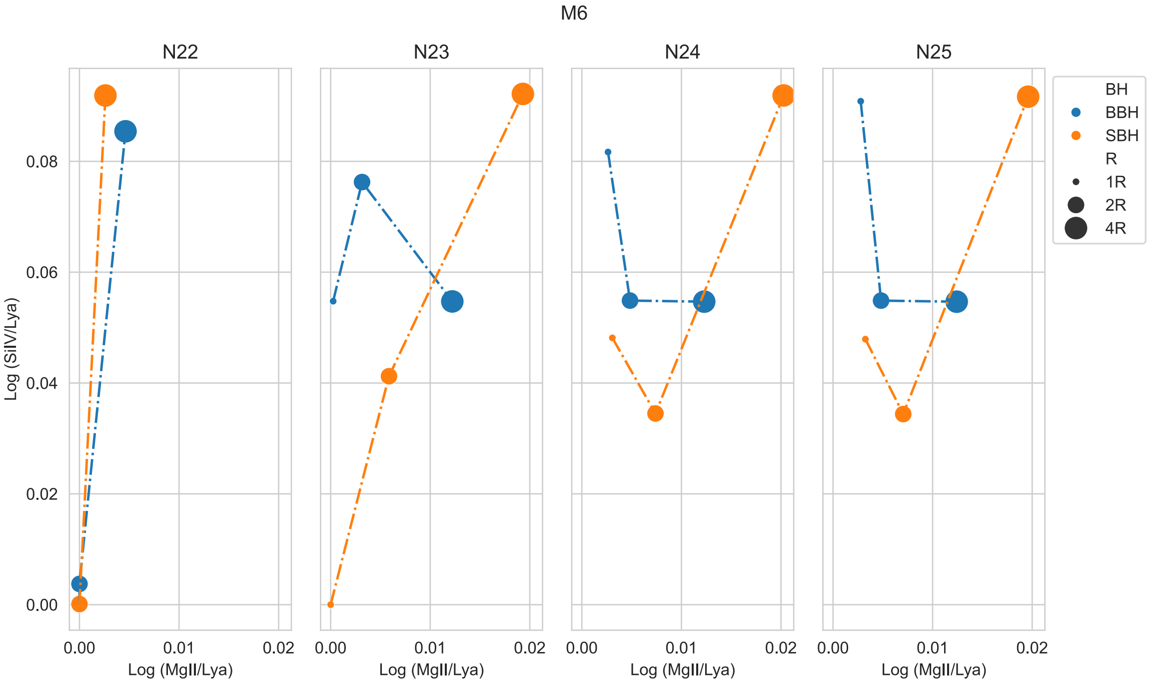

Figure A.2: A BLR BPT diagram for a black hole mass of $10^6 M_\odot$. The x-axis represents the line ratio between SiIV λ1400 Å and Lyα λ1216 Å. the y-axis represents the line ratio between MgII λ2798 Å and Lyα λ1216 Å. The BH types are represented in two colors: SBH (orange) and BBH (blue). From left to right, the column density increases by a factor of 10, from 10^{22} cm^{-3} to 10^{25} cm^{-3}.

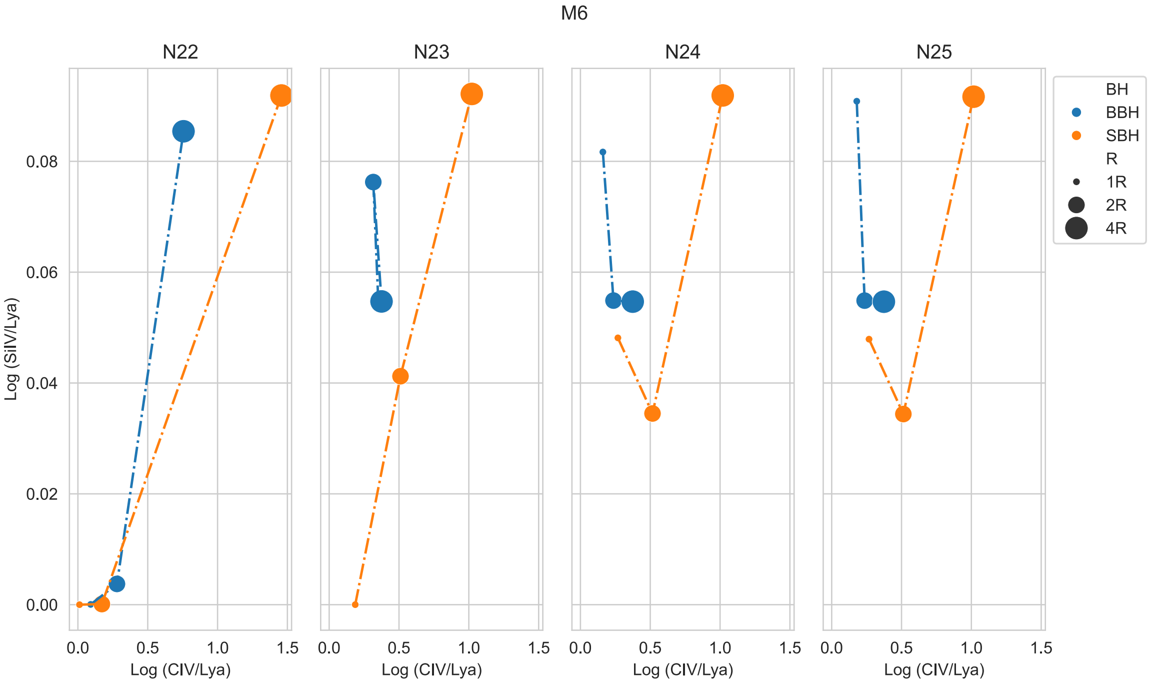

Figure A.3: A BLR BPT diagram for a black hole mass of $10^6 M_\odot$. The x-axis represents the line ratio between SiIV λ1400 Å and Lyα λ1216 Å. the y-axis represents the line ratio between CIV λ1549 Å and Lyα λ1216 Å. The BH types are represented in two colors: SBH (orange) and BBH (blue). From left to right, the column density increases by a factor of 10, from 10^{22} cm^{-3} to 10^{25} cm^{-3}.

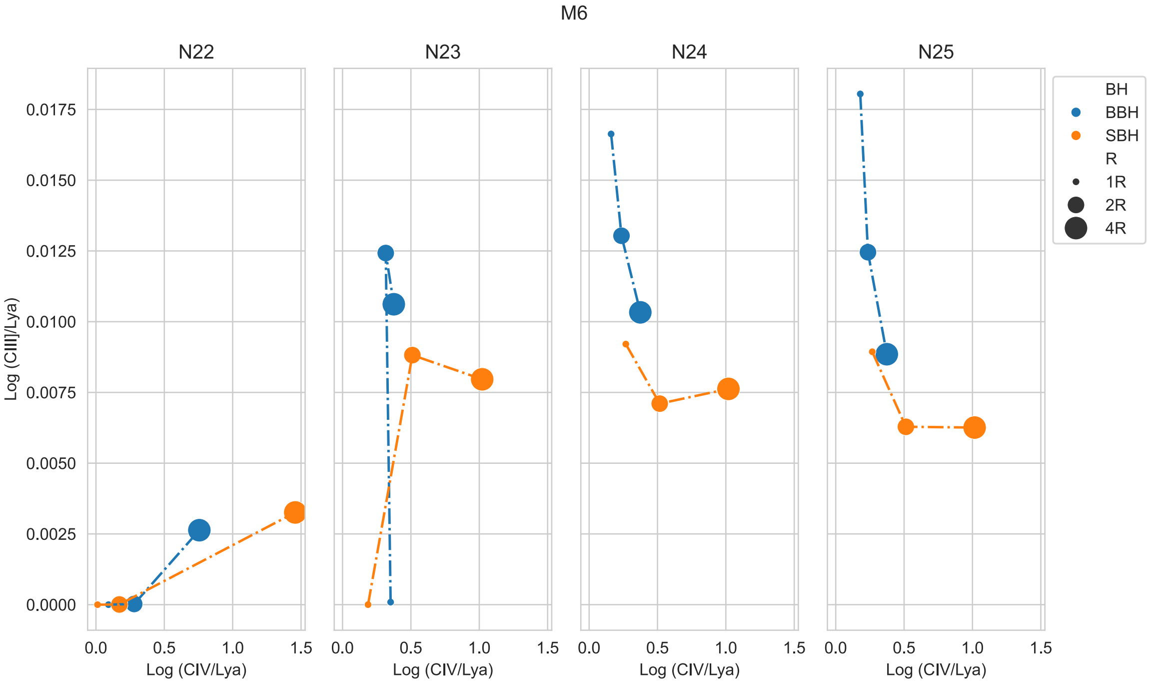

Figure A.4: A BLR BPT diagram for a black hole mass of $10^6 M_\odot$. The x-axis represents the line ratio between CIII] λ1909 Å and Lyα λ1216 Å. the y-axis represents the line ratio between CIV λ1549 Å and Lyα λ1216 Å. The BH types are represented in two colors: SBH (orange) and BBH (blue). From left to right, the column density increases by a factor of 10, from 10^{22} cm^{-3} to 10^{25} cm^{-3}.

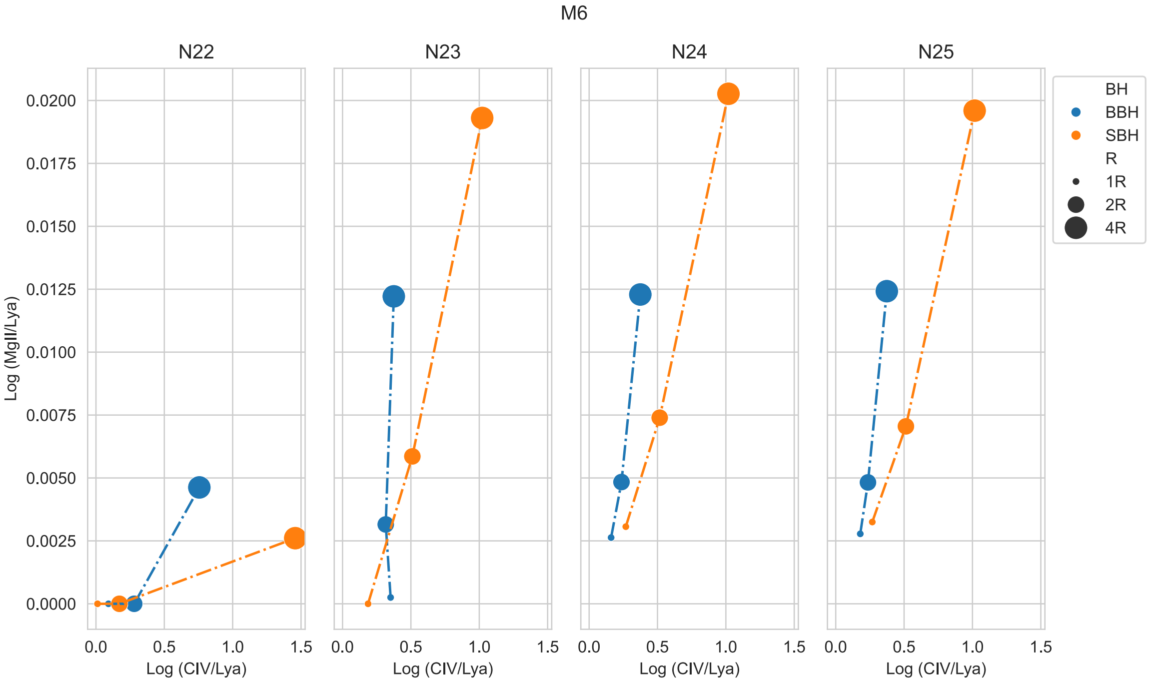

Figure A.5: A BLR BPT diagram for a black hole mass of $10^6 M_\odot$. The x-axis represents the line ratio between MgII λ2798 Å and Lyα λ1216 Å. the y-axis represents the line ratio between CIV λ1549 Å and Lyα λ1216 Å. The BH types are represented in two colors: SBH (orange) and BBH (blue). From left to right, the column density increases by a factor of 10, from 10^{22} cm^{-3} to 10^{25} cm^{-3}.

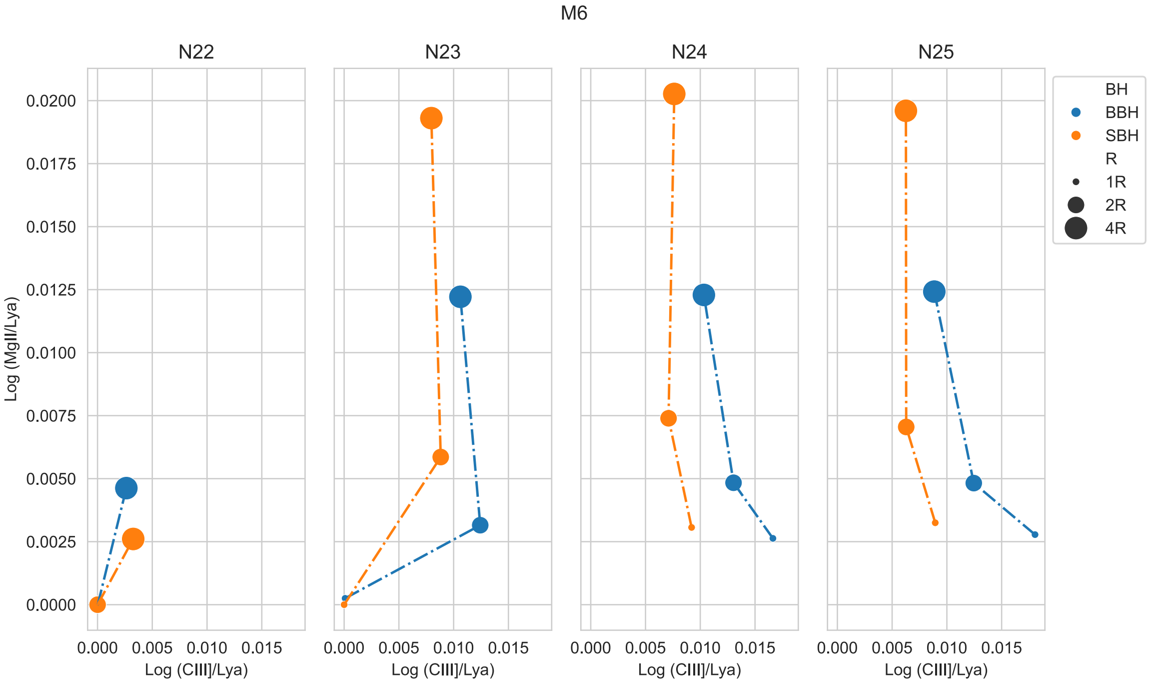

Figure A.6: A BLR BPT diagram for a black hole mass of $10^6 M_\odot$. The x-axis represents the line ratio between MgII λ2798 Å and Lyα λ1216 Å. the y-axis represents the line ratio between CIII] λ1909 Å and Lyα λ1216 Å. The BH types are represented in two colors: SBH (orange) and BBH (blue). From left to right, the column density increases by a factor of 10, from 10^{22} cm^{-3} to 10^{25} cm^{-3}.

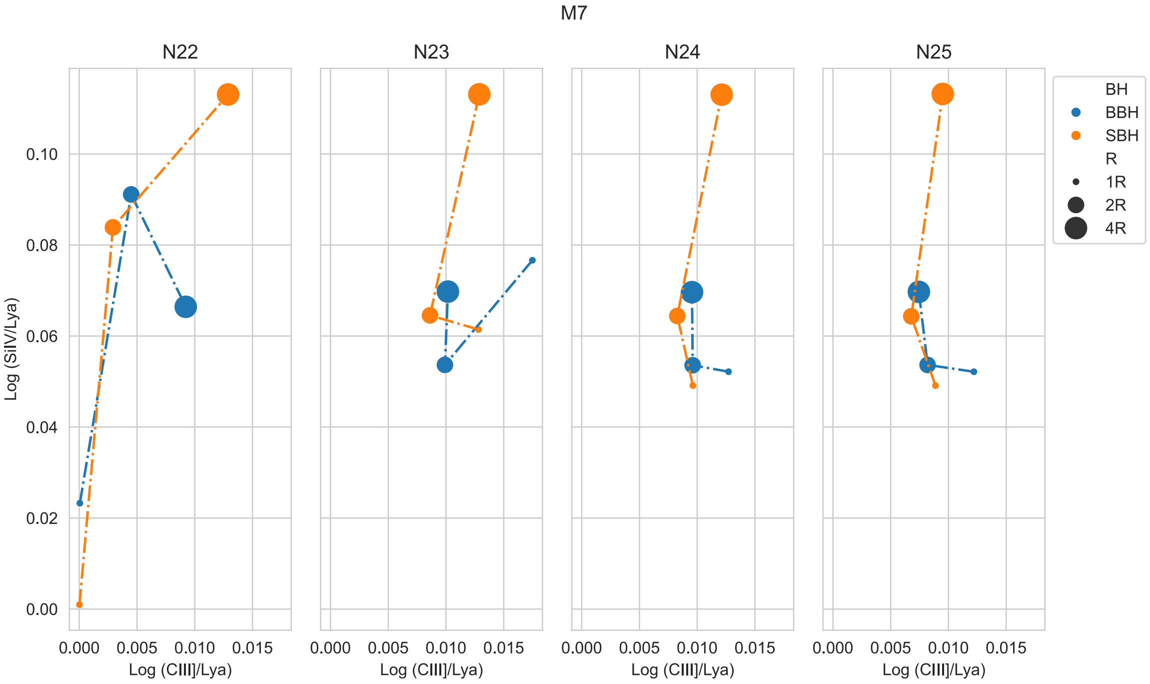

Figure A.7: A BLR BPT diagram for a black hole mass of $10^7 M_\odot$. The x-axis represents the line ratio between SiIV $\lambda1400$ Å and Lyα $\lambda1216$ Å. the y-axis represents the line ratio between CIII] $\lambda1909$ Å and Lyα $\lambda1216$ Å. The BH types are represented in two colors: SBH (orange) and BBH (blue). From left to right, the column density increases by a factor of 10, from 10^{22} cm^{-3} to 10^{25} cm^{-3}.

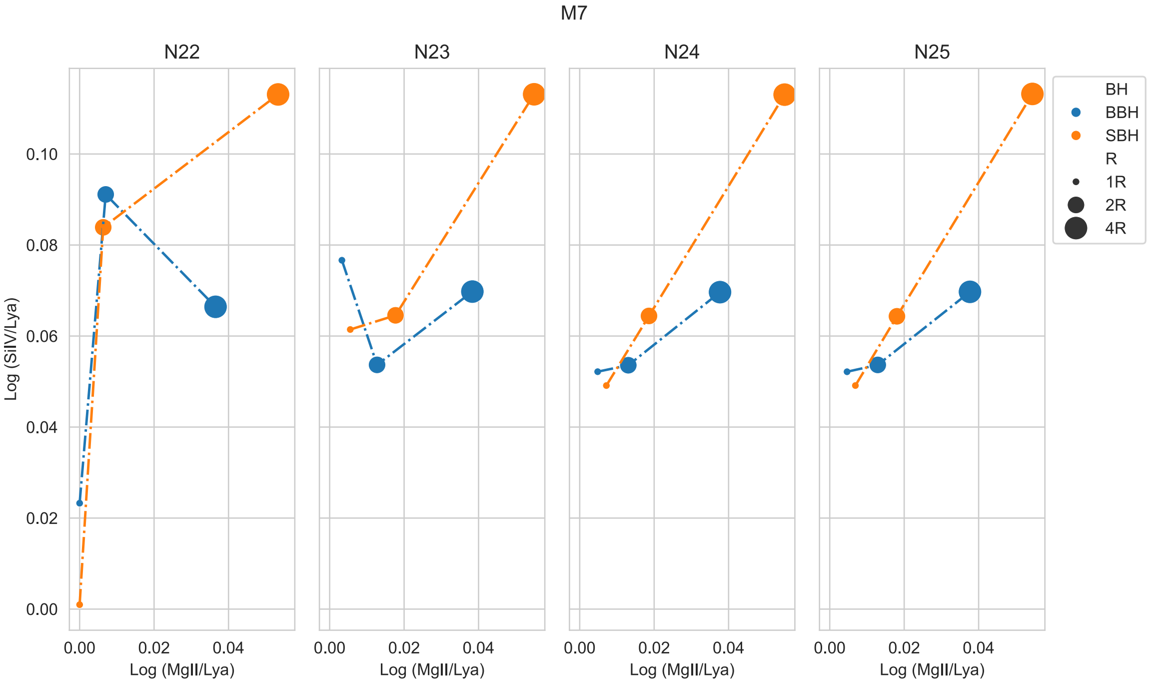

Figure A.8: A BLR BPT diagram for a black hole mass of $10^7 M_\odot$. The x-axis represents the line ratio between SiIV λ1400 Å and Lyα λ1216 Å. the y-axis represents the line ratio between MgII λ2798 Å and Lyα λ1216 Å. The BH types are represented in two colors: SBH (orange) and BBH (blue). From left to right, the column density increases by a factor of 10, from 10^{22} cm^{-3} to 10^{25} cm^{-3}.

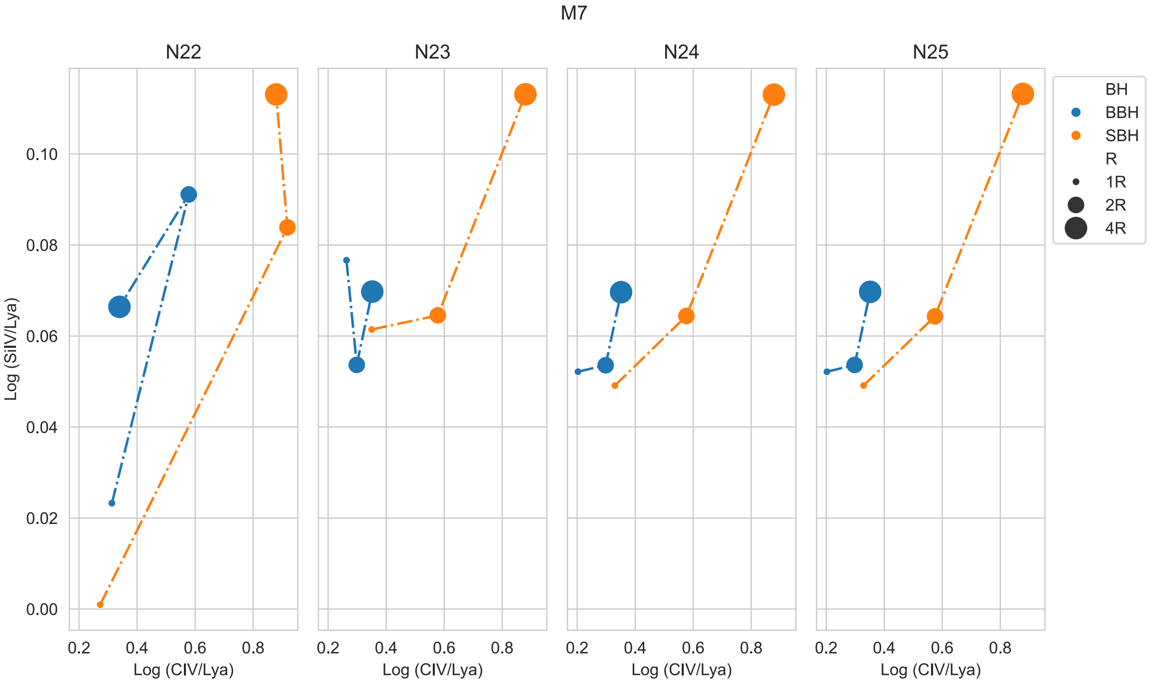

Figure A.9: A BLR BPT diagram for a black hole mass of $10^7 M_\odot$. The x-axis represents the line ratio between SiIV λ1400 Å and Lyα λ1216 Å. the y-axis represents the line ratio between CIV λ1549 Å and Lyα λ1216 Å. The BH types are represented in two colors: SBH (orange) and BBH (blue). From left to right, the column density increases by a factor of 10, from 10^{22} cm^{-3} to 10^{25} cm^{-3}.

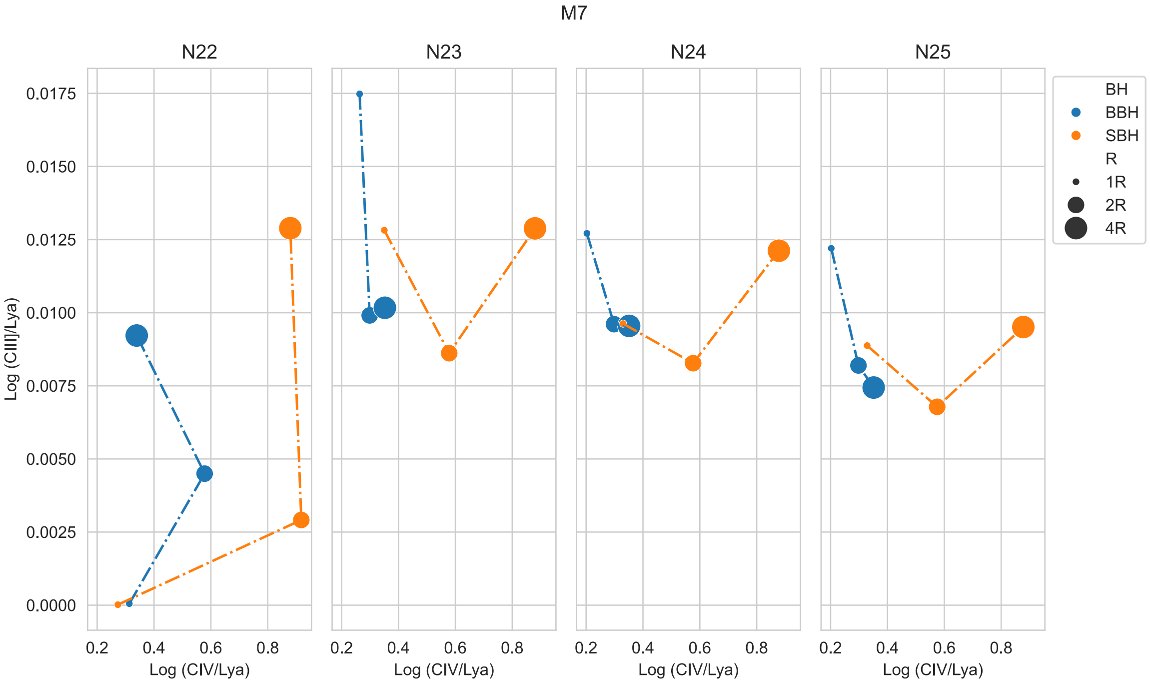

Figure A.10: A BLR BPT diagram for a black hole mass of $10^7 M_\odot$. The x-axis represents the line ratio between CIII] λ1909 Å and Lyα λ1216 Å. the y-axis represents the line ratio between CIV λ1549 Å and Lyα λ1216 Å. The BH types are represented in two colors: SBH (orange) and BBH (blue). From left to right, the column density increases by a factor of 10, from 10^{22} cm^{-3} to 10^{25} cm^{-3}.

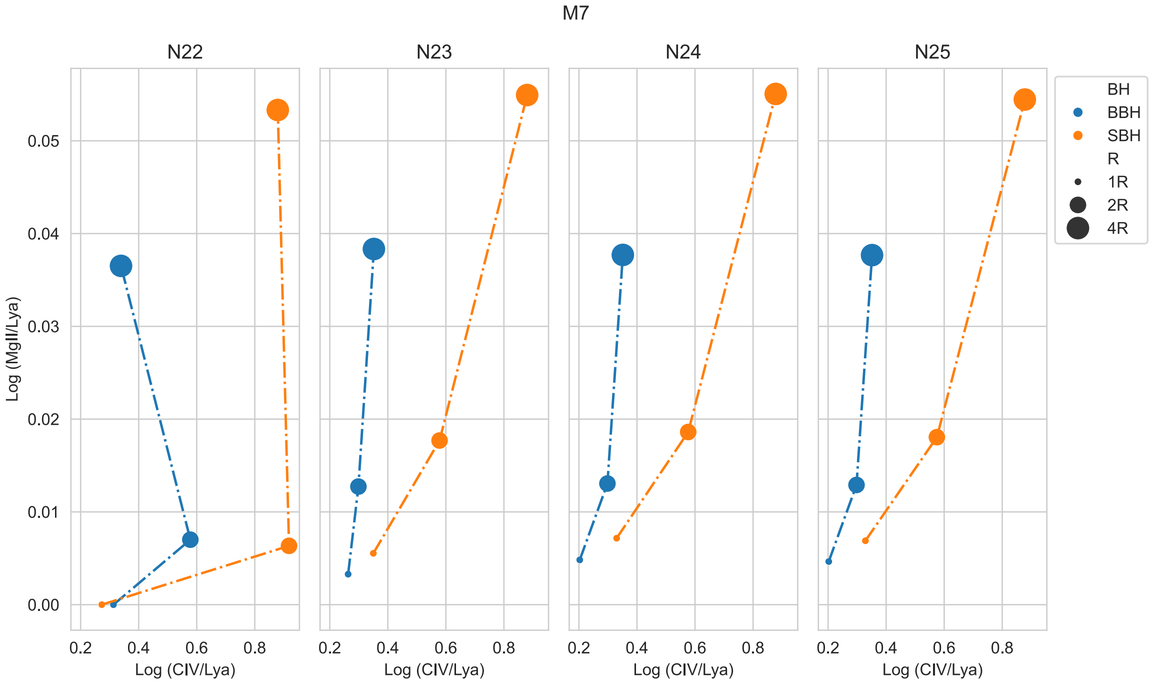

Figure A.11: A BLR BPT diagram for a black hole mass of $10^7 M_\odot$. The x-axis represents the line ratio between MgII λ2798 Å and Lyα λ1216 Å. the y-axis represents the line ratio between CIV λ1549 Å and Lyα λ1216 Å. The BH types are represented in two colors: SBH (orange) and BBH (blue). From left to right, the column density increases by a factor of 10, from 10^{22} cm^{-3} to 10^{25} cm^{-3}.

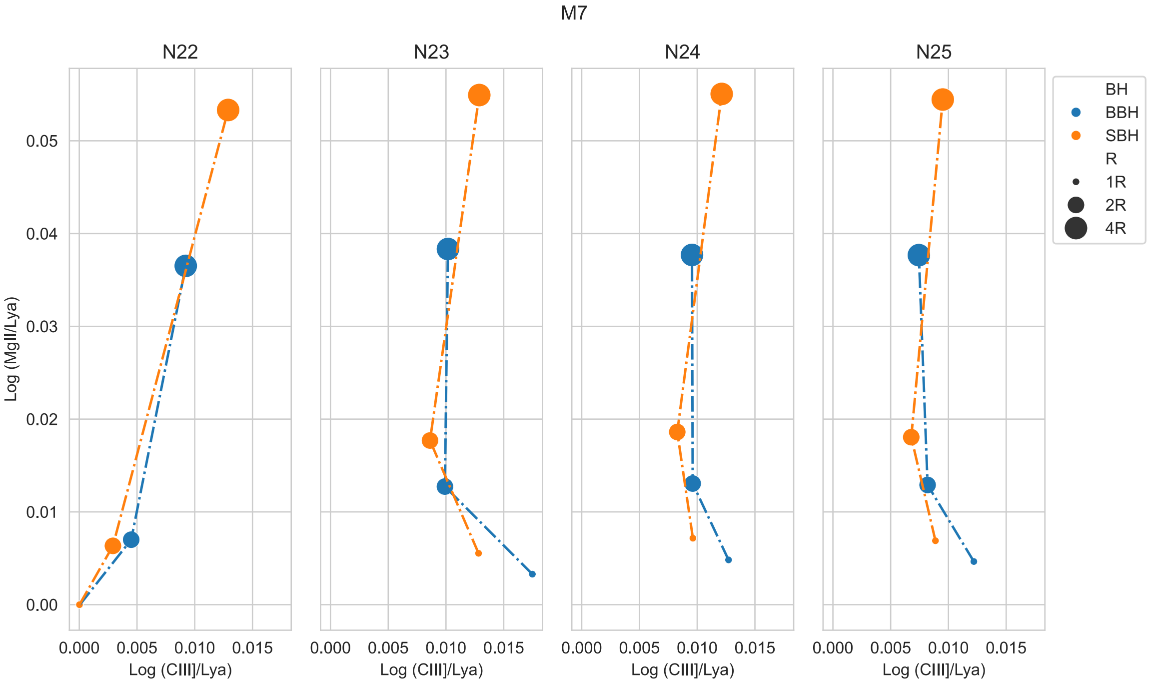

Figure A.12: A BLR BPT diagram for a black hole mass of $10^7 M_\odot$. The x-axis represents the line ratio between MgII λ2798 Å and Lyα λ1216 Å. the y-axis represents the line ratio between CIII] λ1909 Å and Lyα λ1216 Å. The BH types are represented in two colors: SBH (orange) and BBH (blue). From left to right, the column density increases by a factor of 10, from 10^{22} cm^{-3} to 10^{25} cm^{-3}.

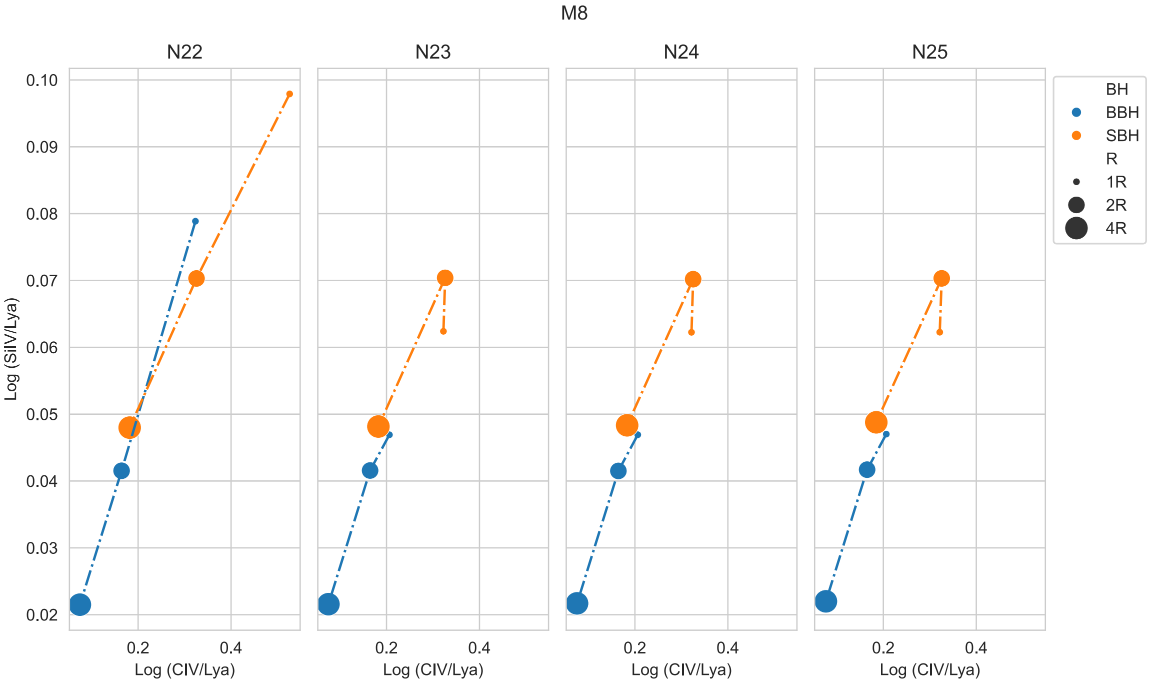

Figure A.13: A BLR BPT diagram for a black hole mass of $10^8 M_\odot$. The x-axis represents the line ratio between SiIV λ1400 Å and Lyα λ1216 Å. the y-axis represents the line ratio between CIV λ1549 Å and Lyα λ1216 Å. The BH types are represented in two colors: SBH (orange) and BBH (blue). From left to right, the column density increases by a factor of 10, from 10^{22} cm^{-3} to 10^{25} cm^{-3}.

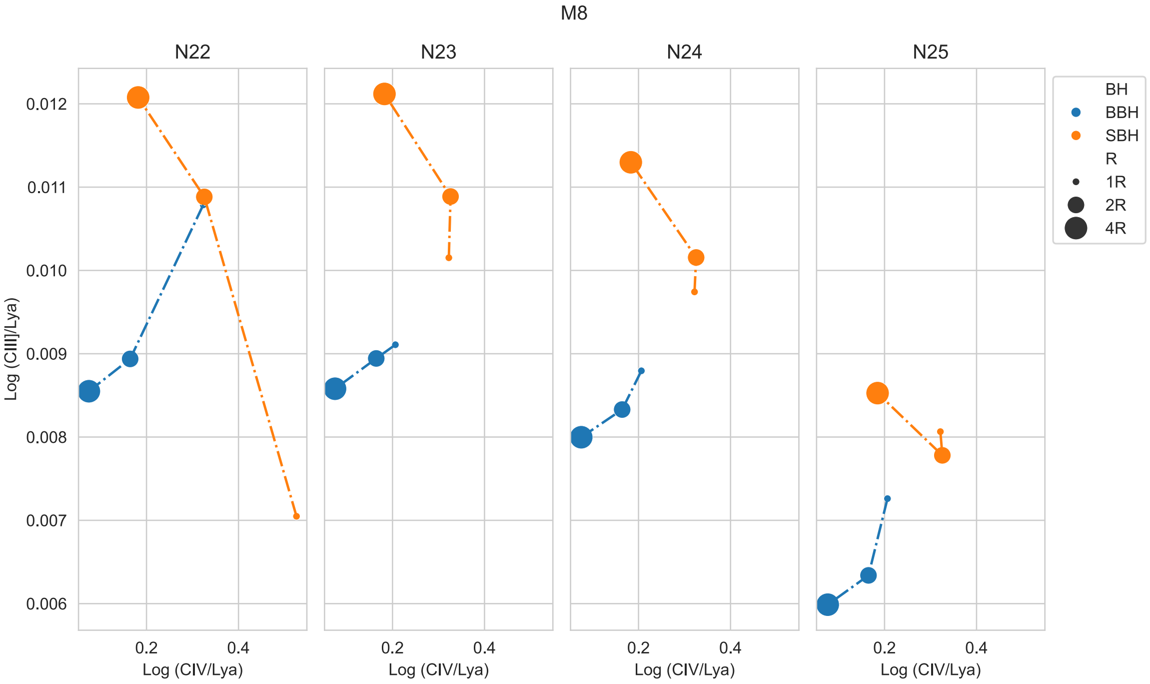

Figure A.14: A BLR BPT diagram for a black hole mass of $10^8 M_\odot$. The x-axis represents the line ratio between CIII] λ1909 Å and Lyα λ1216 Å. the y-axis represents the line ratio between CIV λ1549 Å and Lyα λ1216 Å. The BH types are represented in two colors: SBH (orange) and BBH (blue). From left to right, the column density increases by a factor of 10, from 10^{22} cm^{-3} to 10^{25} cm^{-3}.

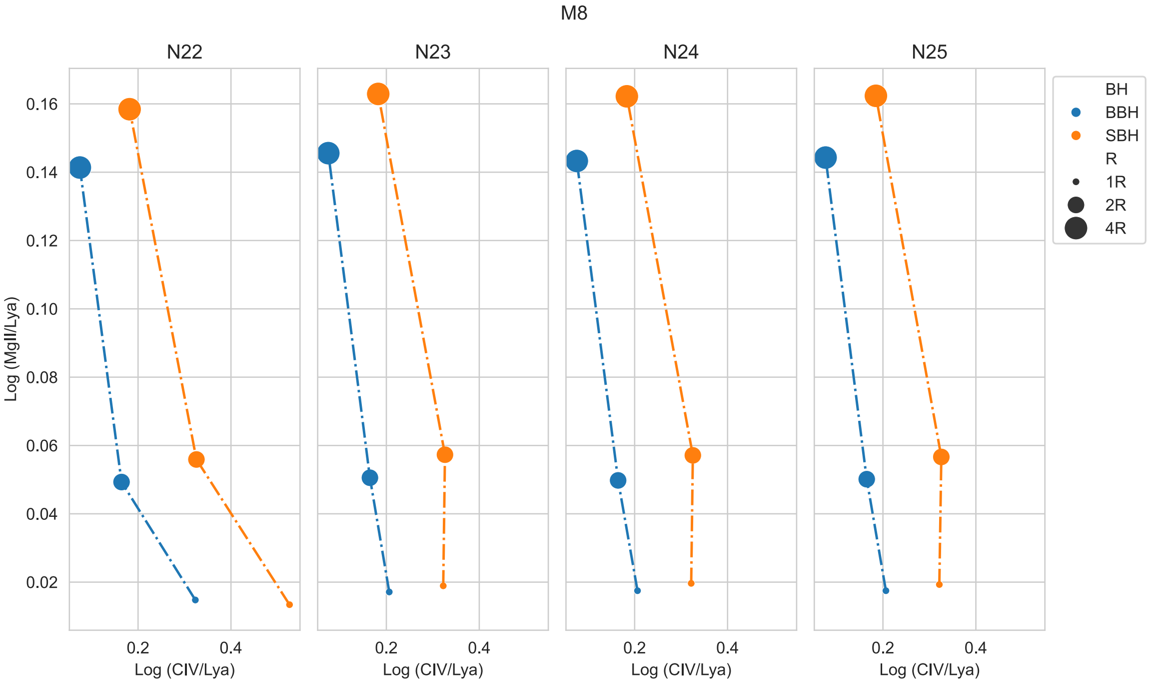

Figure A.15: A BLR BPT diagram for a black hole mass of $10^8 M_\odot$. The x-axis represents the line ratio between MgII λ2798 Å and Lyα λ1216 Å. the y-axis represents the line ratio between CIV λ1549 Å and Lyα λ1216 Å. The BH types are represented in two colors: SBH (orange) and BBH (blue). From left to right, the column density increases by a factor of 10, from 10^{22} cm^{-3} to 10^{25} cm^{-3}.

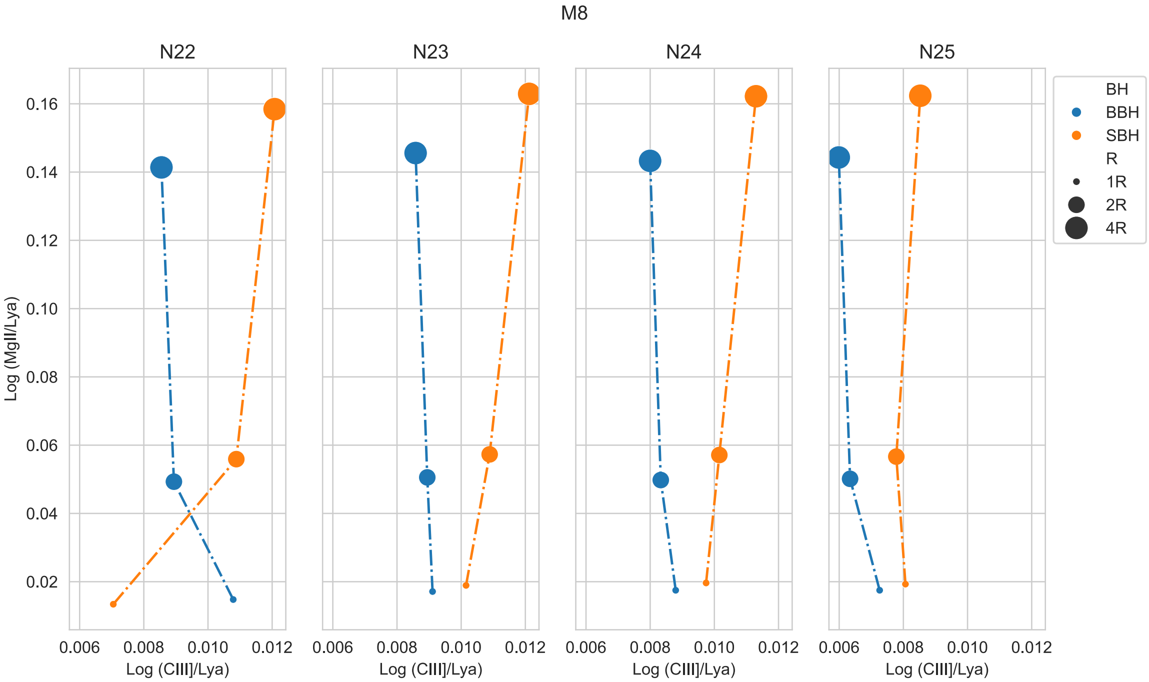

Figure A.16: A BLR BPT diagram for a black hole mass of $10^8 M_\odot$. The x-axis represents the line ratio between MgII λ2798 Å and Lyα λ1216 Å. the y-axis represents the line ratio between CIII] λ1909 Å and Lyα λ1216 Å. The BH types are represented in two colors: SBH (orange) and BBH (blue). From left to right, the column density increases by a factor of 10, from 10^{22} cm^{-3} to 10^{25} cm^{-3}.

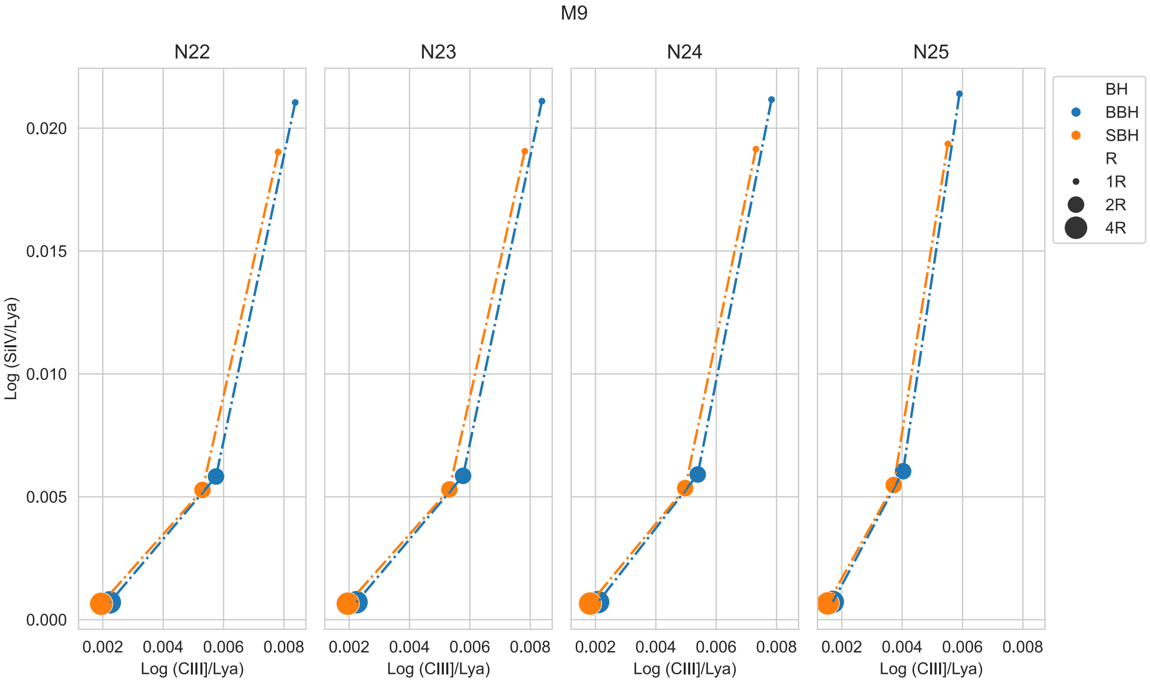

Figure A.17: A BLR BPT diagram for a black hole mass of $10^9 M_\odot$. The x-axis represents the line ratio between SiIV λ1400 Å and Lyα λ1216 Å. the y-axis represents the line ratio between CIII] λ1909 Å and Lyα λ1216 Å. The BH types are represented in two colors: SBH (orange) and BBH (blue). From left to right, the column density increases by a factor of 10, from 10^{22} cm^{-3} to 10^{25} cm^{-3}.

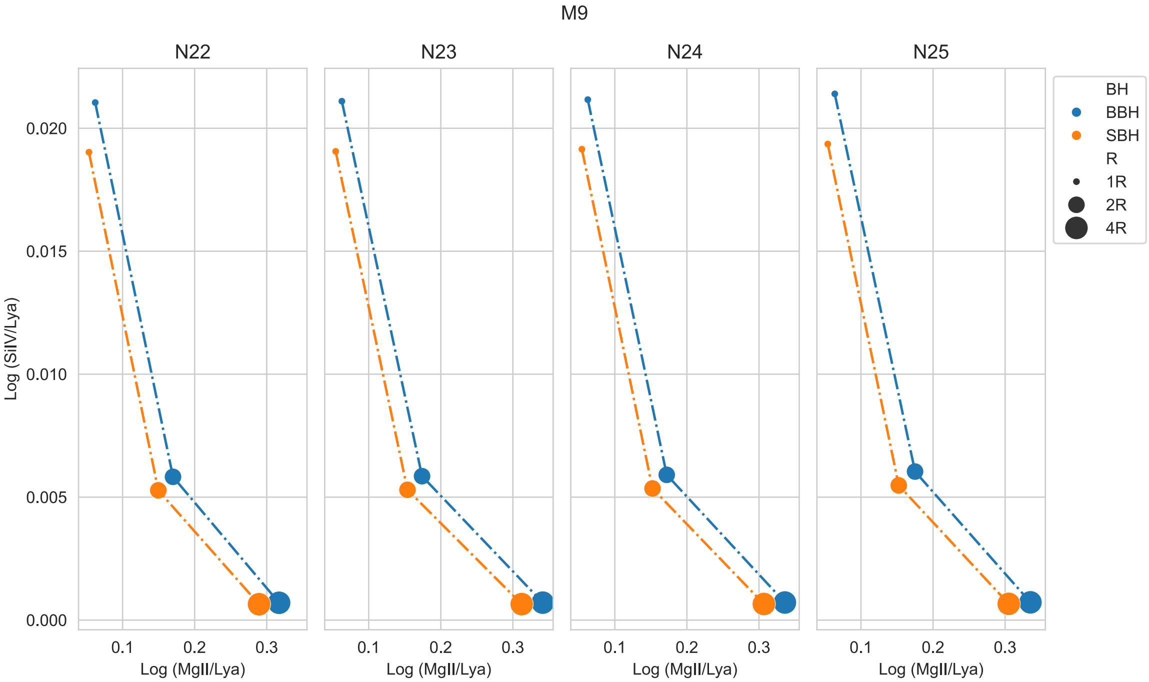

Figure A.18: A BLR BPT diagram for a black hole mass of $10^9 M_\odot$. The x-axis represents the line ratio between SiIV λ1400 Å and Lyα λ1216 Å. the y-axis represents the line ratio between MgII λ2798 Å and Lyα λ1216 Å. The BH types are represented in two colors: SBH (orange) and BBH (blue). From left to right, the column density increases by a factor of 10, from 10^{22} cm^{-3} to 10^{25} cm^{-3}.

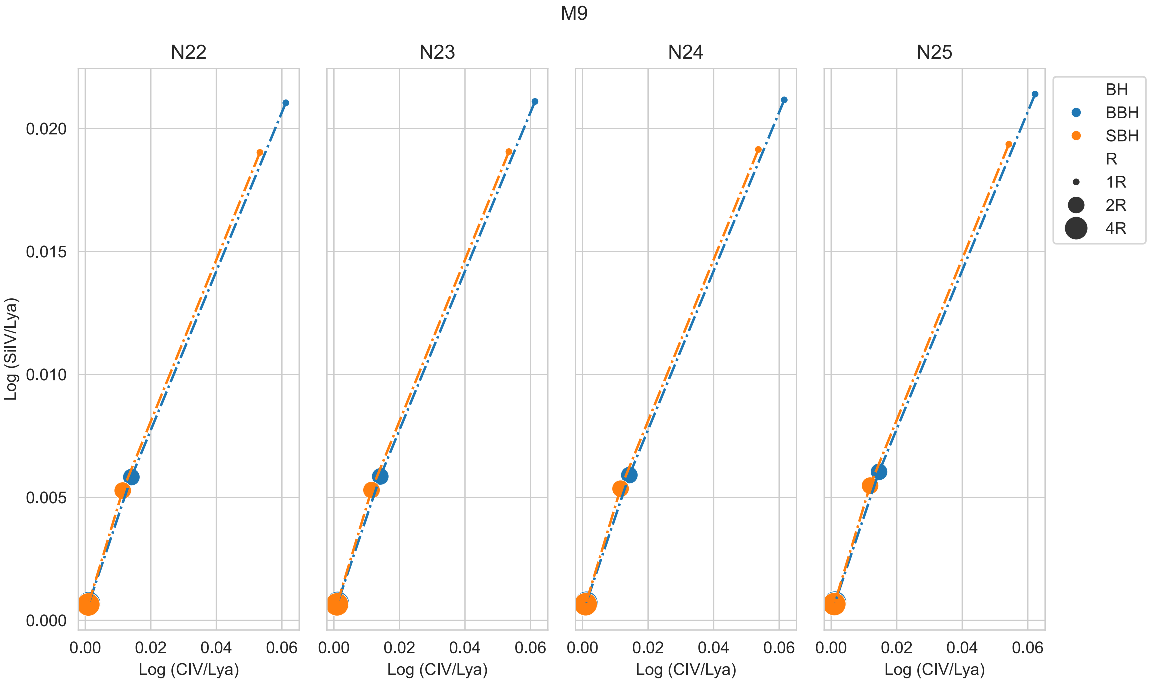

Figure A.19: A BLR BPT diagram for a black hole mass of $10^9 M_\odot$. The x-axis represents the line ratio between SiIV λ1400 Å and Lyα λ1216 Å. the y-axis represents the line ratio between CIV λ1549 Å and Lyα λ1216 Å. The BH types are represented in two colors: SBH (orange) and BBH (blue). From left to right, the column density increases by a factor of 10, from 10^{22} cm^{-3} to 10^{25} cm^{-3}.

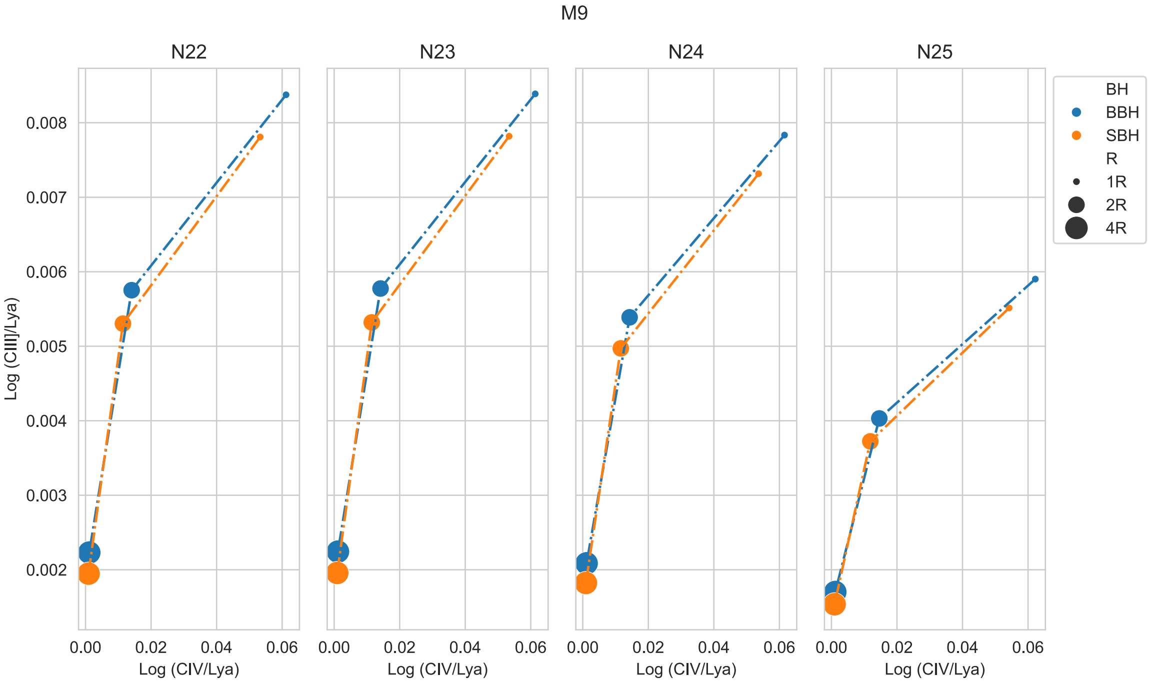

Figure A.20: A BLR BPT diagram for a black hole mass of $10^9 M_\odot$. The x-axis represents the line ratio between CIII] λ1909 Å and Lyα λ1216 Å. the y-axis represents the line ratio between CIV λ1549 Å and Lyα λ1216 Å. The BH types are represented in two colors: SBH (orange) and BBH (blue). From left to right, the column density increases by a factor of 10, from 10^{22} cm^{-3} to 10^{25} cm^{-3}.

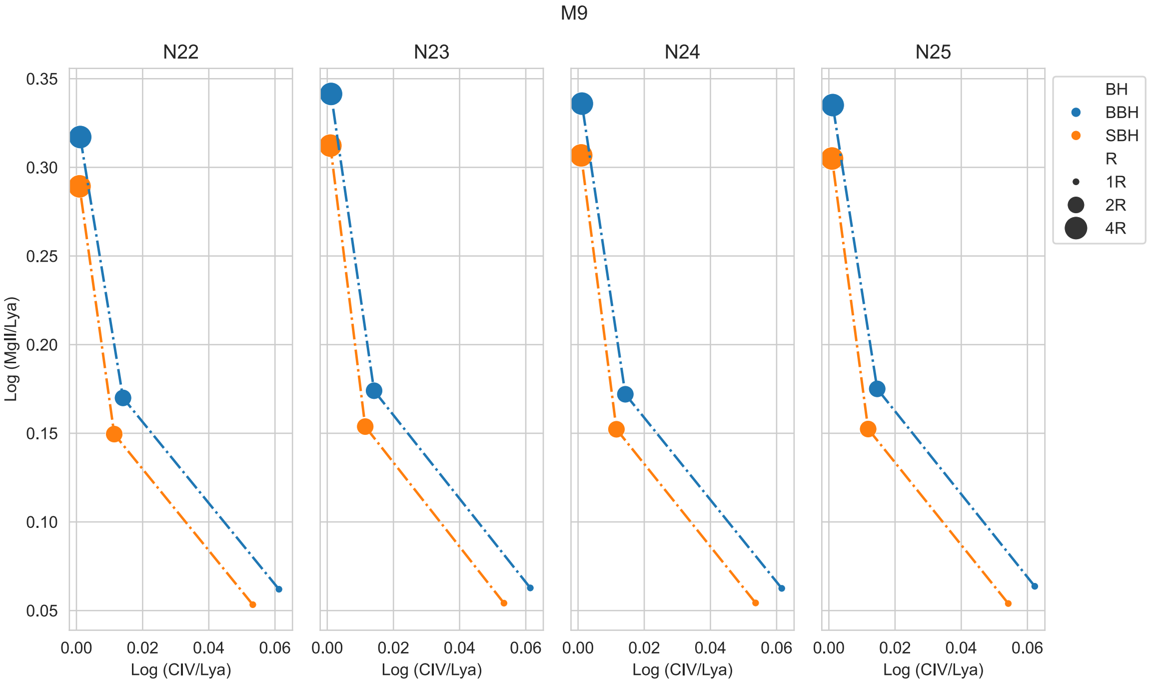

Figure A.21: A BLR BPT diagram for a black hole mass of $10^9 M_\odot$. The x-axis represents the line ratio between MgII $\lambda2798$ Å and Lyα $\lambda1216$ Å. the y-axis represents the line ratio between CIV $\lambda1549$ Å and Lyα $\lambda1216$ Å. The BH types are represented in two colors: SBH (orange) and BBH (blue). From left to right, the column density increases by a factor of 10, from 10^{22} cm^{-3} to 10^{25} cm^{-3}.

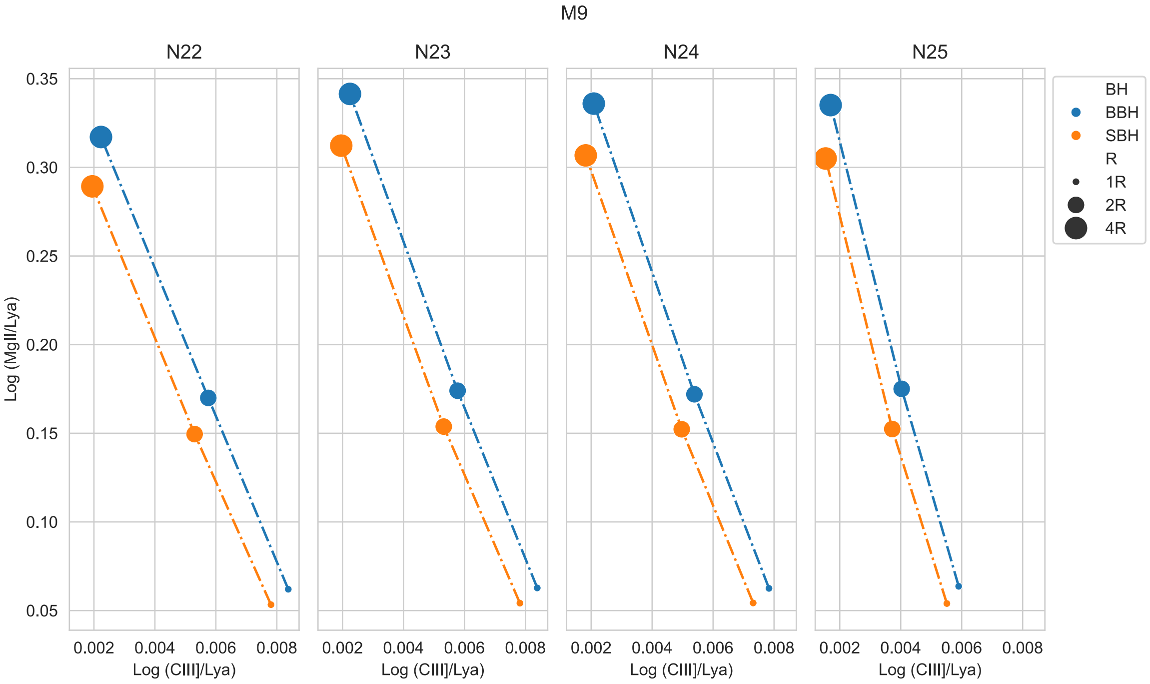

Figure A.22: A BLR BPT diagram for a black hole mass of $10^9 M_\odot$. The x-axis represents the line ratio between MgII λ2798 Å and Lyα λ1216 Å. the y-axis represents the line ratio between CIII] λ1909 Å and Lyα λ1216 Å. The BH types are represented in two colors: SBH (orange) and BBH (blue). From left to right, the column density increases by a factor of 10, from 10^{22} cm^{-3} to 10^{25} cm^{-3}.

Appendix B

Additional EW Diagrams

In this appendix, we included the additional EW diagrams for single-cloud and cloud-ensemble models.

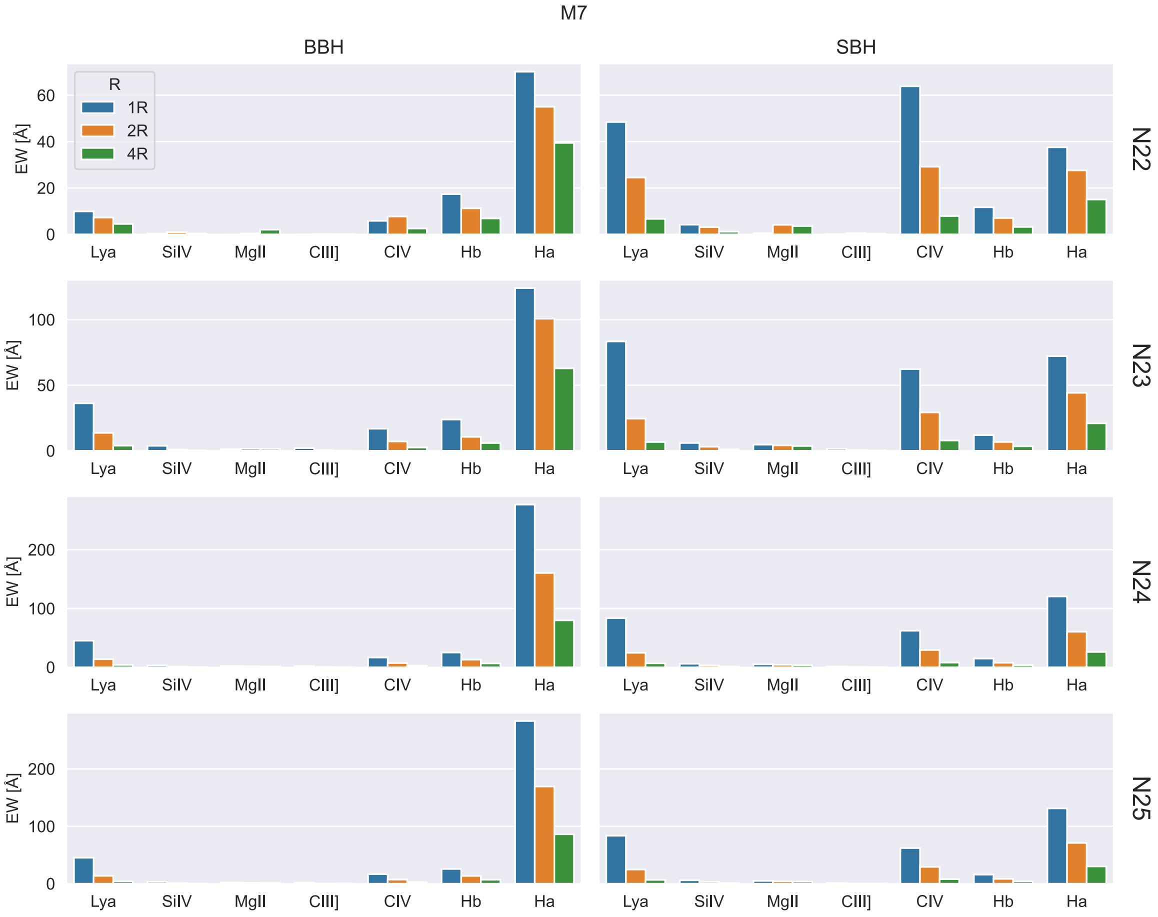

Figure B.1: Equivalent width for M7. The top panel is BBH EW and the bottom one is SBH EW. For each line, there are three radii for EWs: 1R (blue), 2R (orange), and 4R (green). From the left panel to the right, the column density increases by a factor of 10 in the range from 10^{22} cm^{-2} to 10^{25} cm^{-2}.

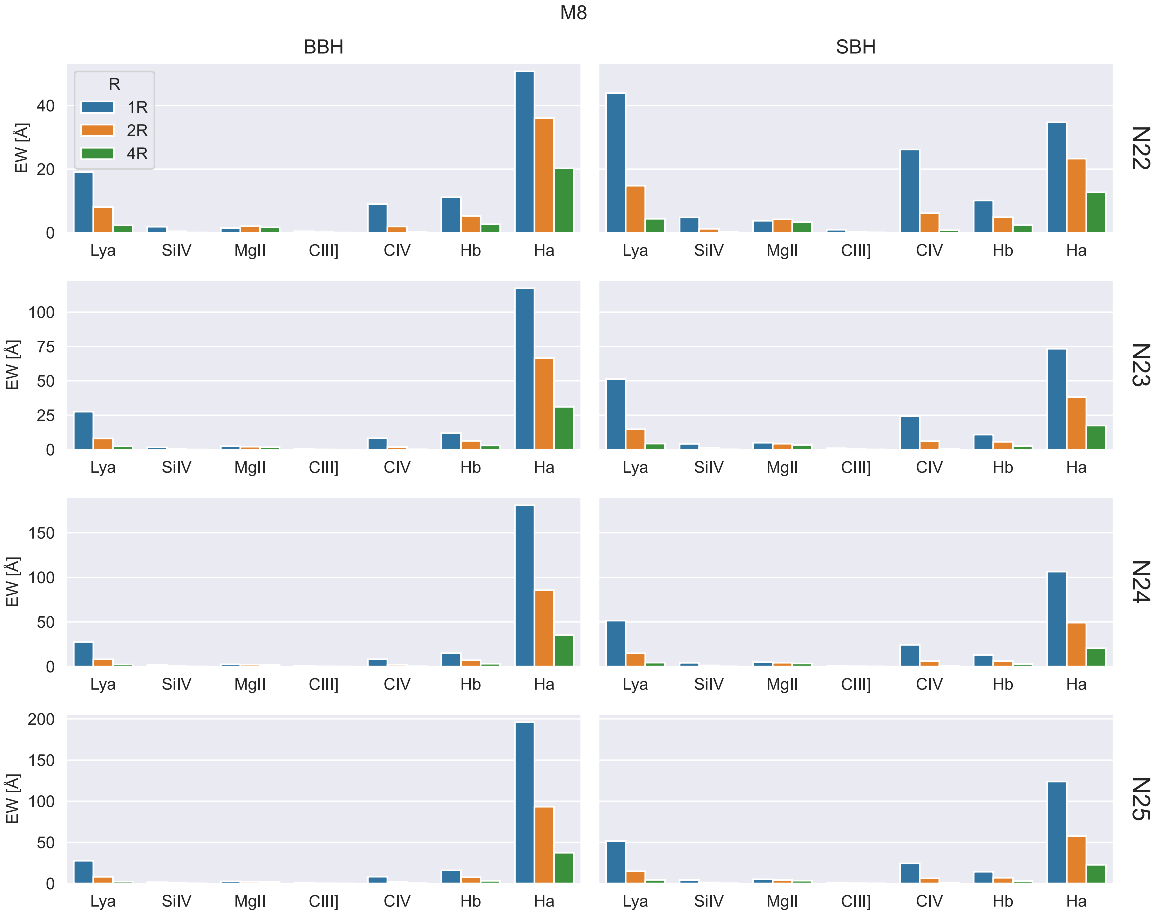

Figure B.2: Equivalent width for M8. The top panel is BBH EW and the bottom one is SBH EW. For each line, there are three radii for EWs: 1R (blue), 2R (orange), and 4R (green). From the left panel to the right, the column density increases by a factor of 10 in the range from 10^{22} cm^{-2} to 10^{25} cm^{-2}.

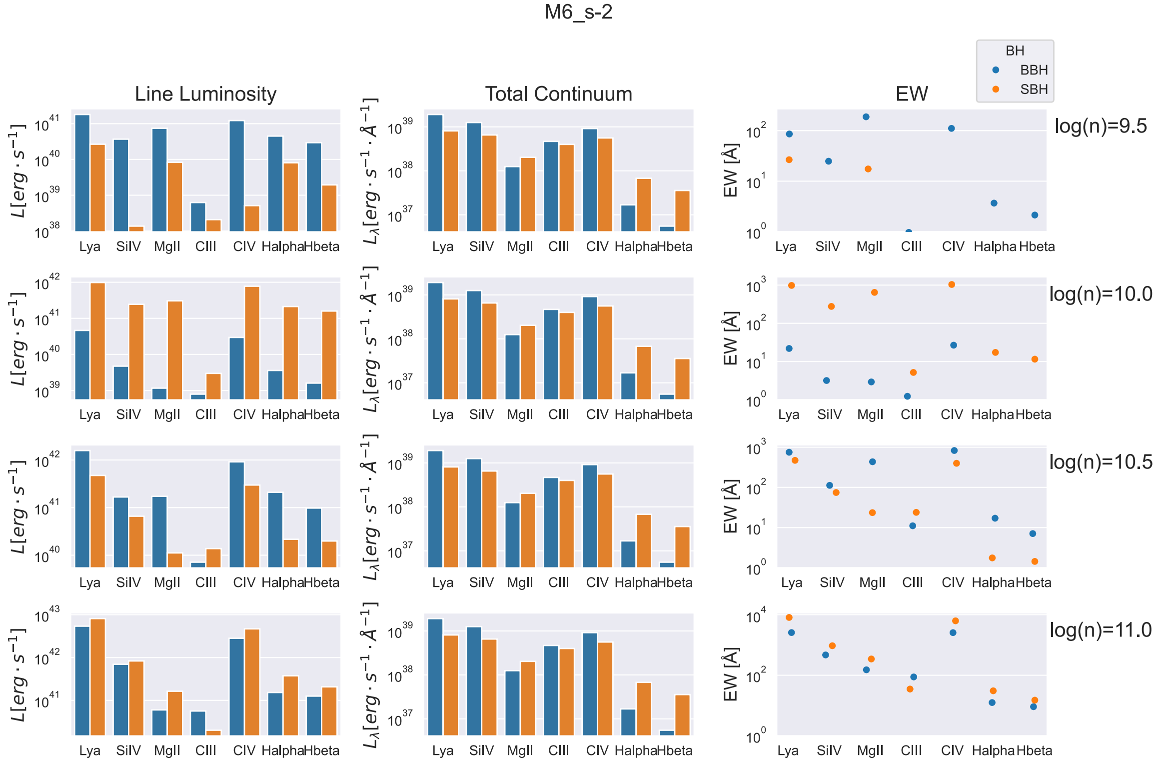

Figure B.3: Cloud ensemble models for the BLR computed with BELMAC. Line luminosity, total continuum including the galaxy continuum, and equivalent widths for a BH mass $10^6 M_\odot$ and $s = -2$. The color scheme here is: BBH denoted in blue and SBH denoted in orange. We have chosen seven emission lines, Si IV λ1400Å, C III] λ1909Å, C IV λ1549Å, Mg II λ2798Å, Lyα λ1216Å, Hα λ6562.80Å, and Hβ λ4861.32Å. There are three columns in the figure: from left to right, the first column shows the line luminosity, the second column shows the specific luminosity of the continuum of the accretion disk, and the third column shows the equivalent width, calculated by dividing the line luminosity by the continuum shown in the previous two columns. The black points with error bars show the mean and standard deviations of the observed EWs of MgII, CIV, Hβ, and Hα calculated using data from the SDSS DR7 Quasar catalog, for black hole masses in the range of $5.5 \leq \log_{10} M_{\rm BH} \leq 6.5$.

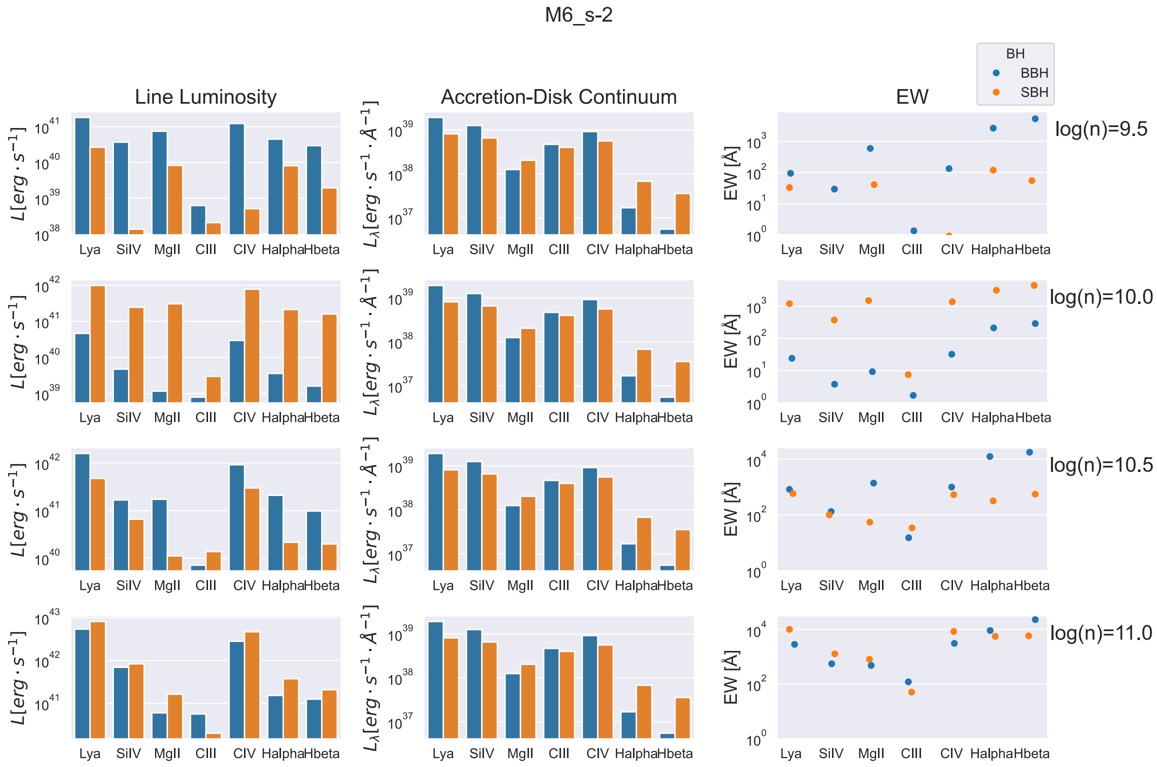

Figure B.4: Cloud ensemble models for the BLR computed with BELMAC. Line luminosity, accretion-disk luminosity, and equivalent widths for a BH mass $10^6 M_\odot$ and $s = -2$. The color scheme here is: BBH denoted in blue and SBH denoted in orange. We have chosen seven emission lines, Si IV λ1400Å, C III] λ1909Å, C IV λ1549Å, Mg II λ2798Å, Lyα λ1216Å, Hα λ6562.80Å, and Hβ λ4861.32Å. There are three columns in the figure: from left to right, the first column shows the line luminosity, the second column shows the specific luminosity of the continuum of the accretion disk, and the third column shows the equivalent width, calculated by dividing the line luminosity by the continuum shown in the previous two columns. The black points with error bars show the mean and standard deviations of the observed EWs of MgII, CIV, Hβ, and Hα calculated using data from the SDSS DR7 Quasar catalog, for black hole masses in the range of $5.5 \leq \log_{10} M_{\rm BH} \leq 6.5$.

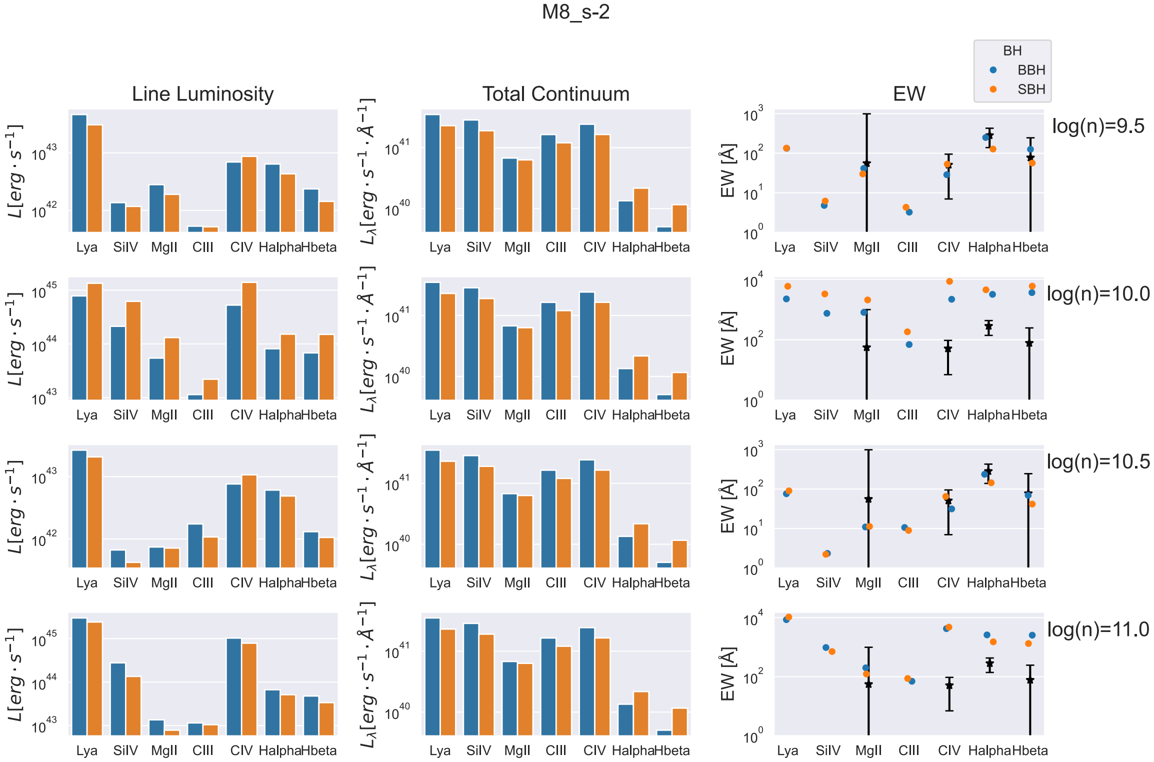

Figure B.5: LCloud ensemble models for the BLR computed with BELMAC. Line luminosity, total continuum including the galaxy continuum, and equivalent widths for a BH mass $10^8 M_\odot$ and $s = -2$. The color scheme here is: BBH denoted in blue and SBH denoted in orange. We have chosen seven emission lines, Si IV λ1400Å, C III] λ1909Å, C IV λ1549Å, Mg II λ2798Å, Lyα λ1216Å, Hα λ6562.80Å, and Hβ λ4861.32Å. There are three columns in the figure: from left to right, the first column shows the line luminosity, the second column shows the specific luminosity of the continuum of the accretion disk, and the third column shows the equivalent width, calculated by dividing the line luminosity by the continuum shown in the previous two columns. The black points with error bars show the mean and standard deviations of the observed EWs of MgII, CIV, Hβ, and Hα calculated using data from the SDSS DR7 Quasar catalog, for black hole masses in the range of $7.5 \leq \log_{10} M_{\rm BH} \leq 8.5$.

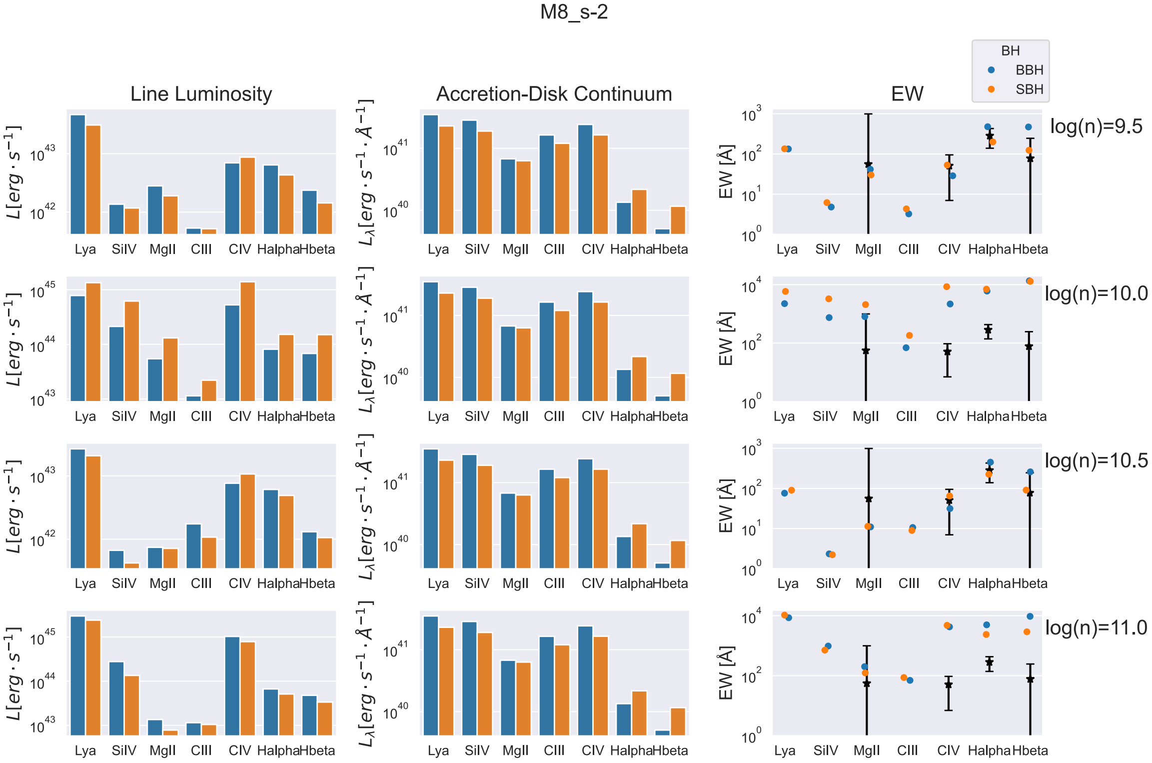

Figure B.6: Cloud ensemble models for the BLR computed with BELMAC. Line luminosity, accretion-disk luminosity, and equivalent widths for a BH mass $10^8 M_\odot$ and $s = -2$. The color scheme here is: BBH denoted in blue and SBH denoted in orange. We have chosen seven emission lines, Si IV λ1400Å, C III] λ1909Å, C IV λ1549Å, Mg II λ2798Å, Lyα λ1216Å, Hα λ6562.80Å, and Hβ λ4861.32Å. There are three columns in the figure: from left to right, the first column shows the line luminosity, the second column shows the specific luminosity of the continuum of the accretion disk, and the third column shows the equivalent width, calculated by dividing the line luminosity by the continuum shown in the previous two columns. The black points with error bars show the mean and standard deviations of the observed EWs of MgII, CIV, Hβ, and Hα calculated using data from the SDSS DR7 Quasar catalog, for black hole masses in the range of $7.5 \leq \log_{10} M_{\rm BH} \leq 8.5$.

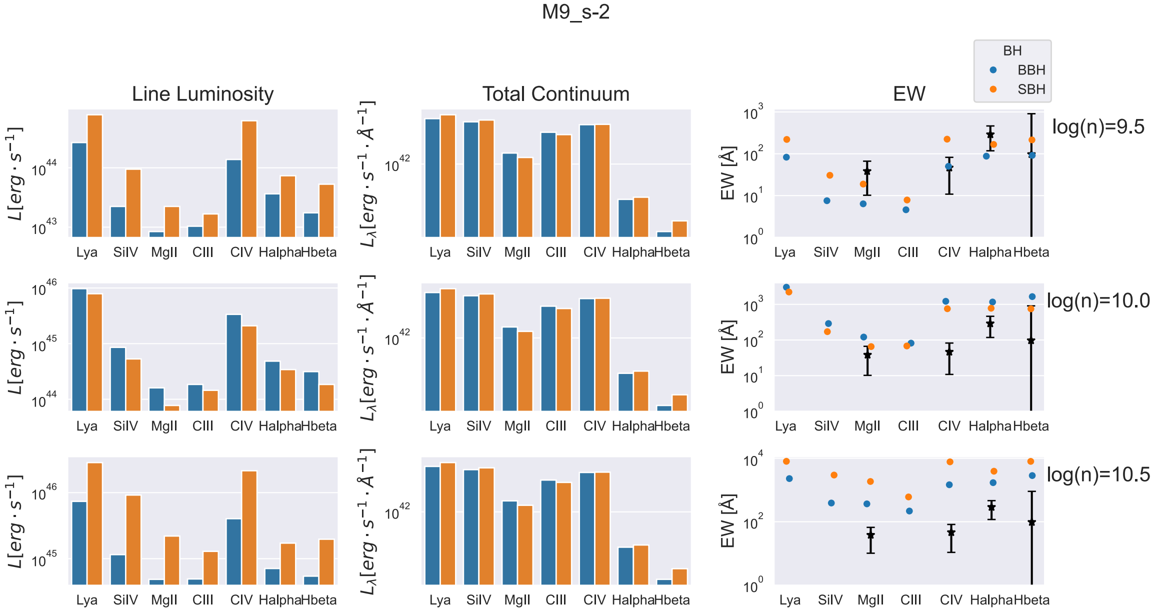

Figure B.7: Cloud ensemble models for the BLR computed with BELMAC. Line luminosity, total continuum including the galaxy continuum, and equivalent widths for a BH mass $10^9 M_\odot$ and $s = -2$. The color scheme here is: BBH denoted in blue and SBH denoted in orange. We have chosen seven emission lines, Si IV λ1400Å, C III] λ1909Å, C IV λ1549Å, Mg II λ2798Å, Lyα λ1216Å, Hα λ6562.80Å, and Hβ λ4861.32Å. There are three columns in the figure: from left to right, the first column shows the line luminosity, the second column shows the specific luminosity of the continuum of the accretion disk, and the third column shows the equivalent width, calculated by dividing the line luminosity by the continuum shown in the previous two columns. The black points with error bars show the mean and standard deviations of the observed EWs of MgII, CIV, Hβ, and Hα calculated using data from the SDSS DR7 Quasar catalog, for black hole masses in the range of $8.5 \leq \log_{10} M_{\rm BH} \leq 9.5$.

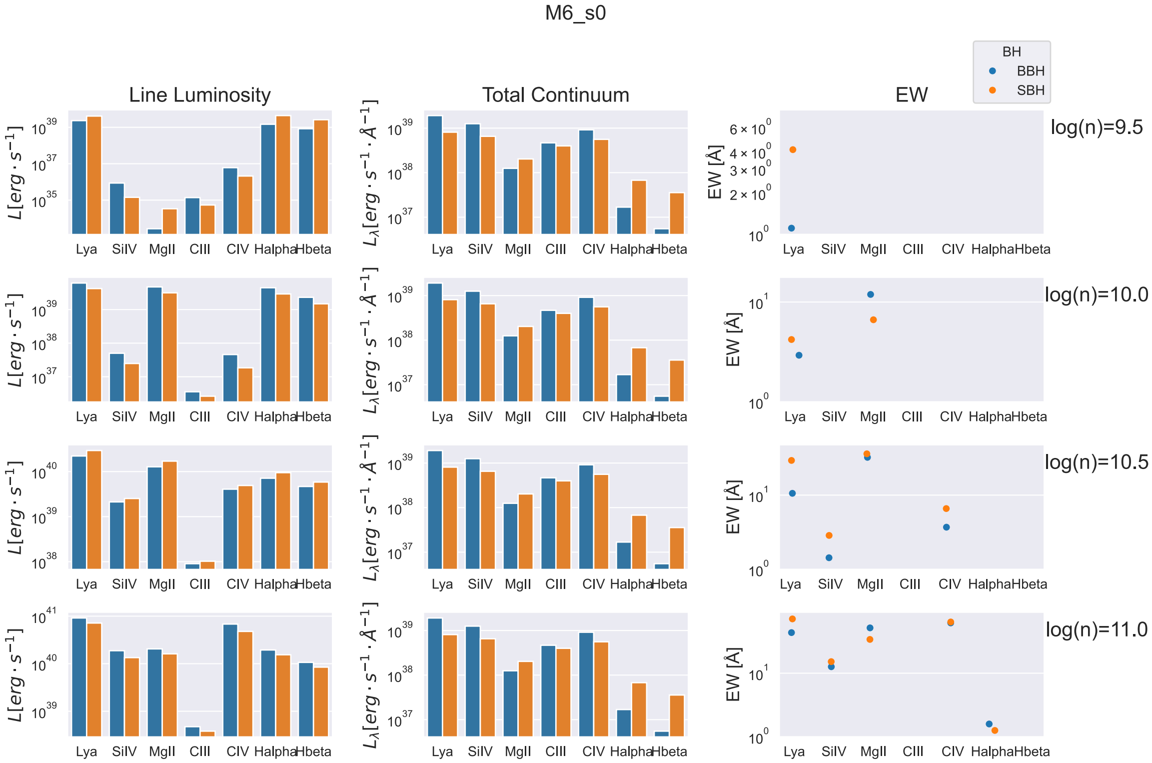

Figure B.8: Cloud ensemble models for the BLR computed with BELMAC. Line luminosity, total continuum including the galaxy continuum, and equivalent widths for a BH mass $10^6 M_\odot$ and $s = 0$. The color scheme here is: BBH denoted in blue and SBH denoted in orange. We have chosen seven emission lines, Si IV λ1400Å, C III] λ1909Å, C IV λ1549Å, Mg II λ2798Å, Lyα λ1216Å, Hα λ6562.80Å, and Hβ λ4861.32Å. There are three columns in the figure: from left to right, the first column shows the line luminosity, the second column shows the specific luminosity of the continuum of the accretion disk, and the third column shows the equivalent width, calculated by dividing the line luminosity by the continuum shown in the previous two columns. The black points with error bars show the mean and standard deviations of the observed EWs of MgII, CIV, Hβ, and Hα calculated using data from the SDSS DR7 Quasar catalog, for black hole masses in the range of $5.5 \leq \log_{10} M_{\rm BH} \leq 6.5$.

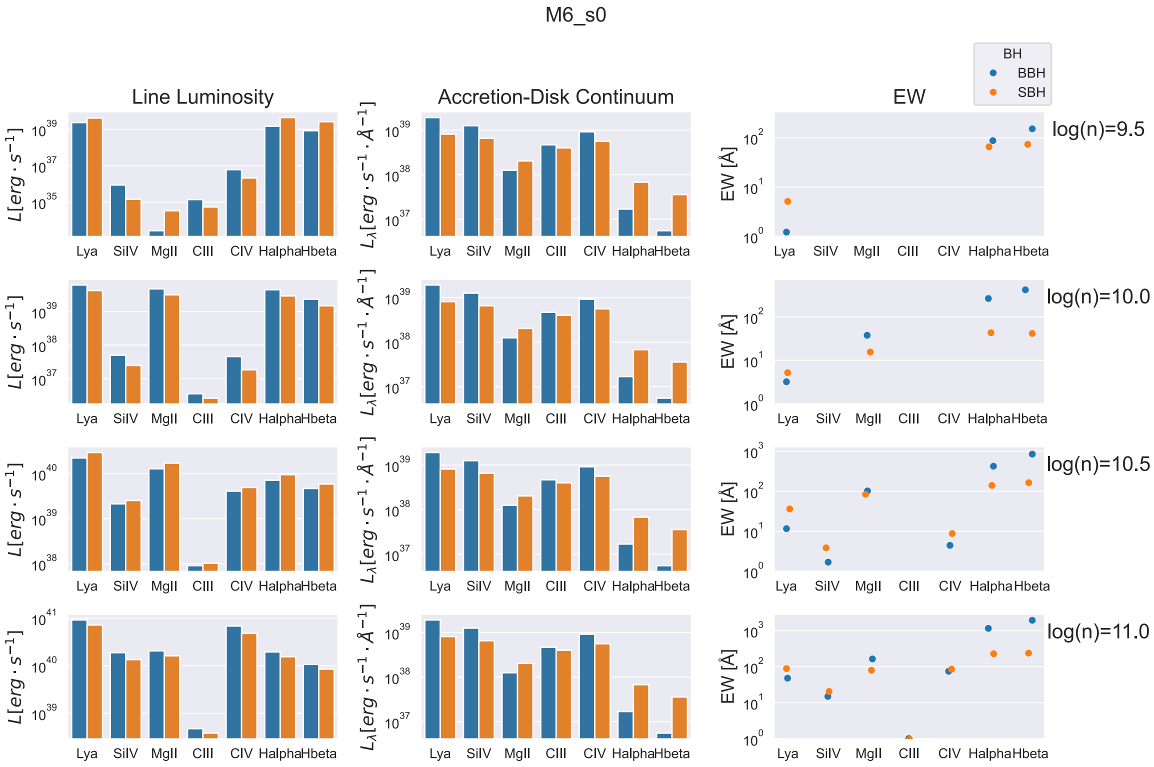

Figure B.9: Cloud ensemble models for the BLR computed with BELMAC. Line luminosity, accretion-disk luminosity, and equivalent widths for a BH mass $10^6 M_\odot$ and $s = 0$. The color scheme here is: BBH denoted in blue and SBH denoted in orange. We have chosen seven emission lines, Si IV λ1400Å, C III] λ1909Å, C IV λ1549Å, Mg II λ2798Å, Lyα λ1216Å, Hα λ6562.80Å, and Hβ λ4861.32Å. There are three columns in the figure: from left to right, the first column shows the line luminosity, the second column shows the specific luminosity of the continuum of the accretion disk, and the third column shows the equivalent width, calculated by dividing the line luminosity by the continuum shown in the previous two columns. The black points with error bars show the mean and standard deviations of the observed EWs of MgII, CIV, Hβ, and Hα calculated using data from the SDSS DR7 Quasar catalog, for black hole masses in the range of $5.5 \leq \log_{10} M_{\rm BH} \leq 6.5$.

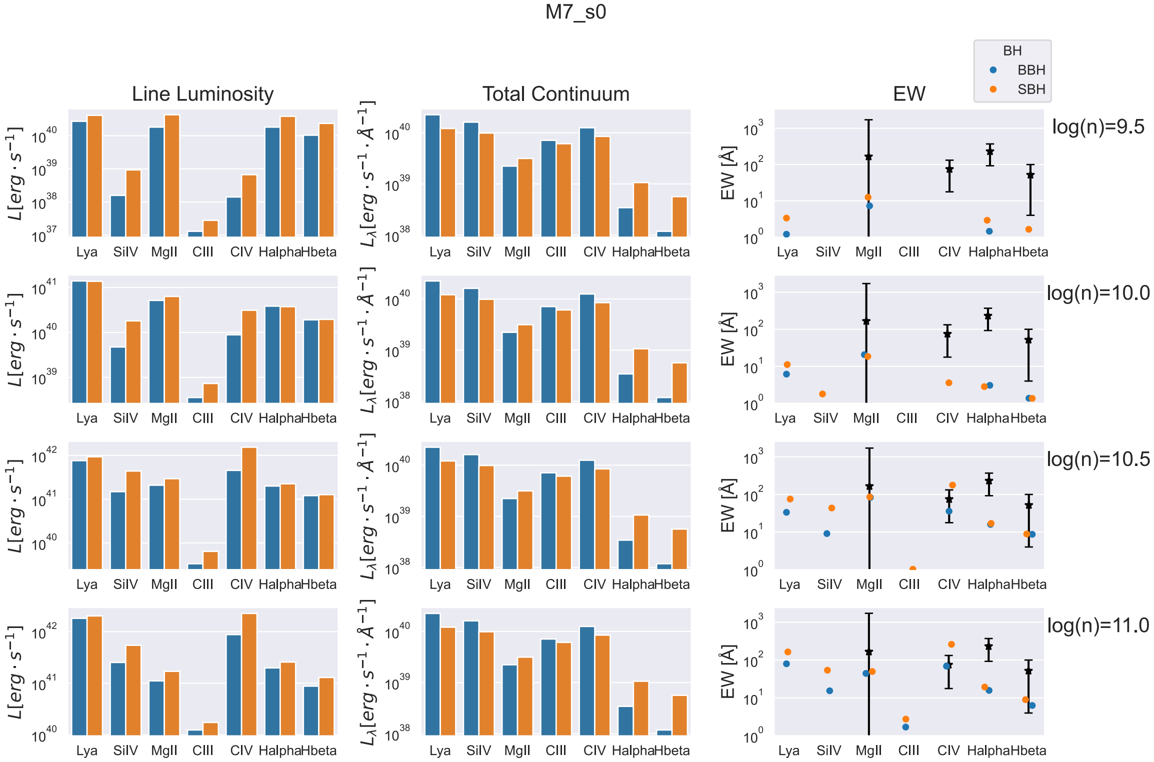

Figure B.10: Cloud ensemble models for the BLR computed with BELMAC. Line luminosity, accretion-disk luminosity, and equivalent widths for a BH mass $10^7 M_\odot$ and $s = 0$. The color scheme here is: BBH denoted in blue and SBH denoted in orange. We have chosen seven emission lines, Si IV λ1400Å, C III] λ1909Å, C IV λ1549Å, Mg II λ2798Å, Lyα λ1216Å, Hα λ6562.80Å, and Hβ λ4861.32Å. There are three columns in the figure: from left to right, the first column shows the line luminosity, the second column shows the specific luminosity of the continuum of the accretion disk, and the third column shows the equivalent width, calculated by dividing the line luminosity by the continuum shown in the previous two columns. The black points with error bars show the mean and standard deviations of the observed EWs of MgII, CIV, Hβ, and Hα calculated using data from the SDSS DR7 Quasar catalog, for black hole masses in the range of $6.5 \leq \log_{10} M_{\rm BH} \leq 7.5$.

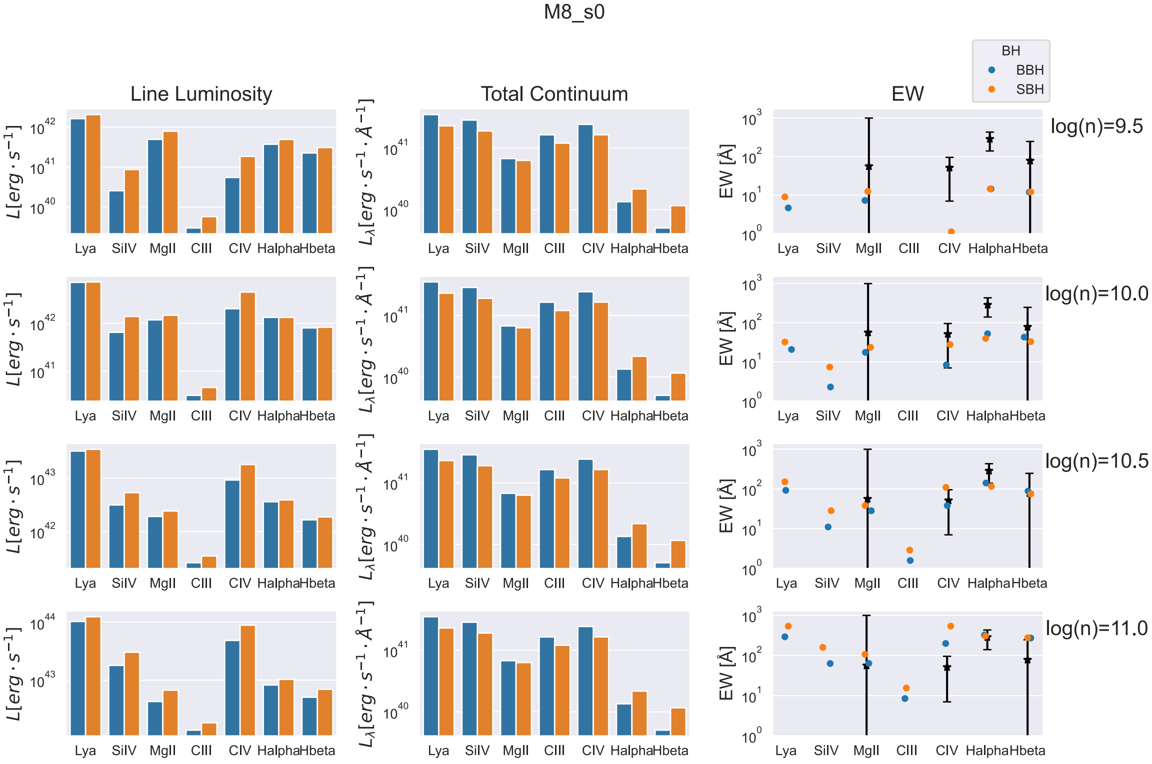

Figure B.11: Cloud ensemble models for the BLR computed with BELMAC. Line luminosity, total continuum including the galaxy continuum, and equivalent widths for a BH mass $10^8 M_\odot$ and $s = 0$. The color scheme here is: BBH denoted in blue and SBH denoted in orange. We have chosen seven emission lines, Si IV $\lambda1400$Å, C III] $\lambda1909$Å, C IV $\lambda1549$Å, Mg II $\lambda2798$Å, Lyα $\lambda1216$Å, Hα $\lambda6562.80$Å, and Hβ $\lambda4861.32$Å. There are three columns in the figure: from left to right, the first column shows the line luminosity, the second column shows the specific luminosity of the continuum of the accretion disk, and the third column shows the equivalent width, calculated by dividing the line luminosity by the continuum shown in the previous two columns. The black points with error bars show the mean and standard deviations of the observed EWs of MgII, CIV, Hβ, and Hα calculated using data from the SDSS DR7 Quasar catalog, for black hole masses in the range of $7.5 \leq \log_{10} M_{\rm BH} \leq 8.5$.

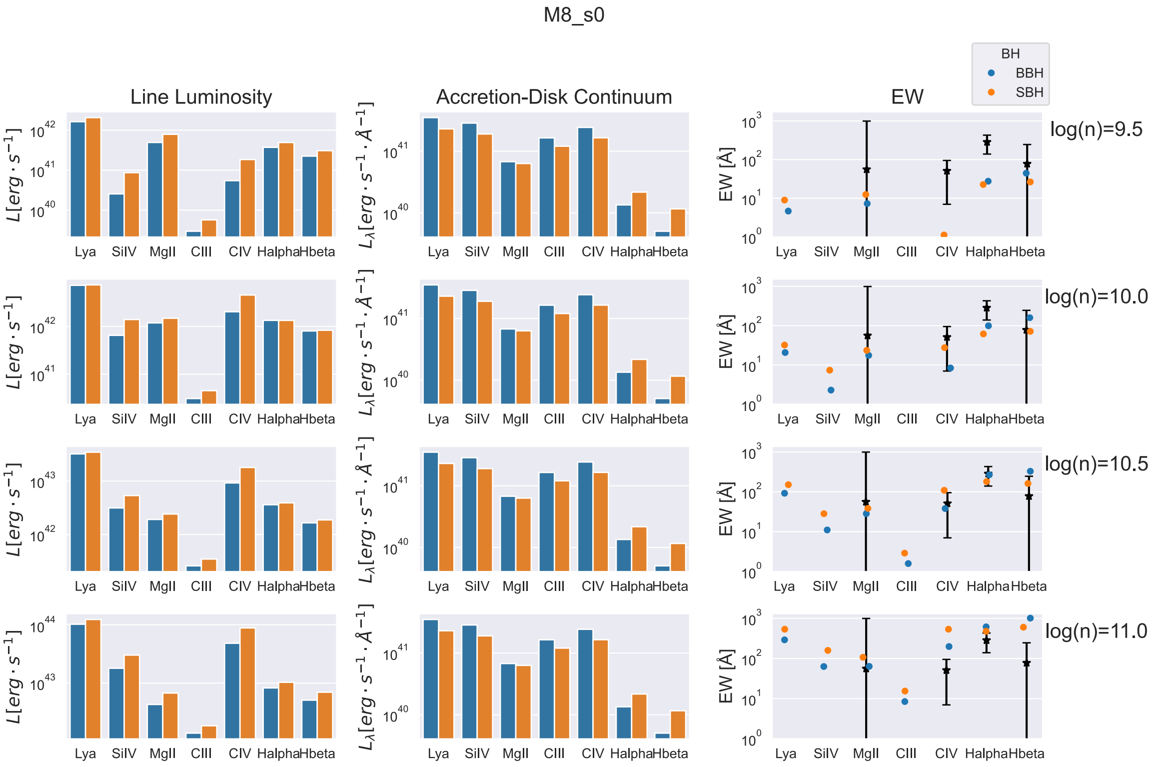

Figure B.12: Cloud ensemble models for the BLR computed with BELMAC. Line luminosity, accretion-disk luminosity, and equivalent widths for a BH mass $10^8 M_\odot$ and $s = 0$. The color scheme here is: BBH denoted in blue and SBH denoted in orange. We have chosen seven emission lines, Si IV λ1400Å, C III] λ1909Å, C IV λ1549Å, Mg II λ2798Å, Lyα λ1216Å, Hα λ6562.80Å, and Hβ λ4861.32Å. There are three columns in the figure: from left to right, the first column shows the line luminosity, the second column shows the specific luminosity of the continuum of the accretion disk, and the third column shows the equivalent width, calculated by dividing the line luminosity by the continuum shown in the previous two columns. The black points with error bars show the mean and standard deviations of the observed EWs of MgII, CIV, Hβ, and Hα calculated using data from the SDSS DR7 Quasar catalog, for black hole masses in the range of $7.5 \leq \log_{10} M_{\rm BH} \leq 8.5$.

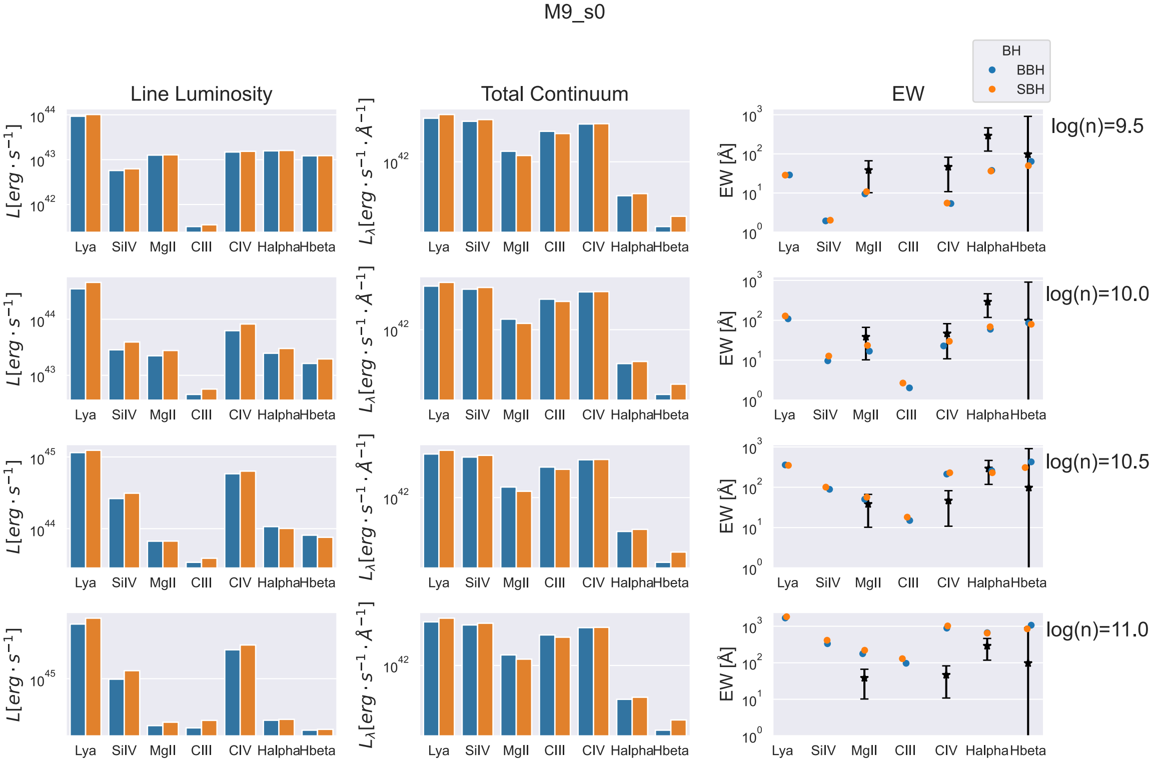

Figure B.13: Cloud ensemble models for the BLR computed with BELMAC. Line luminosity, total continuum including the galaxy continuum, and equivalent widths for a BH mass $10^9 M_\odot$ and $s = 0$. The color scheme here is: BBH denoted in blue and SBH denoted in orange. We have chosen seven emission lines, Si IV λ1400Å, C III] λ1909Å, C IV λ1549Å, Mg II λ2798Å, Lyα λ1216Å, Hα λ6562.80Å, and Hβ λ4861.32Å. There are three columns in the figure: from left to right, the first column shows the line luminosity, the second column shows the specific luminosity of the continuum of the accretion disk, and the third column shows the equivalent width, calculated by dividing the line luminosity by the continuum shown in the previous two columns. The black points with error bars show the mean and standard deviations of the observed EWs of MgII, CIV, Hβ, and Hα calculated using data from the SDSS DR7 Quasar catalog, for black hole masses in the range of $8.5 \leq \log_{10} M_{\rm BH} \leq 9.5$.

Bibliography

Amaro-Seoane, Pau et al. “Laser interferometer space antenna”. In: *arXiv preprint arXiv:1702.00786* (2017).

Amaro-Seoane, Pau et al. “Astrophysics with the laser interferometer space antenna”. In: *Living Reviews in Relativity* 26.1 (2023), p. 2.

Armengol, Federico G Lopez et al. “Circumbinary disk accretion into spinning black hole binaries”. In: *The Astrophysical Journal* 913.1 (2021), p. 16.

Artymowicz, Pawel et al. “Dynamics of binary-disk interaction. 1: Resonances and disk gap sizes”. In: *Astrophysical Journal, Part 1 (ISSN 0004-637X), vol. 421, no. 2, p. 651-667* 421 (1994), pp. 651–667.

— “Mass flow through gaps in circumbinary disks”. In: *The Astrophysical Journal* 467.2 (1996), p. L77.

Arzoumanian, Zaven et al. “Multimessenger gravitational-wave searches with pulsar timing arrays: application to 3C 66B using the NANOGrav 11-year data set”. In: *The Astrophysical Journal* 900.2 (2020), p. 102.

Baker, John et al. *Multimessenger science opportunities with mHz gravitational waves.* Tech. rep. 2019.

Baldwin, Jack A et al. “Classification parameters for the emission-line spectra of extragalactic objects.” In: *Publications of the Astronomical Society of the Pacific* 93.551 (1981), p. 5.

Begelman, Mitchell C et al. “Massive black hole binaries in active galactic nuclei”. In: *Nature* 287.5780 (1980), pp. 307–309.

Bentz, Misty C et al. “The low-luminosity end of the radius–luminosity relationship for active galactic nuclei”. In: *The Astrophysical Journal* 767.2 (2013), p. 149.

Bogdanovi, Tamara et al. “Electromagnetic counterparts to massive black-hole mergers”. In: *Living Reviews in Relativity* 25.1 (2022), p. 3.

Bonetti, Matteo et al. “Post-Newtonian evolution of massive black hole triplets in galactic nuclei–III. A robust lower limit to the nHz stochastic background of gravitational waves”. In: *Monthly Notices of the Royal Astronomical Society* 477.2 (2018), pp. 2599–2612.

Bowen, Dennis B et al. “Relativistic dynamics and mass exchange in binary black hole mini-disks”. In: *The Astrophysical Journal* 838.1 (2017), p. 42.

Bowen, Dennis B et al. “Quasi-periodic behavior of mini-disks in binary black holes approaching merger”. In: *The Astrophysical Journal Letters* 853.1 (2018), p. L17.

Bowen, Dennis B et al. “Quasi-periodicity of supermassive binary black hole accretion approaching merger”. In: *The Astrophysical Journal* 879.2 (2019), p. 76.

Brown, Michael JI et al. “An atlas of galaxy spectral energy distributions from the ultraviolet to the mid-infrared”. In: *The Astrophysical Journal Supplement Series* 212.2 (2014), p. 18.

Carroll, Bradley W. et al. *An Introduction to Modern Astrophysics*. 2nd ed. Cambridge University Press, 2017.

Chapon, Damien et al. “Hydrodynamics of galaxy mergers with supermassive black holes: is there a last parsec problem?” In: *Monthly Notices of the Royal Astronomical Society* 429.4 (2013), pp. 3114–3122.

Charisi, Maria et al. “Multimessenger time-domain signatures of supermassive black hole binaries”. In: *Monthly Notices of the Royal Astronomical Society* 510.4 (2022), pp. 5929–5944.

Chatzikos, Marios et al. “The 2023 release of Cloudy”. In: *arXiv preprint arXiv:2308.06396* (2023).

Colpi, Monica. “Massive binary black holes in galactic nuclei and their path to coalescence”. In: *Space Science Reviews* 183 (2014), pp. 189–221.

Combi, Luciano et al. “Minidisk Accretion onto Spinning Black Hole Binaries: Quasi-periodicities and Outflows”. In: *The Astrophysical Journal* 928.2 (2022), p. 187.

Cuadra, Jorge et al. “Massive black hole binary mergers within subparsec scale gas discs”. In: *Monthly Notices of the Royal Astronomical Society* 393.4 (2009), pp. 1423–1432.

D’Orazio, Daniel J et al. “Accretion into the central cavity of a circumbinary disc”. In: *Monthly Notices of the Royal Astronomical Society* 436.4 (2013), pp. 2997–3020.

D’Orazio, Daniel J et al. “Relativistic boost as the cause of periodicity in a massive black-hole binary candidate”. In: *Nature* 525.7569 (2015), pp. 351–353.

D’Orazio, Daniel J et al. “A transition in circumbinary accretion discs at a binary mass ratio of 1: 25”. In: *Monthly Notices of the Royal Astronomical Society* 459.3 (2016), pp. 2379–2393.

dAscoli, Stéphane et al. “Electromagnetic emission from supermassive binary black holes approaching merger”. In: *The Astrophysical Journal* 865.2 (2018), p. 140.

De Rosa, Alessandra et al. “The quest for dual and binary supermassive black holes: A multi-messenger view”. In: *New Astronomy Reviews* 86 (2019), p. 101525.

Done, Chris et al. “Intrinsic disc emission and the soft X-ray excess in active galactic nuclei”. In: *Monthly Notices of the Royal Astronomical Society* 420.3 (2012), pp. 1848–1860.

Dotti, Massimo et al. “Supermassive black hole binaries in gaseous and stellar circumnuclear discs: orbital dynamics and gas accretion”. In: *Monthly Notices of the Royal Astronomical Society* 379.3 (2007), pp. 956–962.

Farris, Brian D et al. “Binary black hole accretion from a circumbinary disk: gas dynamics inside the central cavity”. In: *The Astrophysical Journal* 783.2 (2014), p. 134.

Farris, Brian D et al. “Characteristic signatures in the thermal emission from accreting binary black holes”. In: *Monthly Notices of the Royal Astronomical Society: Letters* 446.1 (2015), pp. L36–L40.

Fath, Edward Arthur. “The spectra of some spiral nebulae and globular star clusters”. In: *Lick Observatory Bulletin* 149 (Jan. 1909), pp. 71–77. DOI: `10.5479/ADS/bib/1909LicOB.5.71F`.

Ferland, GJ et al. “CLOUDY 90: numerical simulation of plasmas and their spectra”. In: *Publications of the Astronomical Society of the Pacific* 110.749 (1998), p. 761.

Francis, Paul et al. “A high signal-to-noise ratio composite quasar spectrum”. In: (1991).

Frank, Juhan et al. *Accretion Power in Astrophysics: Third Edition.* 2002.

Gaskell, C Martin. “What broad emission lines tell us about how active galactic nuclei work”. In: *New Astronomy Reviews* 53.7-10 (2009), pp. 140–148.

Gutiérrez, Eduardo M et al. “Electromagnetic signatures from supermassive binary black holes approaching merger”. In: *The Astrophysical Journal* 928.2 (2022), p. 137.

Haehnelt, Martin G et al. “Multiple supermassive black holes in galactic bulges”. In: *Monthly Notices of the Royal Astronomical Society* 336.3 (2002), pp. L61–L64.

Hoffman, Loren et al. “Dynamics of triple black hole systems in hierarchically merging massive galaxies”. In: *Monthly Notices of the Royal Astronomical Society* 377.3 (2007), pp. 957–976.

Hopkins, Philip F et al. “A cosmological framework for the co-evolution of quasars, supermassive black holes, and elliptical galaxies. I. Galaxy mergers and quasar activity”. In: *The Astrophysical Journal Supplement Series* 175.2 (2008), p. 356.

Jin, Chichuan et al. “A combined optical and X-ray study of unobscured type 1 active galactic nuclei–I. Optical spectra and spectral energy distribution modelling”. In: *Monthly Notices of the Royal Astronomical Society* 420.3 (2012), pp. 1825–1847.

Ju, Wenhua et al. “Global MHD simulations of accretion disks in cataclysmic variables. I. The importance of spiral shocks”. In: *The Astrophysical Journal* 823.2 (2016), p. 81.

Kara, Erin et al. “X-ray follow-up of extragalactic transients”. In: *arXiv preprint arXiv:1903.05287* (2019).

Kelley, Luke Zoltan et al. “Multi-messenger astrophysics with pulsar timing arrays”. In: *arXiv preprint arXiv:1903.07644* (2019).

Kewley, Lisa J et al. “The host galaxies and classification of active galactic nuclei”. In: *Monthly Notices of the Royal Astronomical Society* 372.3 (2006), pp. 961–976.

Khan, Fazeel Mahmood et al. “Formation and hardening of supermassive black hole binaries in minor mergers of disk galaxies”. In: *The Astrophysical Journal* 756.1 (2012), p. 30.

Kormendy, John et al. “Inward boundthe search for supermassive black holes in galactic nuclei”. In: *Annual review of astronomy and Astrophysics* 33.1 (1995), pp. 581–624.

Kormendy, John et al. “Coevolution (or not) of supermassive black holes and host galaxies”. In: *Annual Review of Astronomy and Astrophysics* 51 (2013), pp. 511–653.

Liu, Tingting et al. “Multi-messenger approaches to supermassive black hole binary detection and parameter estimation: implications for nanohertz gravitational wave searches with pulsar timing arrays”. In: *The Astrophysical Journal* 921.2 (2021), p. 178.

Loeb, Abraham. “Observable signatures of a black hole ejected by gravitational-radiation recoil in a galaxy merger”. In: *Physical Review Letters* 99.4 (2007), p. 041103.

MacFadyen, Andrew I et al. “An eccentric circumbinary accretion disk and the detection of binary massive black holes”. In: *The Astrophysical Journal* 672.1 (2008), p. 83.

Magorrian, John et al. “The demography of massive dark objects in galaxy centers”. In: *The Astronomical Journal* 115.6 (1998), p. 2285.

Mayer, Lucio et al. “Rapid formation of supermassive black hole binaries in galaxy mergers with gas”. In: *Science* 316.5833 (2007), pp. 1874–1877.

McConnell, Nicholas J et al. “Revisiting the scaling relations of black hole masses and host galaxy properties”. In: *The Astrophysical Journal* 764.2 (2013), p. 184.

Merritt, David et al. “Chaotic loss cones and black hole fueling”. In: *The Astrophysical Journal* 606.2 (2004), p. 788.

Merritt, David et al. “Massive black hole binary evolution”. In: *arXiv preprint astro-ph/0410364* (2004).

Merritt, David et al. “Orbits around black holes in triaxial nuclei”. In: *The Astrophysical Journal* 726.2 (2010), p. 61.

Nenkova, Maia et al. “AGN dusty tori. II. Observational implications of clumpiness”. In: *The Astrophysical Journal* 685.1 (2008), p. 160.

Netzer, Hagai. “Ionized gas in active galactic nuclei”. In: *New Astronomy Reviews* 52.6 (2008), pp. 257–273.

Noble, Scott C et al. “Simulating the emission and outflows from accretion discs”. In: *Classical and Quantum Gravity* 24.12 (2007), S259.

Noble, Scott C et al. “Direct calculation of the radiative efficiency of an accretion disk around a black hole”. In: *The Astrophysical Journal* 692.1 (2009), p. 411.

Noble, Scott C et al. “Mass-ratio and magnetic flux dependence of modulated accretion from circumbinary disks”. In: *The Astrophysical Journal* 922.2 (2021), p. 175.

Noble et al. “Circumbinary magnetohydrodynamic accretion into inspiraling binary black holes”. In: *The Astrophysical Journal* 755.1 (2012), p. 51.

Pringle, JE. “The properties of external accretion discs”. In: *Monthly Notices of the Royal Astronomical Society* 248.4 (1991), pp. 754–759.

Quinlan, Gerald D. “The time-scale for core collapse in spherical star clusters”. In: *arXiv preprint astro-ph/9606182* (1996).

Reynolds, Christopher S. “Observational constraints on black hole spin”. In: *Annual Review of Astronomy and Astrophysics* 59 (2021), pp. 117–154.

Richstone, Denuk et al. “Supermassive black holes and the evolution of galaxies”. In: *arXiv preprint astro-ph/9810378* (1998).

Rosborough, Sara A et al. “Modeling the Reverberation Response of the Broad-line Region in Active Galactic Nuclei”. In: *The Astrophysical Journal* 965.1 (2024), p. 35.

Ryan, Geoffrey et al. “Minidisks in binary black hole accretion”. In: *The Astrophysical Journal* 835.2 (2017), p. 199.

Ryu, Taeho et al. “Interactions between multiple supermassive black holes in galactic nuclei: a solution to the final parsec problem”. In: *Monthly Notices of the Royal Astronomical Society* 473.3 (2018), pp. 3410–3433.

Shen, Yue et al. “A Catalog of Quasar Properties from SDSS DR7”. In: *arXiv preprint arXiv:1006.5178* (2010).

Shi, Ji-Ming et al. “Three-dimensional magnetohydrodynamic simulations of circumbinary accretion disks: disk structures and angular momentum transport”. In: *The Astrophysical Journal* 749.2 (2012), p. 118.

Shi, Ji-Ming et al. “Three-dimensional MHD simulation of circumbinary accretion disks. II. Net accretion rate”. In: *The Astrophysical Journal* 807.2 (2015), p. 131.

Tang, Yike et al. “The late inspiral of supermassive black hole binaries with circumbinary gas discs in the LISA band”. In: *Monthly Notices of the Royal Astronomical Society* 476.2 (2018), pp. 2249–2257.

Tremaine, Scott et al. “The slope of the black hole mass versus velocity dispersion correlation”. In: *The Astrophysical Journal* 574.2 (2002), p. 740.

Urry, C Megan et al. “Unified schemes for radio-loud active galactic nuclei”. In: *Publications of the Astronomical Society of the Pacific* 107.715 (1995), p. 803.

White, Simon DM et al. “Core condensation in heavy halos: a two-stage theory for galaxy formation and clustering”. In: *Monthly Notices of the Royal Astronomical Society* 183.3 (1978), pp. 341–358.

White, Simon DM et al. “Galaxy formation through hierarchical clustering”. In: *Astrophysical Journal, Part 1 (ISSN 0004-637X), vol. 379, Sept. 20, 1991, p. 52-79. Research supported by NASA, NSF, and SERC.* 379 (1991), pp. 52–79.

Yu, Qingjuan. “Evolution of massive binary black holes”. In: *Monthly Notices of the Royal Astronomical Society* 331.4 (2002), pp. 935–958.

— “Evolution of massive binary black holes”. In: *Classical and Quantum Gravity* 20.10 (2003), S55.

Yu, Qingjuan et al. “Evolution of accretion disks around massive black holes: constraints from the demography of active galactic nuclei”. In: *The Astrophysical Journal* 634.2 (2005), p. 901.

Zilhão, Miguel et al. “Resolving the relative influence of strong field spacetime dynamics and MHD on circumbinary disk physics”. In: *Physical Review D* 91.2 (2015), p. 024034.